Theses and Dissertations

Summer 2015

Compressed sensing applied to weather radar

Kumar Vijay Mishra
University of Iowa

Recommended Citation

Mishra, Kumar Vijay. "Compressed sensing applied to weather radar." PhD (Doctor of Philosophy) thesis, University of Iowa, 2015.
http://ir.uiowa.edu/etd/1885.

COMPRESSED SENSING APPLIED TO WEATHER RADAR

by

Kumar Vijay Mishra

A thesis submitted in partial fulfillment
of the requirements for the Doctor of
Philosophy degree in Electrical and Computer Engineering
in the Graduate College of
The University of Iowa

August 2015

Thesis Supervisors: Professor Anton Kruger
Professor Witold F. Krajewski

Graduate College
The University of Iowa
Iowa City, Iowa

CERTIFICATE OF APPROVAL

_____

PH.D. THESIS

_____

This is to certify that the Ph.D. thesis of

Kumar Vijay Mishra

has been approved by the Examining Committee
for the thesis requirement for the Doctor of Philosophy
degree in Electrical and Computer Engineering at the August 2015 graduation.

Thesis Committee: _____
                          Anton Kruger, Thesis Supervisor

                   _____
                          Witold F. Krajewski, Thesis Supervisor

                   _____
                          Er-Wei Bai

                   _____
                          Palle E. T. Jorgensen

                   _____
                          Weiyu Xu

                   _____
                          Ananya Sen Gupta

To my Mom Shraddha Mishra who has always been a source of great inspiration

To my brothers Kumar Digvijay Mishra, Kumar Jay Mishra,
sister-in-law Chitra Jaya Mishra, and great aunt Shyama Dubey

To the youngest member of Mishra family, my nephew Kumar Shatrunjay Mishra

To the memories of my Grandma Rajrani Dubey and Dad Shyam Bihari Mishra

जो इच्छा करिहहु मन माहीं। हरि प्रसाद कछु दुर्लभ नाहीं॥
Jo icchā karihahu mana māhīṃ. Hari prasāda kachu durlabha nāhīṃ.
By the grace of Sri Hari, you shall have no difficulty in attaining any of your goals.
Tulasīdāsa, Śrīrāmacaritamānasa (Uttara Kāṇḍa, 114:4)

ACKNOWLEDGMENTS

ABSTRACT

Over the last two decades, dual-polarimetric weather radar has proven to be a valuable instrument providing critical precipitation information through remote sensing of the atmosphere. Modern weather radar systems operate with high sampling rates and long dwell times on targets. Often only limited target information is desired, leading to a pertinent question: could lesser samples have been acquired in the first place? Recently, a revolutionary sampling paradigm – compressed sensing (CS) – has emerged, which asserts that it is possible to recover signals from fewer samples or measurements than traditional methods require without degrading the accuracy of target information. CS methods have recently been applied to point target radars and imaging radars, resulting in hardware simplification advantages, enhanced resolution, and reduction in data processing overheads. But CS applications for volumetric radar targets such as precipitation remain relatively unexamined. This research investigates the potential applications of CS to radar remote sensing of precipitation. In general, weather echoes may not be sparse in space-time or frequency domain. Therefore, CS techniques developed for point targets, such as in aircraft surveillance radar, are not directly applicable to weather radars. However, precipitation samples are highly correlated both spatially and temporally. We, therefore, adopt latest advances in matrix completion algorithms to demonstrate the sparse sensing of weather echoes. Several extensions of this approach are then considered to develop a more general CS-based weather radar processing algorithms in presence of noise, ground clutter and dual-polarimetric data. Finally, a super-resolution approach is presented for the spectral recovery of an undersampled signal when certain frequency information is known.

PUBLIC ABSTRACT

A scanning radar beams a signal in multiple directions, and extracts the information about the targets from the signal that comes back after interaction with a target. A fast scanning radar would be able to update the changing target scenario quickly but, at the same time, it would also hit a target less frequently leading to inaccurate interpretation of target information. Recent research on the application of a novel technique called compressed sensing (CS) to synthetic aperture radars and point target radars suggests that the radar scan rate can be increased without compromising the information accuracy. However, these research efforts have not investigated application of CS to weather radars. In this research, we propose a CS framework for weather radars where the target-of-interest is volumetric. Our approach is based on the recent advances in low-rank matrix completion. We use Iowa X-band Polarimetric (XPOL) radar data to test our algorithms.

TABLE OF CONTENTS

LIST OF TABLES

LIST OF FIGURES

CHAPTER 1

INTRODUCTION

The electromagnetic wave is characterized by its amplitude, frequency and polarization state. The interaction of the radiated wave from the radar with the moving particles in the atmosphere brings a change in all three characteristics of the scattered wave. By analyzing this change it is possible to infer the particles' size, radial velocity, shape and orientation. The earliest weather radars in the era of the 1950s were mainly used to measure the back scatter power at a single polarization state. During the 1960-70s, the Doppler shift principle was used to measure the radial velocity of hydrometeors in addition to the back scattered power although still using a single polarization state. By the mid-1970s, the Doppler radar's importance for operational applications was widely recognized. In the late 1980s, the deployment of Doppler radars for operational weather forecasting by National Weather Service (NWS) accelerated, and has continued to the present time (Bringi et al. 2007).

Before early 1970s there was limited research in dual-polarized radars for weather applications. The measurements were limited by the poor cross polar performance of the radar hardware, particularly the antenna and its feed. The modern era of polarimetric radar using precision microwave hardware began with the Canadian radars (McCormick and Hendry 1979) starting in the late 60s-early 70s using dual-circular polarization techniques for propagation research (Ka and X-bands) and hail detection (at S-band). This research clearly showed that oblate rain drops formed a highly oriented medium and that the differential propagation phase and differential attenuation between the horizontal and vertical polarizations through such a highly-oriented medium could be measured at Ka and S-bands using circular polarization techniques without requiring any Doppler processing (Hendry et al. 1976). The use of widely used dual-linear polarizations (horizontal and vertical) was proposed in the late 70s primarily because at low elevation

angles these states are aligned along the principal axes of the highly oriented oblate rain medium (Seliga and Bringi 1976; Seliga and Bringi 1978).

Motivations

With the advances in hardware for the dual-polarized transmission, the signal processing of weather radar signals has also improved (Keeler and Passarelli 1990). The primary function of radar signal processing is the accurate, efficient extraction of information from radar echoes. A typical pulsed Doppler radar system samples data at 1000 range bins at 1 kilohertz pulse repetition frequency (PRF), generating approximately 3 million samples per second (typically in-phase (I) and quadrature phase (Q) components from a linear channel receiver). These "time series", in their raw form, convey little information that is of direct use in determining the state of the atmosphere. The volume of time series data is sufficiently large that storage for later analysis is impractical except for limited regions of time and space. The data must be processed in real time to reduce its volume and to convert it to more useful form.
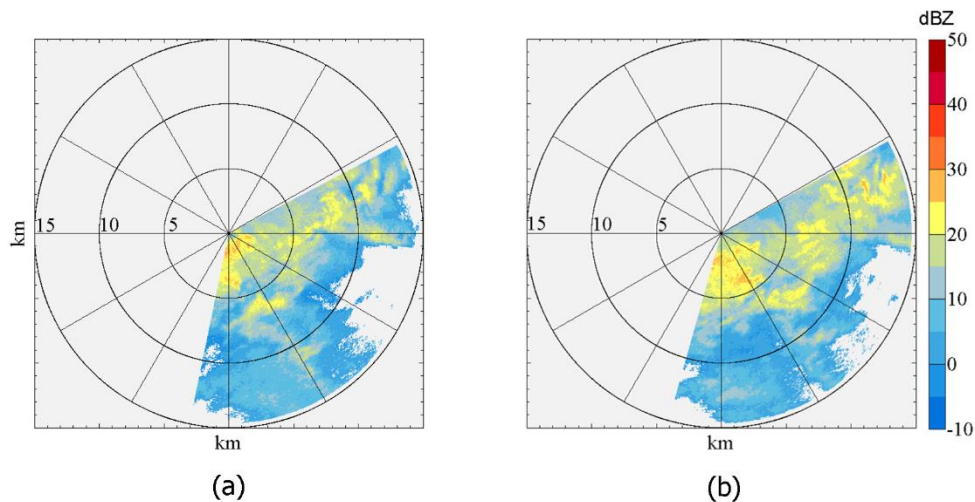
Figure 1. Observed reflectivity for a rain event by XPOL-2 radar on 12 June 2013 at the scan rate of (a) 8 $^\circ$s^{-1} and (b) 5 $^\circ$s^{-1}.

The radar signal acquisition is greatly affected by the dwell time, i.e., the time duration a radar beam spends hitting a particular target (Skolnik 2008b). Surveillance radars constantly scan the target *scene* in order to provide quick updates on the movement of targets-of-interest. The scan rate of the radar is often limited by the dwell time, which, in turn, is determined by the precision necessary to ascertain information about the target. A longer dwell time would lead to more accurate target information, but, simultaneously, it would decrease the update rate of the target *scene* (Figure 1). Using conventional radar hardware and signal processing techniques, it is difficult to maintain the data quality with faster scan rates.

Further, the massive data acquisition of weather radar is accentuated if the radar is deployed onboard satellites such as the Primary Radar (PR) on Tropical Rainfall Measuring Mission (TRMM) (Kummerow et al. 2000) and Dual Precipitation Radar (DPR) onboard recently launched Global Precipitation Measurement (GPM) satellites (Iguchi et al. 2003). In general, remote sensing by satellites is characterized by massive data acquisitions of global-scale information (Ma and Le Dimet 2009). In the case of higher-resolution satellite-based imaging, the data acquisition is often followed by data compression to store and transmit data in order to make economical use of satellite hardware and power. The transmission of compressed data back to Earth introduces distortions and mosaic artifacts (Ma 2009). As the use of spaceborne weather radars that sample data more frequently becomes commonplace, these satellites will soon be confronted with the problems of storage, transmission, and power, while also trying to preserve spatial resolutions and quality. It might be more efficient to eliminate the data compression step in satellite-based remote sensing and, instead, make limited measurements.

Compressed Sensing

Formally proposed in 2006 in two seminal research papers (Donoho 2006a; Candès et al. 2006), CS is a novel signal processing technique that unites digital sampling and digital data compression in a single step. While conventional signal processing methods sample at Nyquist-Shannon rate and then compress the data for minimal storage, CS allows sampling of only useful information at lower sampling rates. This feature is particularly attractive for many radar and remote sensing applications which require efficient and rapid data acquisition.

At the heart of CS lies the following problem (Figure 1): a discrete signal x of length N, is K-sparse if at most $K \ll N$ of its coefficients are nonzero (perhaps under some appropriate dictionary, such as Fourier, wavelet, etc.). Then the *true* information content of x lives in at most K dimensions rather than N. Therefore, for signal acquisition, one has only to measure a signal $M \sim K$ times instead of N. This is done by making M non-adaptive, random, linear observations in the form of $y = Ax$ where A is an $M \times N$ *measurement matrix*. If A is sufficiently "incoherent," then the information of x will be embedded in y such that it can be perfectly recovered with a very high probability. For practical applications, the condition of sparsity is relaxed to *compressibility* or *approximate sparsity*. Here, most of the coefficients are assumed to
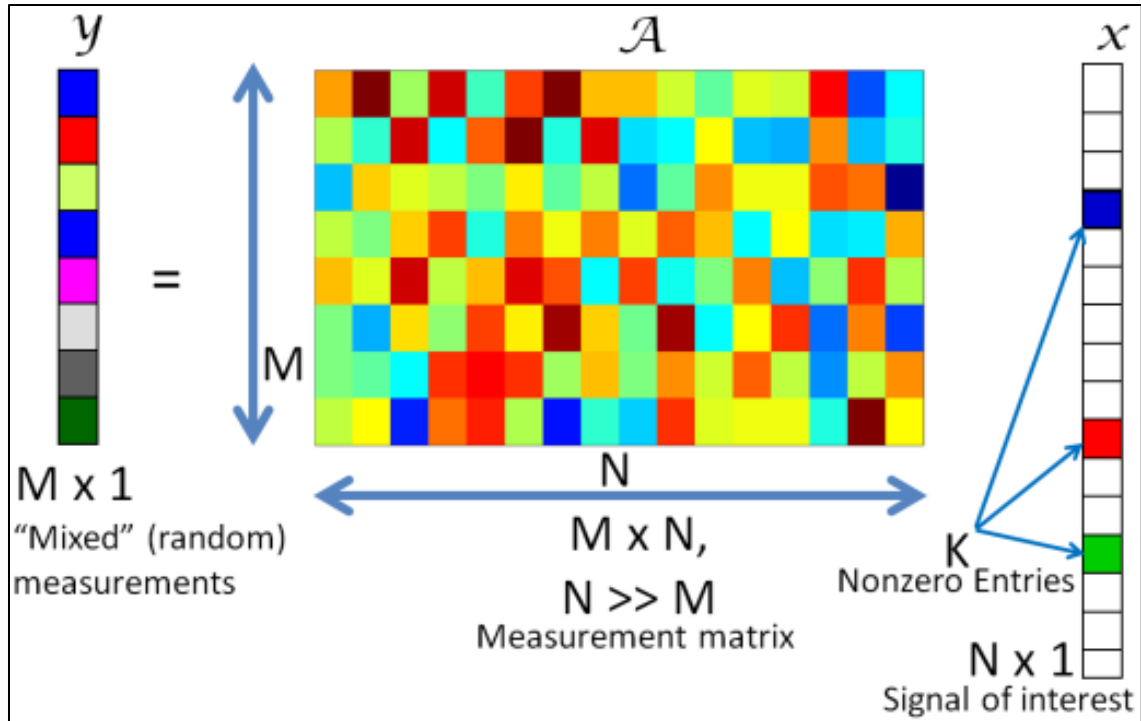
Figure 2. Illustration of compressed sensing problem. The measurement matrix is a randomly generated Gaussian matrix (Baraniuk 2007).

be very small or insignificant but not exactly zero, thereby making it possible to apply CS on sparse signals in noise.

The compressed sensing approach recovers the sparse signal x from the knowledge of y by finding the solution to the following problem (Baraniuk 2007):

$$(P_0) \qquad \begin{aligned} &\text{minimize } \|x\|_0 \\ &\text{subject to } y = Ax \end{aligned} \qquad (1)$$

where $\|\cdot\|_0$ denotes the ℓ_0 norm, i.e., the number of non-zero elements in a vector. It is obvious that minimizing the ℓ_0 norm would yield the sparsest solution to problem (P_0). However, solving (P_0) would require a combinatorial search and computational resources beyond the current technological reach. The key result from the theory of compressed sensing states that, under certain "incoherency" conditions on matrix A, (P_0) can be solved by replacing ℓ_0 by its closest convex approximation – the ℓ_1 norm – as follows:

$$\text{minimize } \|x\|_1$$

(P_1) $\qquad\qquad\qquad\qquad\qquad\qquad\qquad\qquad\qquad\qquad\qquad\qquad\qquad$ (2)

$$\text{subject to } y = Ax$$

In summary, for CS techniques to succeed, (a) x must be sparse and (b) A must be incoherent, i.e., the measurements should be randomly mixed. Stating these requirements for a radar problem, the radar echoes must be sparse and the antenna must sample the radar coverage domain randomly.

Prior Art And Inspirations

Because radar signals are quite recognizably sparse in range and frequency, with typically few targets of interest within range, radar is a natural fit for compressed sensing. There are two different tasks of radar: the first is to detect and localized distinct targets. Here, the resolution cells in range, Doppler, and angle are designed coarse enough to assume that the target is contained in a single cell. The second radar operation is imaging; here the aim is to have many fine resolution cells covering the target (inverse synthetic aperture radar (ISAR), range-profiling) or the scene (synthetic aperture radar (SAR)) to get image-like information. In both situations, CS can be applied in principle. For imaging, the sparsity property can be justified if there are only a few dominant point-like scattering centers in the scene, which is often true especially for targets like vehicles, airplanes and soon. A spiky reconstruction of the reflectivity - as CS offers—has the potential to be of high value for automatic target recognition.

The role of sparsity in radar signal processing and how compressed sensing techniques relate to established processing methods is discussed by (Potter et al. 2010) with compressed sensing to reduce radar hardware complexity and cost is noted by (Baraniuk and Steeghs 2007), and (Ender 2010), while (Herman and Strohmer 2009) explores the use of compressed sensing for increased target detection resolution.

There are many papers about application of CS to various radar tasks. The most elementary task is pulse compression, treated in a large number of papers, where sparse

sampling can be applied in the fast time domain as well as in the frequency domain. An efficient method is to transmit a set of frequencies instantaneously (Ender 2010; Yanan et al. 2011). The optimization of the waveforms for CS is regarded e.g. in (He et al. 2011), orthogonal frequency division multiplexing (OFDM) waveforms in (Lellouch et al. 2009). Aerospace multi-channel MTI is an interesting situation where the space of scene points is extended by the dimension 'radial velocity'. The clutter returns gather at the subspace in which Doppler is zero while moving targets are represented by sparse points in the volume (Pruente 2010).

A great attention has been directed to multiple-input/multiple-output (MIMO) radar systems [11, 12] (Kalogerias et al. 2013; Yu et al. 2012b). This situation well fitted to CS reconstruction, since the signals are related to all Tx/Rx pairs which in general lead to a non-uniform thinned sampling in range and angles. Passive coherent location (PCL) is a special case of a MIMO radar where the waveforms and the positions of the transmitters cannot be influenced by the user.

The application of CS to Synthetic Aperture Radar (SAR) may be problematic, first because of the possibly not given sparsity of the reflectivity, and secondly because of the tremendous numerical effort needed if larger images shall be processed. On the other hand, CS applied to SAR tomography is really a great example for a reasonable CS use (Zhu and Bamler 2012). While the SAR images for different paths of an earth observation satellite are conventionally generated in range and azimuth, the reflectivity in the third dimension - here: the elevation angle – is reconstructed via CS. Since normally in one range-azimuth pixel only one elevation angle is occupied by scatterers, in the case of layover also reflections from two or more elevation angles can be present. The scene is naturally sparse in the third dimension. The application of CS to ISAR imaging (Li et al. 2012) is promising, especially since the number of pixels can be limited and the objects often show sparse reflections.

Many attempts have also been undertaken to process ultra-wide-band (UWB) radar data by CS algorithms, often in the application to through-the-wall radar and ground penetrating radar (Ender 2010). The latter is particularly interesting because of the unknown permittivity of the ground.

As outlined above, most of the research efforts on application of CS to radar remote sensing are confined to point target radars or imaging radars such as SAR. The potential of CS to weather radars which sense volumetric targets is relatively unexamined so far.

<u>Structure Of The Thesis</u>

This research has observational, numerical and theoretical components. In this chapter, we introduced the research problem and motivations of using CS to address the faster scans of weather radars. We discussed existing application of compressed sensing for radar and remote sensing problems, in particular, for point-target radars.

Chapter 2 provides a brief overview of the signal theory of weather radars and the Polarimetric observables. For past few years, there has been enormous interest in short-wavelength weather radars. We explain this thrust in the context of Iowa X-band POLarimetric (XPOL) radars that we use for data collection for this research.

In Chapter 3, we discuss the existing formulations of compressed sensing to point-target radars, and their inapplicability to weather which is a volumetric target. The weather echo is nor parsimonious in conventional dictionaries of range-time and Doppler. We explain these aspects in detail in this chapter.

Chapter 4 presents our approach where we formulate the CS-based weather radar as a matrix completion problem. We also discuss the differences our problem has with other related research areas. Chapter 4 includes some preliminary results that we extend to more practical scenarios in Chapter 5. Such as noise, clutter and dual-polarimetric variables

Chapter 6 presents our work on spectral super-resolution that initially began as a CS application to the weather echo spectrum but later yielded several interesting results for other signal processing applications. We consider probabilistic priors, block priors and known poles, and present interesting theoretical results for spectral estimation using undersampled signals. Chapter 7 concludes the thesis by summarizing the results obtained and outlining future directions of this research.

CHAPTER 2

SIGNAL THEORY OF WEATHER RADAR

Although weather radar signals cannot be modeled as sparse in conventional dictionaries such as time and frequency, the backscattered signal in a weather radar is coherent (Keeler and Passarelli 1990). In other words, the motion among the precipitation scatterers is small compared to the radar wavelength, so their relative positions produce highly correlated echoes from sample to sample and scan to scan. This inherent redundancy in weather radar signals implies that the range-azimuth scan of precipitation echoes can be modeled as a low-rank matrix.

The principle of a ground-based scanning weather radar is to transmit the electromagnetic waves at a wavelength λ of near-constant power P_t in very short pulses of width T_0, concentrated into a narrow beam defined by its radiating antenna, at predetermined azimuthal and elevation angles at periodic intervals of pulse repetition time (PRT) T_s. As each transmit pulse travels away from the radar, the returned voltage $V_r(t)$ at time t of the electromagnetic waves backscattered from the targets within the sampling volume is measured by the radar. The difference between the times of transmitted and received pulses can be translated into distance or range to map the returned echo within the three-dimensional space comprising all sampling volumes (Doviak and Zrnić 1993, p. 64).

Received Signal And Its Statistics

In radar meteorology, the weather signals are defined as the composite of echoes from individual scatterers. These individual echoes constructively or destructively add to produce a complex composite phasor sample. The received voltage can, therefore, be expressed as (Bringi and Chandrasekar 2001, p. 221),

$$V_r(t) = \sum_k A_k(\tau; t) e^{-j2\pi f_0 \tau_k} U_{tr}(t - \tau_k) \tag{3}$$

where A_k is the scattering amplitude of the kth particle at range $r_k = c\tau_k/2$, $f_0 = c/\lambda$ is the frequency of the radar, c is the speed of light and U_{tr} is the transmitted waveform. Further, the complex voltage sample can be expressed in terms of two real information-bearing signals as $V_r(t) = I(t) + jQ(t)$, where $I(t)$ and $Q(t)$ are the in-phase and quadrature(-phase) components. The term "quadrature component" refers to the fact that it is in phase quadrature $(+\pi/2)$ with respect to the in-phase component (Scherier and Scharf 2010, p. 9).

The range r_k of the independent scatterer being random, $V_r(t)$ is a complex sum of independent random variables. The central limit theorem (Papoulis and Pillai 2002) applies since, for the hydrometeor echoes, the number of scatterers is large and none of the variables is dominant. Therefore, the samples of V_r form a Gaussian distribution with zero mean. If V_1, V_2, $\cdots$, V_N form a set of N complex received voltage samples corresponding to N consecutive transmitted pulses, then the probability density function of the signal vector $V = [V_1 \, V_2 \, \cdots \, V_N]$ is a circular (Fjørtoft and Lopès 2001) or proper (Scherier and Scharf 2010, p. 53) complex Gaussian distribution with zero mean:

$$p(\boldsymbol{V}) = \frac{1}{\pi^N |\boldsymbol{R}_{vv}|} \exp(-\boldsymbol{V}^H \boldsymbol{R}_{vv}^{-1} \boldsymbol{V}) \tag{4}$$

where $\boldsymbol{R}_{vv}$ is the $N \times N$ complex covariance matrix corresponding to the signal vector $\boldsymbol{V}$.

Since the I and Q components are independent Gaussian random variables, it follows that the amplitude $|V| = (I^2 + Q^2)^{1/2}$ is Rayleigh distributed while the phase $\theta = \tan^{-1}(Q/I)$ has a uniform distribution:

$$p(|V|) = \frac{|V|}{\sigma^2} \exp\left(-\frac{|V|^2}{2\sigma^2}\right) \tag{5}$$

$$p(\theta) = \frac{1}{2\pi} \tag{6}$$

where σ^2 is the mean square value of I (as well as Q).

Since the power P is proportional to $I^2 + Q^2$, it follows that P is exponentially distributed with a mean value $\overline{P} = E(P) = E(|V|^2) = 2\sigma^2$:

$$p(P) = \frac{1}{2\sigma^2} \exp\left(-\frac{P}{2\sigma^2}\right) \tag{7}$$

Weather Radar Equation

Apart from the precipitation and clouds, meteorological radars respond to a wide variety of scattering targets including insects and birds, smoke and aerosol particles, refractive index variations, chaff and ground targets. Probert-Jones (1962) derived the weather radar equation for precipitation scattering which relates the average received power $\overline{P}_r$ (Watts) to the transmitted power P_t (Watts) as a function of the range r_0 (m) of the scatterer:

$$\overline{P}_r(r_0) = \left(\frac{cT_0}{2}\right)\left[\frac{P_t G_0^2}{\lambda^2 (4\pi)^3}\right]\left[\frac{\pi \theta_1 \phi_1}{8 \ln 2}\right] \frac{\pi^5 |K_p|^2 Z_e(r_0)}{r_0^2} \tag{8}$$

where G_0 denotes the peak antenna gain (dimensionless), θ_1 and ϕ_1 are the conventional half-power beam widths (rad), T_0 is the pulse width (m) and λ is the wavelength of the radar (m). K_p is the complex dielectric factor (dimensionless) of the target (conventionally, water) so that $|K_p|^2 = |(\varepsilon_r - 1)/(\varepsilon_r + 2)|^2$ where ε_r is the relative permittivity. Z_e is the equivalent reflectivity factor (mm^6m^{-3}) defined as

$$Z_e(r_0) = \frac{\lambda^4}{\pi^5 |K_p|^2} \eta(r_0) \tag{9}$$

where η is the back-scatter cross-section per unit volume (m^2m^{-3}).

In arriving at equation (12), it is assumed that the targets are Rayleigh scatterers that completely and uniformly fill the resolution volume. We also assumed that the beam is Gaussian-shaped and that multiple scattering doesn't occur. This equation also ignores the attenuation of the signal as it propagates through gases, particles and precipitation as

is usually observed in radars operating at X-band and, to a lesser extent, C-band. However, the effect of attenuation can be incorporated in equation (12) by multiplying Z_e with an attenuation factor. The equivalent reflectivity factor Z_e is, by definition, proportional to the sixth moment of the raindrop diameter:

$$Z_e = \int_0^\infty N(D)D^6 \, dD \tag{10}$$

where $N(D)$ ($\text{mm}^{-1}\text{m}^{-3}$) denotes the raindrop size distribution (DSD) in a unit volume (m^3) and N is the diameter of the raindrop (mm). Rainfall rate R (mm/h) being proportional to the raindrop size, forms an empirical relationship with Z_e. The measurement of the received power P_r in weather radar is, therefore, key to extract useful meteorological information.

From equation (12), if $\overline{P}_{ref}$ (dBm) is the received power at the reference antenna port and R (km) is the range of the radar to the resolution volume of the observation, then equivalent reflectivity factor Z_e (dBZ) is given by,

$$Z_e = \overline{P}_{ref} + C + 20 \log_{10} R \tag{11}$$

where C (dB) is the radar constant given by (Bringi and Chandrasekar 2001, p. 334),

$$C = 10 \log_{10} \left\{ \frac{1}{\pi^5 |K_p|^2} \left(\frac{2}{cT_0}\right) \left[\frac{4\pi^3 l_{wg}^2}{P_t G_0^2}\right] \right\} \left(\frac{8 \ln 2}{\pi \theta_1 \phi_1}\right) \lambda^2 10^{21} \tag{12}$$

where l_{wg} is the waveguide loss to compensate measurement at the reference plane. The minimum detectable reflectivity Z_{min} (dBZ) at a particular range is usually defined for signal-to-noise ratio (SNR) of 0 dB. Therefore, the sensitivity of the radar is measured in terms of Z_{min}.

Scattering Polarimetry

In contrast to conventional meteorological radars, the polarization diversity systems provide either for the variation of one or both of transmitted and received wave

polarizations, or provide for dual-channel reception of orthogonally polarized waves. These polarimetric techniques permit measurement of additional precipitation echo characteristics such as mean values and distributions of size, shape, spatial orientation and thermodynamic phase state of the scatterers.

Wave Polarimetry Descriptors

There are several descriptors of wave polarimetry (Cloude 2010). As the electric field evolves in three-dimensional space and time, it traces out a geometrical structure. If we look at the time variation of this structure in a fixed plan transverse to the direction of propagation and, without the loss of generality restrict attention to harmonic plane waves, then this locus is always elliptical. The sense of this polarization ellipse can be described in complex domain by Jones vectors for the completely polarized waves (such as in the case of deterministic scattering from hard targets). The polarization algebra which describes the effect of optical elements on polarization for completely polarized waves by manipulating Jones vectors using complex-valued 2×2 Jones matrices is called Jones calculus (Scherier and Scharf 2010, p. 214).

Polarization state	Jones vector[a]	Stokes vector
Horizontal linear	$[1, 0]$	$[1, 1, 0, 0]$
Vertical linear	$[0, 1]$	$[1, -1, 0, 0]$
Linear at 45°	$\left[\dfrac{1}{2}, \dfrac{1}{2}\right]$	$[1, 0, 1, 0]$
Right-hand (CW) circular	$\left[\dfrac{1}{2}, \dfrac{-j}{2}\right]$	$[1, 0, 0, -1]$
Left-hand (CCW) circular	$\left[\dfrac{1}{2}, \dfrac{j}{2}\right]$	$[1, 0, 0, 1]$

[a]Jones vectors cannot describe partially polarized or unpolarized signals.

Table 1. Polarization algebra
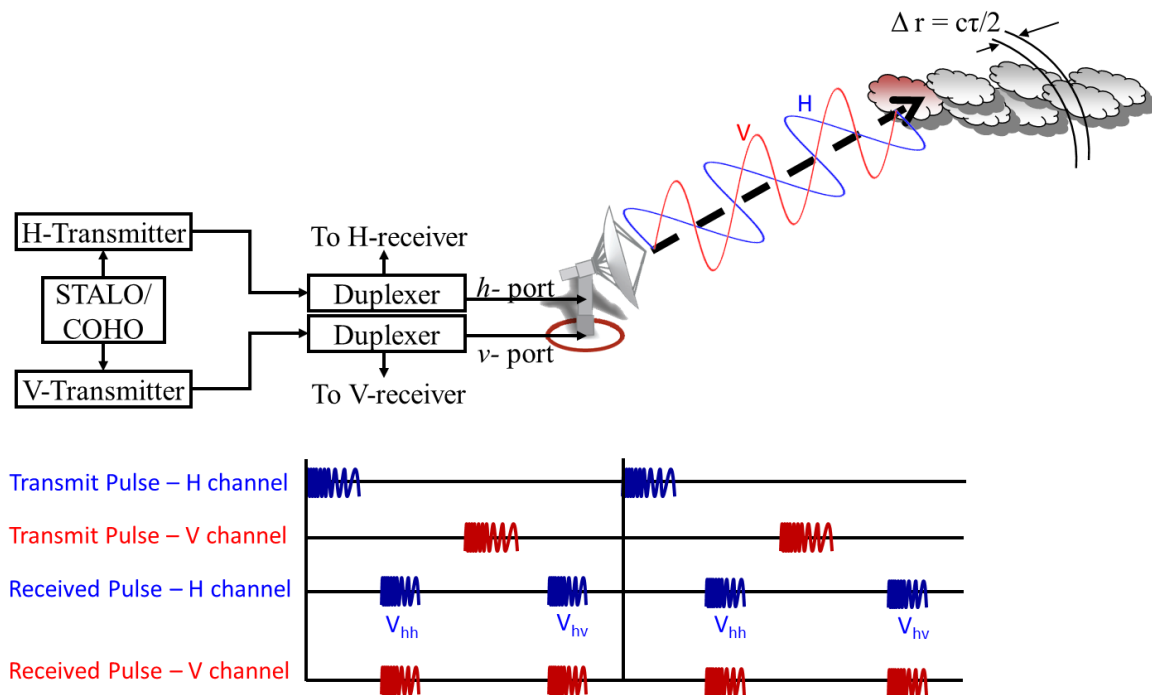
Figure 3. Dual-polarized radar antenna has two ports for the horizontal (H) and vertical (V) polarizations. Each port has a separate transmitter feed synchronized using a STAble Local Oscillator (STALO) or COHerent Oscillator (COHO). The waveform sequence at the bottom depicts alternate transmission. The received voltage V is denoted by twin subscripts: received polarized state is followed by transmit polarized state.

The partially polarized or unpolarized waves (in case of random scattering by precipitation) are described by real-valued Stokes vectors. In 1892, Poincaŕe introduced a spherical visualization of the different states of polarization with the representation of equator as linear polarization, the North Pole as the right-circular polarization and the South Pole as left-circular polarization. The Stokes parameters are the Cartesian coordinates of the points on the sphere or, alternatively, of the parameters of the polarization ellipse. The analog calculus for the manipulation of Stokes vectors using real-valued 4×4 matrix is called the Mueller calculus (Scherier and Scharf 2010, p. 214).

Polarization state	Jones vector[a]	Stokes vector
Horizontal linear	[1, 0]	[1, 1, 0, 0]

Vertical linear	[0, 1]	[1, -1, 0, 0]
Linear at 45°	$\left[\dfrac{1}{2}, \dfrac{1}{2}\right]$	[1, 0, 1, 0]
Right-hand (CW) circular	$\left[\dfrac{1}{2}, \dfrac{-j}{2}\right]$	[1, 0, 0, -1]
Left-hand (CCW) circular	$\left[\dfrac{1}{2}, \dfrac{j}{2}\right]$	[1, 0, 0, 1]

[a]Jones vectors cannot describe partially polarized or unpolarized signals.

Table 1 shows how Jones and Stokes vectors are alternate forms of wave polarimetric descriptors.

The scattering polarimetry i.e., the relationship between the incident wave and the response of the target to the electromagnetic excitation, is described using the scattering matrix representation. Sinclair matrix relates the scattered wave fields to the incident wave fields. In the radar community, the early application of matrix algebra to scattering is due to Edward Kennaugh (Cloude 2010, p. 2). In radar and antenna studies, the Sinclair matrix (Figure 3) is described in backscatter alignment or BSA system as $\boldsymbol{S}_{BSA}$.

Transmission Matrix And Radar Range Equation

Apart from the backscatter matrix description of the target, the other radar polarimetry concept is based on the network theory and depends on the polarization transformation properties of the receiving antenna. The voltage induced in the horizontal (h) and vertical (v) ports of the radar antenna by the back scattered wave can be described in terms of the transmission matrix $\boldsymbol{T}$ in the linear polarization basis as (Bringi and Chandrasekar 2001, p. 178),

$$\begin{bmatrix} V_h \\ V_v \end{bmatrix} = \frac{\lambda G}{4\pi r^2} [\boldsymbol{T}][\boldsymbol{S}_{BSA}][\boldsymbol{T}] \begin{bmatrix} M_h \\ M_v \end{bmatrix} \tag{13}$$

where

$$\boldsymbol{S}_{BSA} = \begin{bmatrix} S_{hh} & S_{hv} \\ S_{vh} & S_{vv} \end{bmatrix}, \tag{14}$$

r is the propagation path distance to the fixed scatterer,

G is the antenna gain (assumed to be same for both horizontal and vertical polarization ports), and

$\boldsymbol{M} = [M_h \quad M_v]^T$ represents the state of transmit polarization ($[M_h = 1, M_v = 0]$ for horizontal and $[M_h = 0, M_v = 1]$ for vertical polarization).

Covariance And Coherency Matrices

Corresponding to the two states of polarization as given by $\boldsymbol{M}$, the received voltage is a vector of four random variables:

$$\boldsymbol{v} = [v_{hh} \quad v_{hv} \quad v_{vh} \quad v_{vv}] \tag{15}$$

where the subscript hv denotes vertical transmit state and horizontal receive state and so forth. The statistical properties of this random vector are expressed by its covariance matrix:

$$E(\boldsymbol{v}\boldsymbol{v}^H) = E\begin{bmatrix} |v_{hh}|^2 & v_{hh}v_{hv}^* & v_{hh}v_{vh}^* & v_{hh}v_{vv}^* \\ v_{hv}v_{hh}^* & |v_{hv}|^2 & v_{hv}v_{vh}^* & v_{hv}v_{vv}^* \\ v_{vh}v_{hh}^* & v_{vh}v_{hv}^* & |v_{vh}|^2 & v_{vh}v_{vv}^* \\ v_{vv}v_{hh}^* & v_{vv}v_{hv}^* & v_{vv}v_{vh}^* & |v_{vv}|^2 \end{bmatrix} \tag{16}$$

This vectorial formulation of voltage measurements can also be expressed in terms of two other scattering vectors: Pauli scattering vector $\underline{k}$ and Lexicographic scattering vector $\underline{\Omega}$ (Lee and Pottier 2009). While $\underline{k}$ representation is closely related to the physical properties of the scatterer, the $\underline{\Omega}$ representation is directly related to the system measurables.

$$\underline{k} = \frac{1}{\sqrt{2}}[S_{hh} + S_{vv} \quad S_{hh} - S_{vv} \quad S_{hv} + S_{vh} \quad j(S_{hv} - S_{vh})]^T \tag{17}$$

$$\underline{\Omega} = [S_{hh} \quad S_{hv} \quad S_{vh} \quad S_{vv}]^T \tag{18}$$

In case of backscattering from reciprocal scatterers, $S_{hv} = S_{vh}$ and the vectors can be represented as:

$$\underline{k} = \frac{1}{\sqrt{2}}[S_{hh} + S_{vv} \quad S_{hh} - S_{vv} \quad 2S_{hv}]^T \tag{19}$$

$$\underline{\Omega} = [S_{hh} \quad \sqrt{2}S_{hv} \quad S_{vv}]^T \tag{20}$$

The statistical description of partial scattering polarimetry can then be represented as either coherency matrix $J = \underline{k} \cdot \underline{k}^H$ or the covariance matrix $\boldsymbol{\Sigma} = \underline{\Omega} \cdot \underline{\Omega}^H$. Coherence is a synonymous term for correlation coefficient, but, in the frequency domain, coherence is more commonly used than correlation coefficient (Scherier and Scharf 2010, p. 211). However, radar observables are directly expressed in terms of the elements of the covariance matrix. For meteorological radars, since the individual scatterers are not only in relative motion but also fluctuate in the shape or orientation aspects, ensemble averaging should also be included in the statistical description. The backscatter covariance matrix is then given by (Bringi and Chandrasekar 2001, p. 137),

$$\boldsymbol{\Sigma} = \left\langle \begin{bmatrix} |S_{hh}|^2 & \sqrt{2}S_{hh}S_{hv}^* & S_{hh}S_{vv}^* \\ \sqrt{2}S_{hv}S_{hh}^* & 2|S_{hv}|^2 & \sqrt{2}S_{hv}S_{vv}^* \\ S_{vv}S_{hh}^* & \sqrt{2}S_{vv}S_{hv}^* & |S_{vv}|^2 \end{bmatrix} \right\rangle \tag{21}$$

where the angle brackets denote ensemble averaging.

Dual-pol Radar Observables

For the dual-polarization radar systems, any two arbitrary polarization states are admissible. However, in general these states are usually either circular or linear. Though circular polarization has been used in the past for rainfall estimation and hydrometeor classification (Hendry and Antar 1984), the linear horizontal and vertical polarizations have become prevalent recently. This is because the linear polarization states do not change as a function of propagation or, alternatively, they are the eigen-polarization states of the precipitation medium for electromagnetic wave propagation (Bringi and Chandrasekar 2001, p. 186). The dual-polarization system discussed here and later is therefore confined to linear polarization systems. Hence, the description of radar observables such as circular depolarization ratio (CDR) (Bringi and Chandrasekar 2001, p. 112) is excluded from the list here.

Once all the elements of the backscatter covariance matrix have been estimated in a so-called fully polarimetric system, several radar observables, which provide useful information about hydrometeor size, shape orientation, spatial distribution and thermodynamic state, can be defined. Following are some of the common dual-polarization radar observables expressed in terms of the scattering matrix parameters.

Copolar backscattering cross-section per unit volume $(m^2 m^{-3})$:

$$\textbf{Horizontal: } \eta_{hh} = \langle n 4\pi |S_{hh}|^2 \rangle \tag{22}$$

$$\textbf{Vertical: } \eta_{vv} = \langle n 4\pi |S_{vv}|^2 \rangle \tag{23}$$

where n is the number concentration of the particles (m^{-3}).

Cross-polar backscattering cross-section per unit volume $(m^2 m^{-3})$:

$$\eta_{hv} = \langle n 4\pi |S_{hv}|^2 \rangle \tag{24}$$

$$\eta_{vh} = \langle n 4\pi |S_{vh}|^2 \rangle \tag{25}$$

$$\eta_{hv} = \eta_{vh} \tag{26}$$

where the last equality is due to (Tragl 1990).

Copolar reflectivity $(mm^6 m^{-3}$ or dBZ$)$:

$$Z_h = \frac{\lambda^4}{\pi^5 |K_p|^2} \eta_{hh} \tag{27}$$

$$Z_v = \frac{\lambda^4}{\pi^5 |K_p|^2} \eta_{vv} \tag{28}$$

Cross-polar reflectivity $(mm^6 m^{-3}$ or dBZ$)$:

The cross-polar reflectivity measures the sum of contributions from different scatterers in the orthogonal polarization (first subscript) than the polarization the scatterers are illuminated with (second subscript).

$$Z_{hv} = \frac{\lambda^4}{\pi^5 |K_p|^2} \eta_{hv} \tag{29}$$

$$Z_{vh} = \frac{\lambda^4}{\pi^5 |K_p|^2} \eta_{vh} \tag{30}$$

Differential reflectivity (dB):

The single measure of reflectivity (Z_h or Z_v) at one polarization (usually horizontal polarization) being dependent on both n and D can lead to large errors in the estimate of attenuation and rain rate. To overcome this problem, the dual-polarimetric weather radars make use of the oblateness of the rain drops and its monotonic relationship with the equivalent drop diameter (Pruppacher and Beard 1970). The oblateness gives rise to a difference in the back-scatter signal between horizontal and vertical polarizations. This additional parameter measured by a dual-polarization radar, is called the differential reflectivity Z_{dr} (Wakimoto and V.N. Bringi 1988)

$$Z_{dr} = 10 \log_{10} \left(\frac{\eta_{hh}}{\eta_{vv}} \right) \tag{31}$$

Linear depolarization ratio (dB):

For scatterers which have a finite canting angle (i.e. with their axis of symmetry tilted from the vertical), the scattering process will cause a small but finite fraction of the transmit (or incident) energy to be depolarized, the contribution of which could be resolved in the direction of the orthogonal polarization. The amount of depolarization, measured as linear depolarization ratio (LDR), will depend on a number of factors, namely, the hydrometeor size, the axis ratio, the degree of canting and the radar beam elevation.

$$LDR_{vh} = 10 \log_{10} \left(\frac{\eta_{vh}}{\eta_{hh}} \right) \tag{32}$$

$$LDR_{hv} = 10 \log_{10} \left(\frac{\eta_{hv}}{\eta_{vv}} \right) \tag{33}$$

Copolar correlation coefficient (dimensionless):

Another parameter which can be measured by a dual-polarization radar is the co-polar correlation coefficient ρ_{co} (zero-lag if polarization switching is used), which is the correlation between horizontally and vertically polarized return signals. This is defined as (Sachidananda and Zrnić 1985). The ρ_{co} is therefore useful for identifying non-rain hydrometeors. Measurements made in rain using horizontally pointing radar beam indicate that ρ_{co} can range from 0.98 (Balakrishnan and Zrnić 1990) to 0.995 (Illingworth and Caylor 1991) (using a high resolution S band radar).

$$\rho_{co} = \frac{|\langle S_{hh} S_{vv}^* \rangle|}{\sqrt{\langle |S_{hh}|^2 |S_{vv}|^2 \rangle}} \tag{34}$$

Differential propagation phase (°):

The oblateness of the drops also causes a difference in the amplitude and phase of the propagating signal, with the result that the horizontally polarized wave will suffer a phase lag relative to the vertically polarized wave. This gives rise to differential propagation phase (ϕ_{dp}) between the H and V polarized waves. In rainfall, the differential propagation phase ϕ_{dp} is known to be a monotonically increasing function of range. If the rain rate is uniform along the path, ϕ_{dp} increases by a fixed amount per unit distance along range. If we define ϕ_{HH} and ϕ_{VV} cumulative differential phase shift for the total round trip between the radar and the resolution volume for horizontal and vertical polarizations respectively, then

$$\phi_{dp} = \phi_{HH} - \phi_{VV} \tag{35}$$

Backscatter differential phase (°):

Backscatter differential phase (δ) becomes significant in Mie region, i.e. when the radar wavelength is comparable to the size of the scatterers. It is largely negligible in rain at S-band whereas at X-band and even at C-band, it can become noticeable in the measured ϕ_{dp} range profiles as a local perturbation on the monotonically increasing differential

propagation phase. Although not used for quantitative estimation of rainfall rates, the parameter δ helps to identify non-precipitation echoes, such as those arising from birds.

$$\delta = \angle(\langle S_{vv} S_{hh}^* \rangle) \tag{36}$$

Co-cross-polar correlation coefficients (dimensionless):

These quantities are primarily dependent on the characteristics of hydrometeor orientation, i.e. the canting angle distribution. In particular, the mean and the rms width of the canting angle distribution in rain can be estimated approximately from ρ_{cx}^h and ρ_{cx}^v (Ryzhkov et al. 2002), when combined with Z_{dr} and LDR. Other applications are (i) detection of aligned crystals – indicated by pronounced ρ_{cx}^h and ρ_{cx}^v signatures – which could be used to locate electrically charged regions in clouds and (ii) radar hardware assembly quality checks (in particular antenna/feed) such as undue coupling between the two orthogonal channels.

$$\rho_{cx}^h = \frac{|\langle S_{hh} S_{hv}^* \rangle|}{\sqrt{\langle |S_{hh}|^2 |S_{hv}|^2 \rangle}} \tag{37}$$

$$\rho_{cx}^v = \frac{|\langle S_{vv} S_{hv}^* \rangle|}{\sqrt{\langle |S_{vv}|^2 |S_{hv}|^2 \rangle}} \tag{38}$$

Mean Doppler velocity (m / s):

For a symmetric Doppler spectrum , the estimate of mean velcoity can be calculated from the autocorrelation at lag 1 of received complex voltage time-series at horizontal polarization.

$$\hat{\bar{v}} = -\frac{\lambda}{4\pi T_s} \angle(r_{vv}[1]) \tag{39}$$

where λ is the radar wavelength, T_s is the pulse repetition or sampling time and $r_{vv}[1]$ is the autocorrelation of received voltage time-series at lag 1.

Spectrum width (m / s):

The Doppler spectrum of weather echoes has a Gaussian shape. The variance of this distribution or the spectrum width is the measure of shear and turbulence. Also, a faster antenna rotation rate has the effect of broadening the weather echo spectrum. For the uniform pulsing scheme, the estimate of the spectrum width is calculated using autocorrelation at lag 0 and lag 1 for received voltage time-series horizontal polarization:

$$\widehat{\sigma_v} = \frac{\lambda}{2\pi T_s \sqrt{2}} \left[\ln \left| \frac{r_{vv}[0]}{r_{vv}[1]} \right| \right]^{1/2} \tag{40}$$

<u>Evolution Of Short Wavelength Weather Radars</u>

It is widely accepted that precipitation monitoring is difficult because of its high spatial and temporal variability (see e.g., Wilson and Brandes 1979; Zawadzki 1982; Krajewski and Smith 2002); nonetheless, rainfall remains one of the most critical variables in many hydrological applications (Battan 1973; Chow et al. 1988). A number of studies and experiments have used rain gauges and disdrometers to establish the spatio-temporal variability of rainfall with direct *in situ* measurements (Ciach and Krajewski 1999a, b); a detailed exposition of these ground-based methods can be found in Habib et al. (2010). However, these instruments do not yield precipitation measurements in the space-time continuum. On the other hand, while the wide use of modern weather radar systems has enabled continuous rainfall measurements in the space-time domain (Doviak and Zrnić 1993; Bringi and Chandrasekar 2001; Bringi et al. 2007), this feature compromises the accuracy of the radar rainfall products when compared with the *in situ* estimates (see e.g., Krajewski et al. 1996; Seo and Smith 1996; Smith et al. 1996; Gebremichael and Krajewski 2004; Tabary 2007). We refer the reader to Villarini and Krajewski (2010) for an exhaustive review of the errors in radar rainfall estimates.

High-resolution fast-scanning radars should be deployed to combat the differences in spatio-temporal resolutions of radar and rain-gauge sampling regimes. However, the

sampling geometry, resolution, and temporal coverage of the conventional S- and C-band weather radars, which constitute many national weather radar networks (Klazura and Imy 1993; Lapczak et al. 1999; Gekat et al. 2004), are designed primarily to observe mesoscale weather phenomena. Further, popular NEXRAD hourly rainfall estimates are available at 4 km $\times$ 4 km resolution (Lin and Mitchell 2005), while there is evidence that rainfall variability is significant below this resolution (Krajewski et al. 2003). The low resolution of these radars is incapable of detecting microbursts, scattered storms, or other weather events (such as tornadoes) at far ranges (e.g., > 50 km) in the lower troposphere. More importantly, detailed observations of rainfall at the near-ground level remain undetected in S- and C-band radars at far ranges. Therefore, it has become increasingly more common to use shorter wavelengths, such as those in the X- and Ku-bands, to enhance the S/C-band rainfall observations and monitor the precipitation variability at scales smaller (e.g. basin) than the available products from the longer-wavelength radars (see e.g,. McLaughlin et al. 2009; Maki et al. 2010; Yoshikawa et al. 2010).

Employing a network of several identical units often compensates for X-band radars' lack of spatial coverage. This strategy has proved economically and operationally feasible, as demonstrated by X-band networks such as those used by the Center for Collaborative Adaptive Sensing of the Atmosphere (CASA) Integrated Project 1(IP1) (McLaughlin et al. 2009), X-RAIN (X-band Polarimetric RAdar Information) (Maki et al. 2010), and the Tropical Radar Network (TropiNet) (Galvez et al. 2009). The objective of these X-band weather radar networks is to retrieve meteorological echoes in the lower troposphere and to adapt to rapidly changing, severe weather. The hydrological quest (Krajewski et al. 2010) to finely resolve rainfall in space and time remains secondary to the stated objectives of such X-band networks. Therefore, the research in hydrology would benefit greatly from an X-band weather radar network that focuses exclusively on the hydrological aspects of radar rainfall estimation.

Iowa XPOL System

With the objective of conducting hydrology-focused research and obtaining accurate quantitative estimation of rainfall at a high temporal and spatial resolution, The University of Iowa has acquired four scanning, mobile, X-band polarimetric (XPOL) Doppler weather radars. Iowa procured these XPOLs from Prosensing Inc. under the Major Research Instrumentation (MRI) grant funded by the National Science Foundation (NSF). The Iowa XPOL system's distinct engineering and operational abilities facilitate the study of near-ground hydrological processes at smaller scales. Several of the XPOL radar system's features make it more appealing to the hydrology community than the existing networks of X-band weather radars. Firstly, while many existing X-band weather radars are installed on tower-tops, the Iowa XPOL radars are mounted on mobile platforms. Consequently, Iowa XPOLs can be deployed at any location of interest and provide better near-ground observations than those basins that were previously covered by only 4 km × 4 km NEXRAD pixels. Secondly, because XPOL systems can acquire data at a programmable range oversampling which can be as low as 7.5 m, they provide more accurate polarimetric estimates without decreasing the scan rate (Torres and Zrnić 2003). Thirdly, unlike existing X-band networks, the Iowa XPOL network provides very high-resolution precipitation profiles of up to 15 m range resolution. In a previous study, Schneebeli et al. (2013) used an X-band radar unit similar to the Iowa XPOLs to observe high-resolution vertical profiles in the alpine region. The Iowa XPOLs can facilitate similar studies for the Great Plains region of the Midwestern United States and capture multiple high-resolution snapshots of the same storm from different angles. The radars are intended to serve multiple areas of hydrological research, including uncertainty modeling, urban hydrology, flood and flash-flood prediction, and soil erosion.

X-band weather radars have been used for important hydrological studies concerning the spatio-temporal variability of rainfall (see e.g., Delrieu et al. 1999; Berne and Uijlenhoet 2006; Uijlenhoet and Berne 2008; Scipión et al. 2013). A detailed

observational study using an X-band radar operating at a spatial resolution of 120 m and temporal resolution of 16 s can be found in Van de Beek et al. (2010). The CASA radars typically operate at range resolutions of 100 m or 50 m with a scan rate of $12°s^{-1}$ (McLaughlin et al. 2009). Similarly, mobile X-band radars such as Agenzia Regionale per la Protezione Ambientale (ARPA) Piemonte (ARX), operating at a range resolution of 125 m and a beamwidth of 1.3°, have previously been used (Cremonini et al. 2010). Kabeche et al. (2010) have analyzed quantitative precipitation estimates obtained from a network of X-band radars operating at 300 m. Pazmany et al. (2013) have deployed a mobile X-band radar that employs a traveling wave tube amplifier (TWTA) to study severe storms and tornadoes at a minimum range resolution of 15 m and azimuthal scan rates of $180°s^{-1}$. (Borque et al. 2014) have also actively used an X-band network to assist in cloud radar studies. Compared to these existing applications, the mobile Iowa XPOLs push the range resolutions at 3 cm regimes to smaller scales, of the order of 15 m, enabling detection of detailed precipitation structures at finer scales with an acceptable accuracy. While the cross-beam resolution clearly remains limited here, the flexibility in deployment and operation of each of these low-cost XPOL units aids in achieving our research goals that we briefly describe in the following subsection.

Scientific Objectives

As previously discussed, while conventional lower frequency (S- and C-band) weather radar data are limited to 100-300 m range resolution, the Iowa XPOL system can provide radar rainfall data at higher range resolutions. Further, the radars are configured to observe target-of-opportunity storms from multiple look-angles within narrow high spatio-temporal windows. Such observations of the same precipitation event with several radars can mitigate signal attenuation due to precipitation at the X-band (Krajewski 2007). The Iowa XPOL data can be used to model the spatial dependence of the errors at smaller scales, which is useful when constructing input for ensemble-based predictive models.

Another key scientific goal is to understand the scaling behavior of rainfall below the scale of about 1 km. The XPOLs are capable of range over-sampling up to 7.5 m and making observations at the range resolution of 30 m. There are very few studies that have been carried out at this scale. For example, a range spacing of 7.5 m can provide several data points within 0.5 km sampling radius around a range gage. This has a potential of bringing the radar measurements even closer to the rain gage in space-time continuum. Indeed, the rain gages were strategically placed within the coverage of XPOLs to generate this kind of data during the IFloodS campaign. Eventually, the fully-operational XPOLs are expected to aid in more elaborate applications of urban hydrology and flash-flood prediction.

Technical Specifications

Table 2 lists the salient technical parameters of the Iowa XPOL radars. Each of the Iowa XPOL radars is deployed on a flatbed trailer mounted system and is capable of taking measurements at remote and secure locations where power and Internet facilities are available. The trailer platform enables the use of a parabolic antenna dish that is 6 ft. in diameter - slightly larger than the 4 ft. dish used in tower-mounted X-band radars (McLaughlin et al. 2009) - leading to enhanced azimuthal resolution. The radars are equipped with an on-site uninterrupted power supply (UPS) and can be controlled and monitored remotely over the Internet. Essentially, each unit is a self-reliant system with an on-site, on-demand archiving capability for raw time series and polarimetric products, GPS (Global Positioning System) enabled time and location information, and Internet access to archived data. The transmitter is magnetron-based with a peak output power of 25 kW. The radars can operate in staggered pulse repetition time (PRT) (Zrnić and Mahapatra 1985) and dual-PRF pulsing modes and can process data using either standard pulse-pair or spectral mode techniques. An advanced signal processor computes the polarimetric estimates in multiple modes such as auto-covariance and spectral processing

(Doviak and Zrnić 1993) at selectable range resolutions and range oversampling ratios. At the default range resolution of 75 m, the radars have a clear air sensitivity of -5 dBZ at a range of 10 km, which allows the radar to observe light to heavy precipitation up to a maximum unambiguous range (R_{max}) of 40 km (Figure 4).
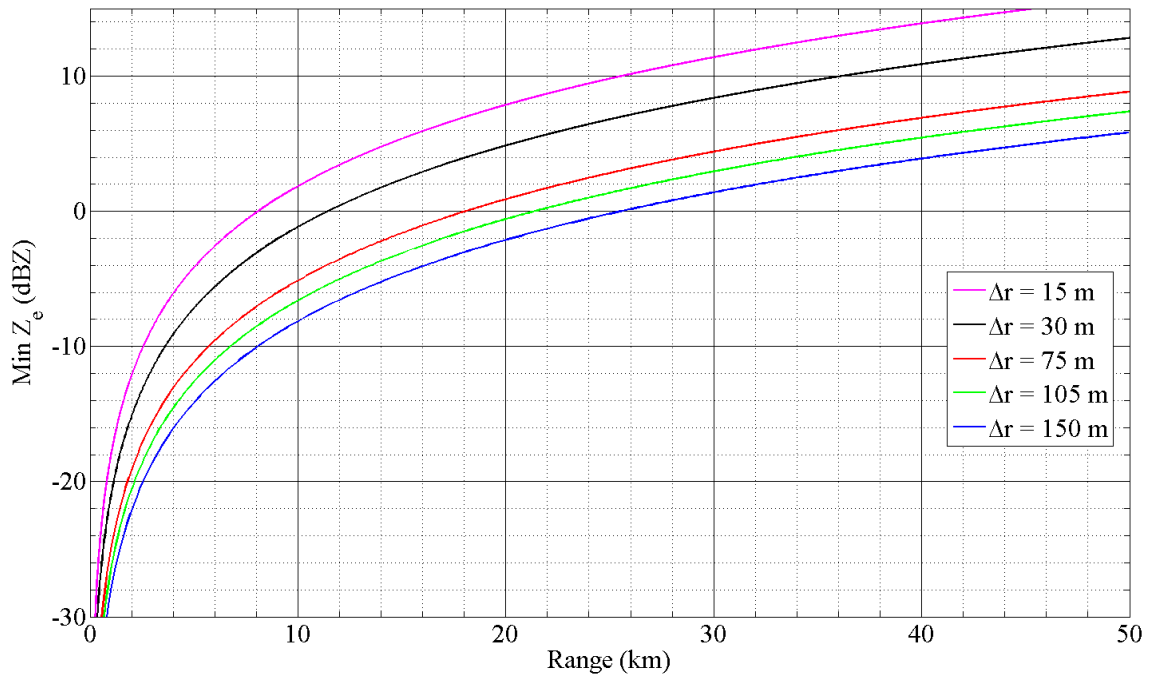
Figure 4. Expected sensitivity of Iowa XPOL radars for different range resolutions (Δr).

The XPOL radar has a magnetron-based transmitter system, whose output frequency is nominally centered around 9.41 GHz. The receiver is composed of two physically separate, identical RF (Radio Frequency) hardware paths consisting of an assembly of microwave limiters and low noise amplifiers (LNA). The output of the radar STALO (STAble Local Oscillator) – in this case, a dielectric resonant oscillator (DRO) – is passed through a receiver splitter to the microwave mixers of horizontal (H) and vertical (V) polarization chains in order to translate the signal from the RF to an IF (Intermediate Frequency) of 60 MHz. The transmit signal is also translated to 60 MHz and then

sampled in the V-channel IF using a Single-Pole-Double-Throw (SPDT) switch that is located before the microwave IF filters. A digital receiver subsamples the 60 MHz IF signal at the sampling rate of 80 MSPS (Mega Samples Per Second). For an overview of the theory and detailed operation of weather radar digital receivers and related terminology used here, please refer to Mishra (2012). The downconverted in-phase (I) and quadrature-phase (Q) data are downsampled using a Cascaded Integrator-Comb (CIC) filter chain and are eventually filtered by a Finite-Impulse Response (FIR) decimator operating at a programmable bandwidth and decimation rate. The digital data processor receives the I/Q time series data over a Peripheral Component Interconnect eXtended (PCI-X) interface.

Technical Characteristic	Description
System	
Nominal R_{max}	40 km
Range resolution	Selectable 15-150 m
Sensitivity	-5 dBZ at 10 km at range resolution of 75 m
Mounting platform	8 x 10 ft customized trailer
Power supply	On-site and trailer-mounted UPS
Time-location sync source	On-site GPS
Radar and antenna controller	Remote operated web-interface
Antenna	
Shape	Parabolic
Polarization	Dual-polarized
Diameter	6 ft
Gain	42 dBi
3-dB beam width	1.3-1.5°
Cross-polarization isolation	~30 dB
Maximum Voltage Standing Wave Ratio (VSWR)	~1.25
Scanning	Az: 0-360°, El: 0-90°
Transmitter	
Operating frequency	9.41 GHz

Transmitter	Magnetron Peak power $P_t = 25$ kW
Pulsing schemes	Staggered PRT and dual-PRF
Receiver	
RF Receiver Gain	~33 dB
Cross-channel receiver isolation	>50 dB
Noise Figure	~3 dB
Dynamic range	80 dB
Digital noise floor	-84 dBm (at 2 MHz receiver bandwidth)
Signal and data processor	
Digital receiver bandwidth	Selectable 2-20 MHz
Range oversampling	Programmable 7.5-75 m
Processing modes	Standard pulse pair, dual pulse pair, FFT
Data Products	
Data archiving	On-site on-demand for raw timeseries and processed products
Archived products	<u>Standard moments</u>: Equivalent reflectivity factor (Z_h, Z_v), Doppler velocity (v) and Doppler spectrum width (σ_v) <u>Dual-pol products</u>: Differential reflectivity (Z_{dr}), copolar correlation coefficient (ρ_{hv}) and differential propagation phase (ϕ_{dp}) <u>Derived products</u>: Instantaneous rainfall rate, specific differential phase (K_{dp})
Available data format	NetCDF

Table 2. Technical specifications of a typical unit in the Iowa XPOL radar system.

CHAPTER 3

CS CONSIDERATIONS FOR WEATHER RADAR

As discussed in Chapter 1, application of CS to the radar scenario requires sparsity of target echoes in a certain domain. Also, the measurements should be incoherent. In this chapter, we examine these two considerations for weather radar.

Sparsity: Point Targets Versus Weather

Most of the current research on applying CS to radar applications is concentrated on point target radars (Ender 2010). For example, an aircraft surveillance radar display typically tracks a finite number of aircrafts that is very small compared to the totalk number of resolution cells. Figure 5(a) illustrates a typical radar display for an aircraft surveillance radar, in which every red dot indicates an aircraft. For the radar scenario, spatial domain has same connotation as the time domain since every spatial sample is acquired at a different time. Therefore, one can also refer this dictionary as range-time or space-time. It is obvious that the point target radar signals are sparse in spatial range-time domain. The radar signals from point targets are sparse in frequency domain, too (Fannjiang et al. 2010). This is because the corresponding spectrum shows only a finite number of Doppler frequencies, as shown in simulation of Figure 6(a).

The recognizable sparsity of point targets is not available for volumetric targets such as precipitation. Figure 5(b)-(d) show that the precipitation target need not always be sparse in spatial domain. Also, unlike point targets, the power spectral density of the weather echo is Gaussian (Doviak and Zrnić 1993) and occupies a continuum of spectrum, as shown in simulation of Figure 6(b). Therefore, in general, precipitation is neither sparse in spatial domain nor in Doppler domain. The CS techniques exploiting range-time and frequency sparsity of point target radars are, thus, not directly applicable to weather radars.
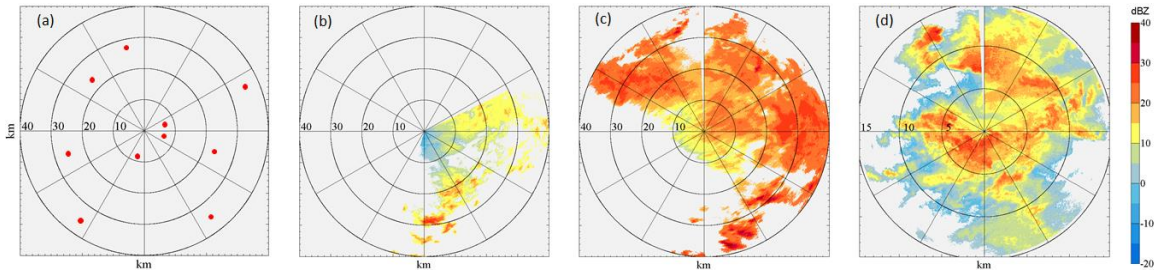
Figure 5(a) Point targets on a radar display. (b) Spatially sparse precipitation. (c) Precipitation is sparse along only some of the range profiles. (d) No spatial sparsity for precipitation. The precipitation data shows the horizontal reflectivity for the storms observed on Jun 13, 2013 by the Iowa XPOL-2 radar during the NASA IFloodS campaign (Mishra et al. 2014).
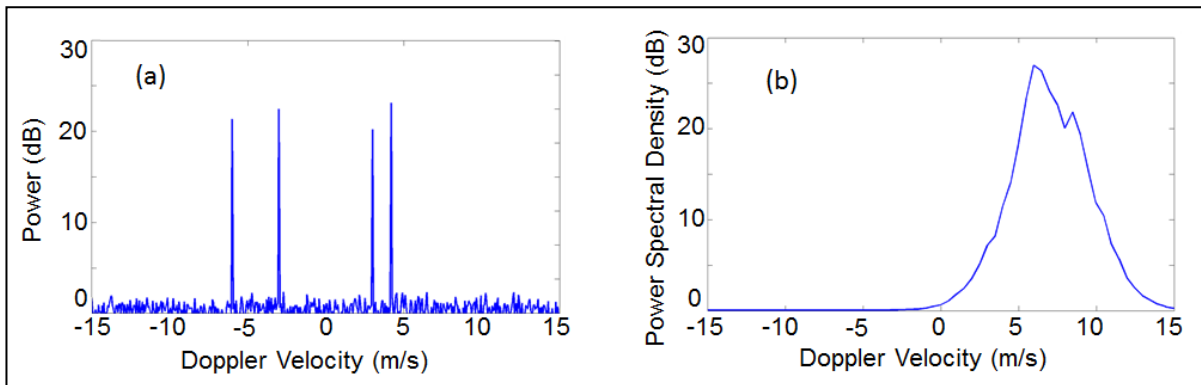
Figure 6. Typical Doppler spectra for (a) point targets and (b) weather echo in white noise using pulse repetition frequency = 2 kHz for an X-Band radar. Two incoming and two outgoing point targets are shown in (a). In (b), the estimated parameters are velocity ≈6 m/s and spectrum width ≈ 3.5 m/s. The simulation of weather echoes follows the algorithm specified in (Chandrasekar et al. 1986).

Some of the existing research on volumetric target CS-radar is dedicated to meteor detection radars. Meteors are not point targets, but they are localized in range-time. A joint time-frequency sparsity of such targets has been exploited to extract the benefits of the high-resolution radar, as shown in (Volz and Close 2012). Although highly localized precipitation can appear sparse in joint time-frequency domain, as depicted by the Short-Time Fourier Transform (STFT) of weather echo in Figure 7, such
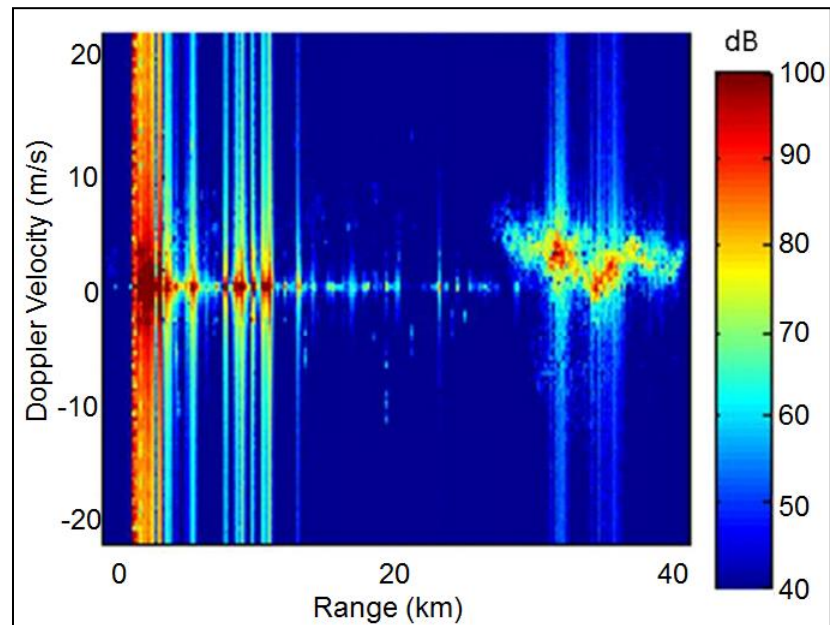
Figure 7. STFT of precipitation echoes. The precipitation signal appears at 23-40 km and is localized in Doppler domain. The straight lines in nearer range correspond to ground clutter and other interference. This data was collected by XPOL-2 on Jun 13, 2013.

scenarios are quite infrequent in observed weather.

There have been attempts to use CS in weather radars for specialized tasks such as refractivity retrieval (Yu et al. 2011) and imaging using phased-array antennas (Ozturk et al. 2013). A related application is downscaling (Venugopal et al. 1999), where the sparsity of precipitation image in wavelet domain is used to form a high-resolution precipitation image from low-resolution measurements (Ebtehaj et al. 2012). Downscaling adds details to a low-resolution image using CS, but the radar data is obtained using conventional scanning. Further, downscaling operates on the image of the data rather than directly on received radar signal.

Incoherence Considerations

There are several incoherence strategies discussed in other CS-based radars. One of the strategies to ensure incoherence for point target radars is to transmit an incoherent waveform such as an "Alltop" sequence (Herman and Strohmer 2009). This particular approach to CS-based radar increases the measurement resolution and simplifies the radar hardware by eliminating the matched filter stage in the receiver. Another approach to incoherence samples the same target scene using multiple radars on ground (Yu et al. 2012b). The incoherence of the measurements can also be achieved by deploying an array of antenna elements. By randomly choosing the elements of antenna array transmit-and-receive, such a CS-based radar is shown to recover the sparse or approximately sparse target scene (Fannjiang et al. 2010). This strategy is the easiest choice to achieve incoherence in spaceborne weather radars, since they invariably always employ phased array antenna.

For the ground-based weather radars, incoherence can be achieved by randomly selecting only a few time samples to pass through the receiver. This approach however would require scanning the entire target scene and then discard many samples randomly. An alternative can be setting the radar antenna to scan at a very high scan rate. In general, a scanning weather radar produces meteorological estimates by averaging over several azimuths. Therefore, should the radar to scan at a very fast scan rate, it would then dwell less on each azimuth and would randomly "miss" other azimuths (which would have been dwelled by the radar at a normal scan rate). This scan strategy would then produce randomly sensed samples (fewer than a slower scan rate) for each range cell.

In a possible scenario when such a scan is, indeed, constructed, the other pertinent question to ask is how one can construct the distributed weather echoes from a sample of its entries. We address this question in next chapter.

CHAPTER 4

MATRIX COMPLETION FOR CS-BASED WEATHER RADAR

Although weather radar signals cannot be modeled as sparse in conventional dictionaries such as time and frequency, the backscattered signal in a weather radar is coherent (Keeler and Passarelli 1990). In other words, the motion among the precipitation scatterers is small compared to the radar wavelength, so their relative positions produce highly correlated echoes from sample to sample and scan to scan. This inherent redundancy in weather radar signals implies that the range-azimuth scan of precipitation echoes can be modeled as a low-rank matrix.

Weather Signal As a Low-rank Matrix

Low-rank matrices are the multi-dimensional equivalents of one-dimensional sparse vectors. Given a matrix $M \in \mathbb{R}^{m \times n}$, its singular value decomposition (SVD) is given by, $M = USV^T, U \in \mathbb{R}^{m \times r}, V \in \mathbb{R}^{r \times n}$, and $S = \text{diag}(\sigma_1, \cdots, \sigma_r)$, where $\sigma_1 \geq \cdots \geq \sigma_r > 0$ are the unique singular values and $r \leq \min(m, n)$ is the rank of the matrix. For a low-rank matrix, most diagonal elements of S are zero such that, $r \ll \min(m, n)$. The best r'-rank approximation $\widetilde{M}$ of the matrix M is given by zeroing out the $r - r'$ smallest singular values so that, $\widetilde{M} = U\tilde{S}V^T$ and $\tilde{S} = \text{diag}(\sigma_1, \cdots, \sigma_{r'}, 0, \cdots, 0)$.

This sparsity has been illustrated in Figure 8(a) using real radar data from Iowa XPOL-2 radar. Figure 5(a), depicted as spatially non-sparse precipitation shows original observations of horizontal reflectivity Z_h which is a 1930 (range gates) by 413 (azimuthal rays) matrix. A plot of eigen-values of this matrix Figure 8(b) shows a large fraction of eigen-values are very small or close to zero. This is due to the highly correlated nature of weather signal both temporally as well as spatially. Figure 2 shows the effect of low-rank approximation on the original weather echo. During eigen-decomposition of the matrix, we retain only a fraction of the eigenvalues and set others to zero. Subsequent figures are derived at various degrees of low-rank approximations of the original reflectivity matrix.

We note that a very small fraction of detailed features are lost, and low-rank versions are statistically identical to the original matrix, illustrating the sparsity of the real radar data.

(a)   (b)
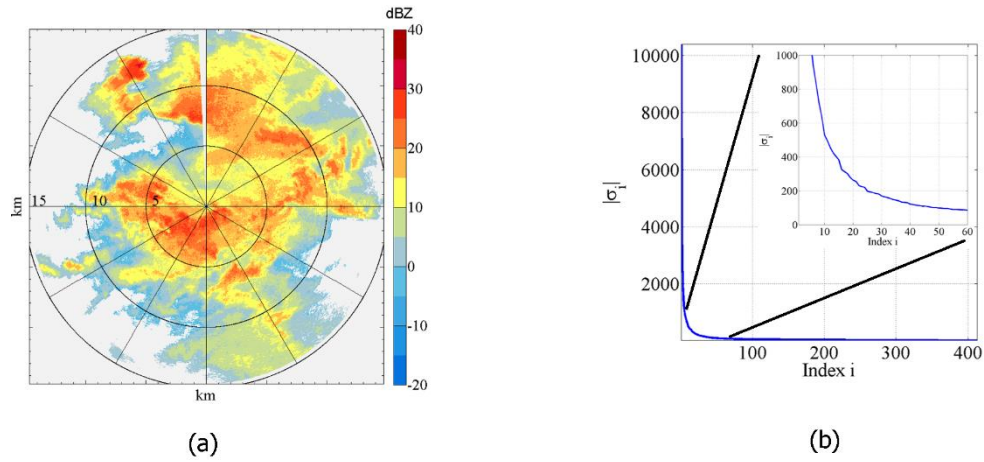
Figure 8. (a) Spatially non-sparse precipitation signal (b) A plot of absolute value of eigenvalues of the data matrix plotted in (a).
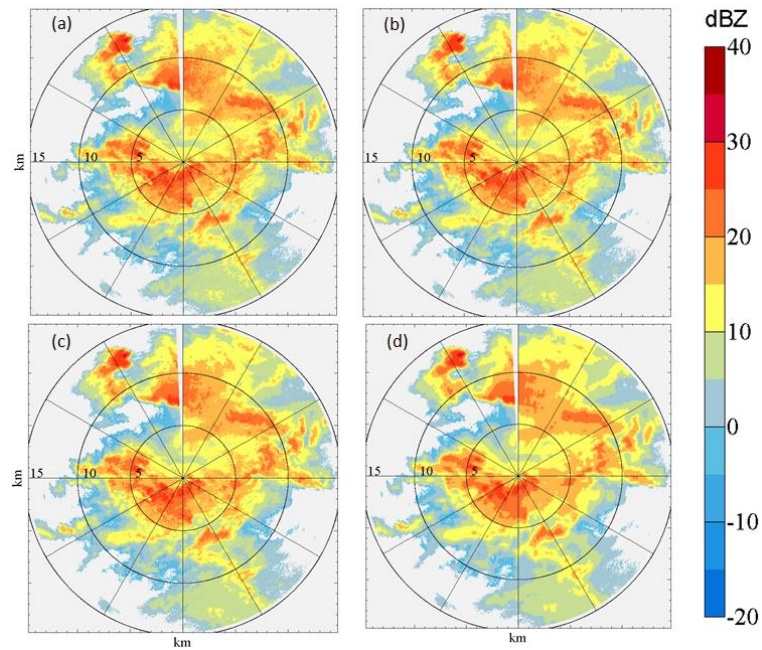
Figure 9. (a) Observed Z_h on Iowa XPOL-2 radar on Jun 13, 2013. Low-rank Z_h using (b) 40% (c) 25% (d) 5% of the significant eigen-values.

Reconstruction Algorithm

Current research in matrix completion shows that it is possible to recover all the elements of the low-rank matrix from a sample of its entries (Candès and Recht 2009). Let Ω denote the set of the locations of the partially observed entries of the original low rank matrix M. Then, intuitively, recovering M corresponds to the rank minimization problem:

$$(P_0') \qquad \begin{array}{c} \text{minimize } rank(\boldsymbol{X}) \\ \text{subject to } X_{ij} = M_{ij}, (i,j) \in \Omega \end{array} \qquad (41)$$

However, like problem P_0, rank minimization is also intractable and very difficult to solve. The approach to low-rank matrix completion is therefore to solve the matrix equivalent of problem P_1, i.e., minimization of the nuclear-norm $\|\boldsymbol{X}\|_* = \sum_k \sigma_k$ where σ_k denotes the kth eigen-value:

$$(P_1') \qquad \begin{array}{c} \text{minimize } \|\boldsymbol{X}\|_* \\ \text{subject to } X_{ij} = M_{ij}, (i,j) \in \Omega \end{array} \qquad (42)$$

This approach for weather radars is illustrated in Figure 10. Figure 10(a) reproduces original Z_h from Figure 8(a). Figure 10(c) shows 30% of entries sampled randomly from the low-rank approximation Figure 10(b) of Figure 10(a). Here, solely for illustration purposes, we chose the 25% low-rank approximation shown in Figure 9(c). Figure 10 (d) shows recovery of remaining entries based on partial observations of Figure 10(c). As the matrix size grows bigger, the nuclear norm minimization requires faster algorithms. Figure 10(d) was generated using singular value thresholding (SVT) (Cai et al. 2010) – one of the several popular large-scale matrix completion algorithms that rely on nuclear norm minimization. Figure 10(e), (f) and (g) show the distribution of Z_h for Figure 10(a), (b) and (d). Although the illustrated reconstruction uses a low-rank approximation $\tilde{Z}_h$ as matrix M, the results are not very different if Z_h itself is used with

some modifications to problem P_1 (the relative errors ε_1 and ε_2 are of the same order), as we show next. The very close similarity of the reconstructed data distribution with the original clearly illustrates the potential of CS for weather radars. The low-rank nature of weather signal enables application of various other extension of CS to weather radar. We discuss these extensions in Chapter 5.

$$\varepsilon_1 = \frac{\left\| Z_h - \hat{Z}_h \right\|_{\mathcal{F}}}{\left\| Z_h \right\|_{\mathcal{F}}} = 0.0917$$

$$\varepsilon_2 = \frac{\left\| \tilde{Z}_h - \hat{Z}_h \right\|_{\mathcal{F}}}{\left\| \tilde{Z}_h \right\|_{\mathcal{F}}} = 0.0732$$
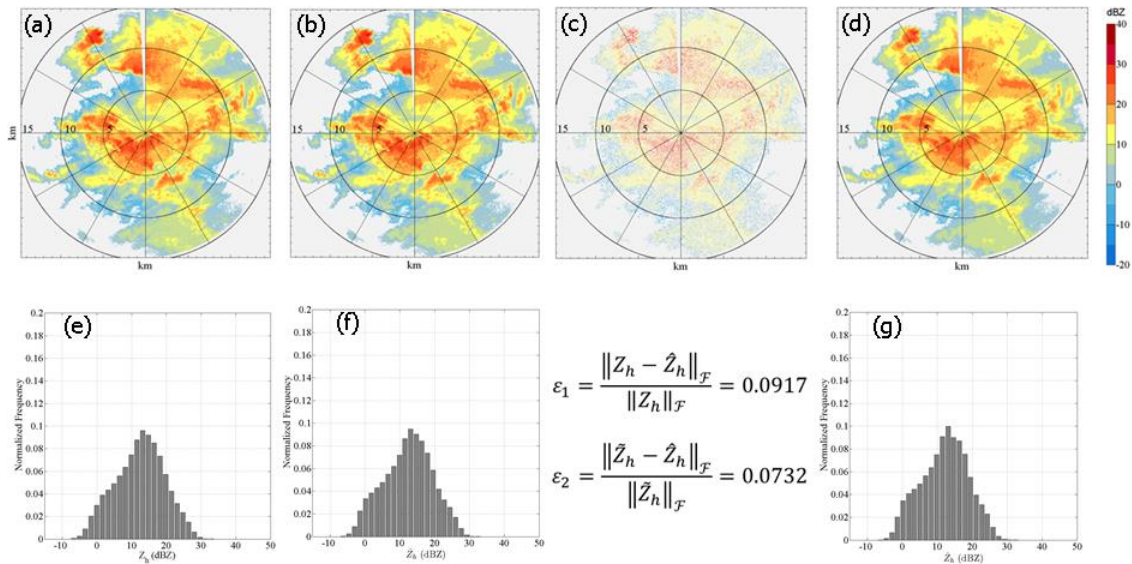
Figure 10. Illustration of reconstruction of precipitation echo using matrix completion. (a) Original Z_h (b) $\tilde{Z}_h$: low rank approximation of original Z_h using only 25% singular values (c) $P_\Omega(\tilde{Z}_h)$: Randomly sub-sampled entries of the low-rank $\tilde{Z}_h$ matrix. (d) $\hat{Z}_h$: Recovered Z_h (e) Distribution of Z_h for original data matrix (f) Distribution of $\tilde{Z}_h$ for low-rank approximation of original data matrix (g) Distribution of $\hat{Z}_h$ for recovered data matrix. The two error metrics ε_1 and ε_2 are of the same order.

In practice, the radar would not be sampling from the low-rank approximation of the data. The radar samples weather directly, and therefore, the reconstruction should be

based on sparse sampling of measured data. Figure 11 illustrates the reconstruction directly from the original matrix using the Low Rank Matrix Fitting (LMaFit) (Shen et al. 2014; Wen et al. 2012). This algorithm is much faster than SVT but comes at the expense of the accuracy. We note that the error increases by an order using the LMaFit algorithm that contains a collection of solvers that can be used to solve various classes of low-rank matrix optimization problems. The same reconstruction using SVT algorithm exhibits lower errors. Still, nuclear norm minimization problems can become excessively costly as problem sizes and ranks increase. As a result, algorithms based on nuclear norm minimization so far only have limited capacity for solving large-scale problems due to their slow speed when ranks are not extremely low.

$$\varepsilon_1 = \frac{\|Z_h - \hat{Z}_h\|_{\mathcal{F}}}{\|Z_h\|_{\mathcal{F}}} = 0.1001$$
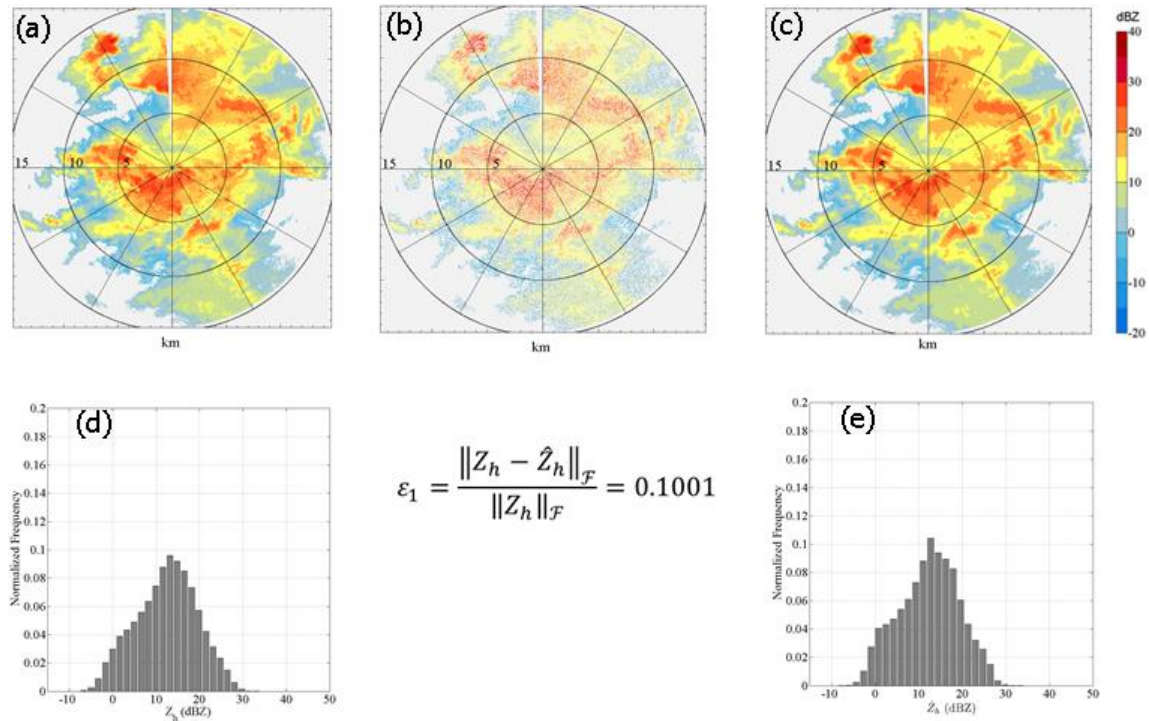
Figure 11. Illustration of reconstruction of precipitation echo using matrix completion by sampling directly from the original matrix. (a) Original Z_h (b) $P_\Omega(Z_h)$: Randomly sub-sampled entries of the low-rank $\tilde{Z}_h$ matrix. (c) $\hat{Z}_h$: Recovered Z_h (d) Distribution of Z_h for original data matrix (e) Distribution of $\hat{Z}_h$ for recovered data matrix.

<u>Comparison With Related Research</u>

It is natural to compare the matrix completion for precipitation echoes with some related algorithms such as radar data compression (Kruger and Krajewski 1997), image interpolation (Sonka et al. 2014) and downscaling (Ebtehaj et al. 2012). However, there are qualitative differences in the applicability of these algorithms for the problem we intend to address. Therefore, these comparisons are at best red-erring in this research. We now explain the problems with each of these algorithms.

<u>Data Compression</u>

Since the weather radar data is voluminous, there has been considerable interest in efficiently storing the weather radar data in a compressed format. Kruger and Krajewski (1997) developed an improved format called ASCII Run Length Encoding (RLE) that offers several attractive features, among them a compression ratio of about 15:1. This format offers preservation of all data values, efficient storage, fast access, modularity, and portability across different platforms. The standard data compression techniques such as UNIX utility compress do not offer the above features. To access a particular data point, e.g., reflectivity value over a rain gage, the data must be decompressed first through a time consuming procedure. The disadvantage of this becomes obvious during studies that require multiple passes over the same data. This is a typical situation in research where it is impossible and/or restrictive to anticipate all possible data uses and analyses. As a result, the researcher ends up repeating similar computations many times.

The sparse sensing of weather addresses a different problem, i.e., how to sample frugally in real-time without losing much information. This is not same as lossless compression of the data that has already been collected by the radar using conventional (slower) scanning methods. The lossless compression offers a technology to efficiently store weather data thereby leading to less memory requirements. The sparse sensing leads

to faster scanning and tracking of storms in real-time and later recovering the missing samples using different reconstruction algorithms.

Image Interpolation

Another obvious comparison of sparse sampling could be with the 2-dimensional (2D) interpolation of the data to recover missing values. The 2D interpolation is common in image processing and computer vision applications. We refer the reader to Sonka et al. (2014) for details on various image interpolation algorithms. The purpose of interpolation is to render a visibly similar image after the original image has been subjected to some geometric transformations.

$$\varepsilon_1 = \frac{\|Z_h - \hat{Z}_h\|_{\mathcal{F}}}{\|Z_h\|_{\mathcal{F}}} = 0.1220$$
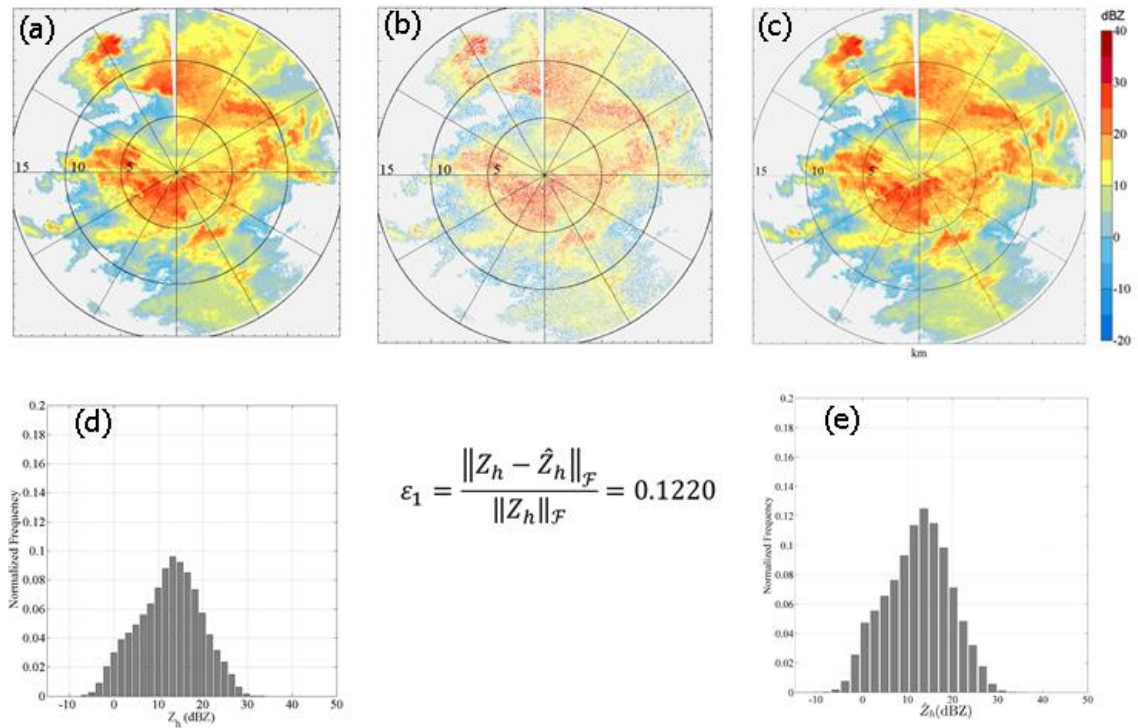
Figure 12. Illustration of reconstruction of precipitation echo using matrix completion by sampling directly from the original matrix. (a) Original Z_h data matrix in polar coordinates (b) $P_\Omega(Z_h)$:Randomly sub-sampled entries of the low-rank Z_h matrix. (c) $\hat{Z}_h$: Recovered Z_h using nearest neighbor interpolation (d) Distribution of Z_h data (e) Distribution of $\hat{Z}_h$ data.

The weather radar data matrix completion should not be treated as an image interpolation problem. The data matrix is not an image and matrix entries do not denote pixel values. Further, the matrix entries are subsequently used for computing science products such as rainfall. Therefore, the objective here is not to render a visibly similar image. The image interpolation usually interpolates first in one direction separately and then in the second direction. To compare the image interpolation with our method, in Figure 12 we interpolate the sparsely sampled weather data using the nearest neighbor method. The reconstructed matrix has a higher error, but more importantly the resultant matrix looks like a "smoothed" version of the original matrix and shows interpolation artifacts. This is not same as recovering the matrix accurately.

In this example, we used the simplest method of nearest-neighbor interpolation. There are other advanced image interpolation algorithms such as those based on bilinear functions and cubic splines which perform better than the nearest-neighbor method. However, all these approaches introduce artifacts the effects of which are compounded while generating the dual-polarimetric products from sparsely sampled precipitation echoes.

Precipitation Downscaling

A related research is downscaling (Ebtehaj et al. 2012) that uses sparse regularization to generate high-resolution images of rainfall products from low-resolution images. The downscaling method uses sparsity of rainfall image in the wavelet domain. Apart from hydrometeorological applications, enhancing the resolution and quality of low-resolution images, often referred to as super-resolution in the image processing community, has been a subject of interest for many years. Super-resolution refers to recovering a high-resolution signal form its low-resolution counterparts.

Downscaling is related to compressed sensing research but differs considerably from sparse sensing of precipitation. Firstly, downscaling is applied on an *image* rather

than the data matrix. Secondly, the sparsity on downscaling is available for the rainfall products rather than the received signal itself. Finally, the downscaling is an offline processing method while the problem we consider is real-time sensing and acquisition of precipitation echoes.

CHAPTER 5

AN OPERATIONAL CS-BASED WEATHER RADAR

In general, the weather signal as received by the radar is contaminated with a number of unwanted echoes or interferences. These interferences may cause the weather signal matrix to lose its low rank nature. Therefore, any compressed sensing approach for weather radar must account for such situations. In this chapter, we analyze the modifications in the reconstruction to account for such situations.

Reconstruction In Noise

The ability of a weather radar to detect weak echoes is limited by the presence of noise or unwanted echoes. Some of these unwanted signals originate externally to the radar system, such as cosmic noise, radome reflections, interference from co-located radars, and power transmission lines. The internal source of noise in microwave radar receiver is mainly thermal. The thermal noise from various microwave devices in the radar receiver tends to lower the signal-to-noise ratio, thereby masking the weaker signals. Apart from the receiver noise, other external interference may also be encountered in weather signal (for example, from a co-located aircraft surveillance radar). Therefore, the performance of CS should also be characterized for precipitation signals in the presence of noise.

The illustrations in Chapter 4 operated on noise-free thresholded data. In this study, we characterize the performance of a CS-based weather radar in the presence of additive noise. We use a signal model where the precipitation signals form a low-rank matrix that is corrupted with (bounded) noise. Using recent advances in algorithms for matrix completion from few noisy observations (Candès and Plan 2010), we can reconstruct the precipitation scene with reasonable accuracy. The theoretical support for this application comes from the extension of matrix completion algorithms proven stable

in the presence of bounded noise (Candès and Plan 2010). As a first step we change the nuclear norm minimization problem in (42) as follows:

$$\text{minimize } \|X\|_*$$

$$\text{subject to } \|P_\Omega(X - Y)\|_{\mathcal{F}} \leq \delta$$

(43)

where Y is the true matrix M contaminated with noise matrix N, and δ is the bounded noise. The SVT algorithms allows for the recovery of matrix using this formulation. We illustrate this reconstruction in Figure 13.
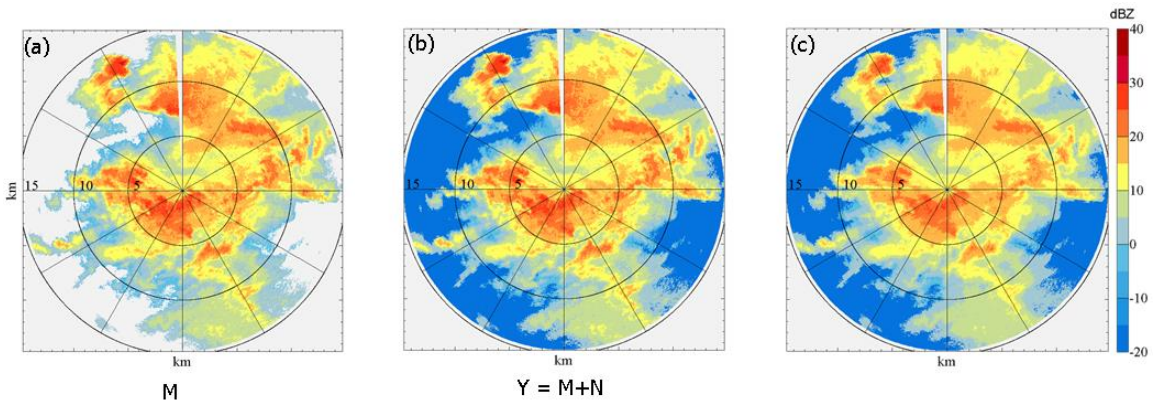
Figure 13. Illustration of reconstruction in noise using SVT algorithm. (a) The noise thresholded matrix M. (b) The measured matrix Y contaminated with noise N. (c) Reconstructed matrix from the sparse observations (same as in Figure 10). We assumed Signal-to-Noise ratio (SNR) of 70 dB.

Recovery In Presence Of Clutter

Apart from the precipitation, the transmitted signal of the weather radar can hit other targets as well. The backscatter from stationary targets on ground such as trees and buildings constitutes undesired signals or clutter for the weather radar. Since the radar gains valuable precipitation data close to the ground, it is difficult to avoid ground clutter. Filtering the ground clutter echoes from the received signal, called clutter filtering, is one of the critical tasks of the radar signal processor. Since the ground clutter is largely

stationary and therefore has close-to-zero Doppler velocity, it resides in the low frequency part of the signal spectrum. For hard target targets, the ground clutter can be easily removed by passing the received signal through a filter that has a notch at zero frequency. The targets-of-interest are moving and therefore reside in the non-zero frequencies. This filtering technique therefore preserves the target signal. However, for weather radar, this technique would prove disastrous since the precipitation signal co-occupies the low-frequency part of the spectrum with the ground clutter.

Modern weather radars thus adopt sophisticated ground clutter filtering techniques that use the Gaussian shape of the precipitation spectrum (Siggia and Passarelli Jr 2004). In case of compressed sensing weather radar, these filtering techniques do not directly apply. This calls for an innovative clutter filtering technology for compressed sensing weather radar.

We note that, except for the lowest elevation scan, most of the time ground clutter manifests as a spatially sparse signal. This allows us to pose the clutter filtering as a problem of decomposing observed weather data matrix into the sum of a low-rank matrix and a sparse error matrix (Candès et al. 2011): the precipitation corresponds to the low-rank matrix and the clutter corresponds to the sparse error. Figure 14(a) shows XPOL-5 radar data collected at Eastern Iowa Airport at Cedar Rapids on May 25, 2013. The radar captured a passing storm apart from ground clutter from nearby buildings and vehicles. However, this data matrix can be represented as a sum of low-rank weather data matrix (Figure 14(b)) and sparse ground clutter (Figure 14(c)).

$$\underset{L,S}{\text{minimize}} \|L\|_* + \lambda \|S\|_1$$

$$\text{subject to } L_{ij} + S_{ij} = M_{ij}, (i,j) \in \Omega \tag{44}$$

Since weather radars also scan close to ground, the ground/urban clutter contamination is one of the most frequently observed unwanted signals in weather echoes. The ground clutter does not form a low-rank matrix. However, often ground

clutter can be viewed as a sparsely distributed error. This assumption allows for development of CS-based efficient clutter filtering algorithms using recent research on the reconstruction of partially observed low-rank matrices mixed with sparse (impulse) noise (Candès et al. 2011).
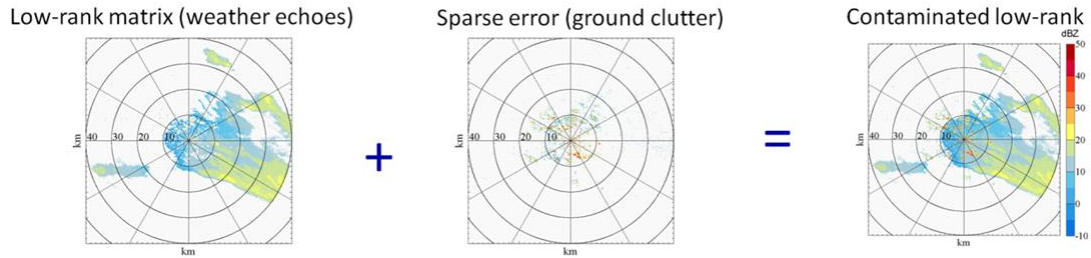
Figure 14. Ground clutter is sparse and the weather signal is low-rank. The addition of two is a corrupted low-rank matrix. XPOL-5 data as observed on 25 May, 2013.

Compressed Dual-polarimetry

Many modern weather radars are polarization agile. That is, they can transmit both horizontal and vertical polarized electromagnetic waves independently, and the radar receiver/processor processes the two polarization echoes independently. From such measurements, the determination of dual-polarized products such as differential reflectivity (Z_{dr}), copolar correlation coefficient (ρ_{hv}) and differential propagation phase (ϕ_{dp}) follows. Proper interpretation of these products provides estimates on the size, shape, and type of hydrometeors.

Here we extend the sparse sensing to dual-polarization estimates of precipitation. We use data collected with the Iowa X-band Polarimetric (XPOL) radars to test and demonstrate our techniques. Application of CS requires *sparsity* or sparse approximation for the radar signals. Unlike hard point targets, precipitation echoes are not sparse in conventional dictionaries such as time and frequency. However, the motion among the

precipitation scatterers is small compared to the radar wavelength. With typical sampling rates their relative positions produce highly correlated echoes from sample to sample. These highly-correlated precipitation echoes can be modeled as a low-rank matrix. We reconstruct the full matrix and produce estimates of the dual-polarization products in Figure 15 where we see that the error in the dual-pol estimates rises compared to single-pol estimates. Therefore, one of the future directions will be to further reduce the errors in the single-pol estimates.

$$\varepsilon_1 = \frac{\|Z_{dr} - \hat{Z}_{dr}\|_{\mathcal{F}}}{\|Z_{dr}\|_{\mathcal{F}}} = 0.0991 \qquad \varepsilon_1 = \frac{\|\Psi_{dp} - \hat{\Psi}_{dp}\|_{\mathcal{F}}}{\|\Psi_{dp}\|_{\mathcal{F}}} = 0.1130$$
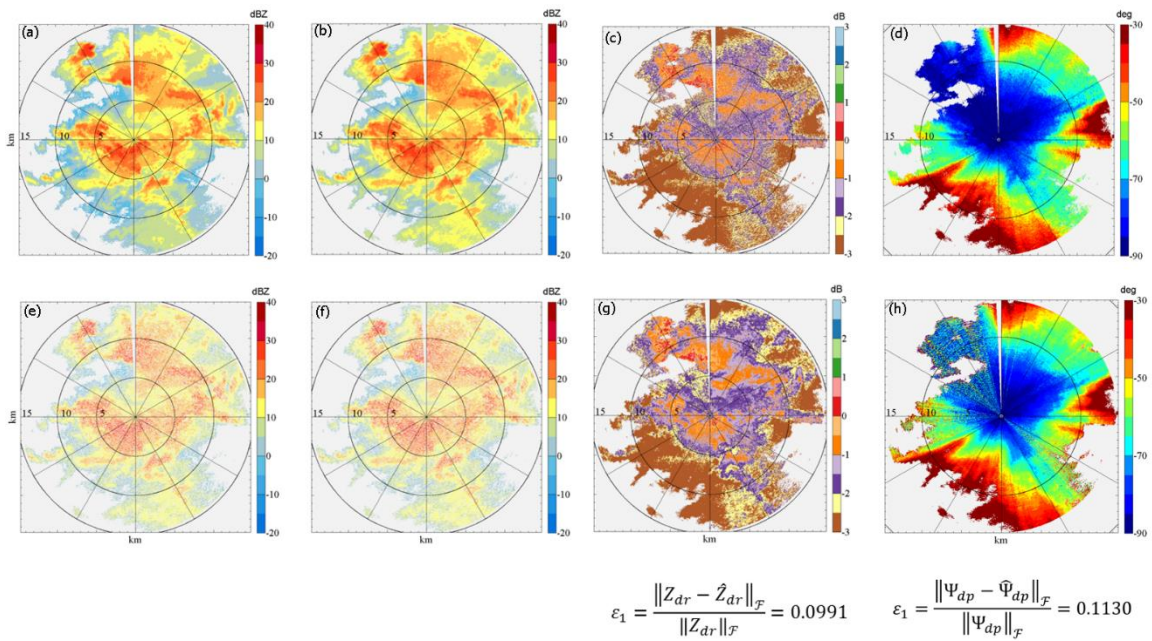
Figure 15. Illustration of reconstruction of dual-pol estimates. (a) Measured Z_h (b) Measured Z_v (c) Measured differential reflectivity Z_{dr} (d) Measured Ψ_{dp} (e) $P_\Omega(Z_h)$: sparsely sampled Z_h (f) $P_\Omega(Z_V)$: sparsely sampled Z_V (g) $\hat{Z}_{dr}$: Reconstructed differential reflectivity (h) $\hat{\Psi}_{dp}$: Reconstructed differential phase.

CHAPTER 6

SPECTRAL SUPER-RESOLUTION WITH PRIOR KNOWLEDGE

Some of the initial thrusts in this research were based on finding suitable sparsity models in conventional dictionaries for the weather radar. As explained in Chapter 3, this approach didn't yield an efficient way to sparsely sample the precipitation echoes. However, our investigation in the conventional sparsity models yielded a new research thrust in spectral super-resolution. The spectrum of the precipitation echo has a Gaussian power spectral density in a continuously-valued frequency domain. Existing compressed sensing recovery techniques do not allow for recovery of such a spectrum from undersampled signals. During our problem formulation of the recovery of this spectrum from few samples, we found novel results in spectral super-resolution that we present in this chapter.

Spectral Estimation

In many areas of engineering, it is desired to infer the spectral contents of a measured signal. In the absence of any *a priori* knowledge of the underlying statistics or structure of the signal, the choice of spectral estimation technique is a subjective craft (Marple Jr. 1987; Stoica and Moses 2005). However, in several applications, the knowledge of signal characteristics is available through previous measurements or prior research. By including such prior knowledge during spectrum estimation process, it is possible to enhance the performance of spectral analysis.

One useful signal attribute is its sparsity in spectral domain. In recent years, spectral estimation methods that harness the spectral sparsity of signals have attracted considerable interest (Mishali and Eldar 2010; Duarte and Baraniuk 2013; Tang et al. 2013b; Candès and Fernandez-Granda 2013). These methods trace their origins to compressed sensing (CS) that allows accurate recovery of signals sampled at sub-Nyquist rate (Donoho 2006b). In the particular context of spectral estimation, the signal is

assumed to be sparse in a finite discrete dictionary such as Discrete Fourier Transform (DFT). As long as the true signal frequency lies in the center of a DFT bin, the discretization in frequency domain faithfully represents the continuous reality of the true measurement. If the true frequency is not located on this discrete frequency grid, then the aforementioned assumption of sparsity in the DFT domain is no longer valid (Tan and Nehorai 2014) (Huang et al. 2012). The result is an approximation error in spectral estimation often referred to as scalloping loss (Harris 1978), basis mismatch (Chi et al. 2011), and gridding error (Fannjiang and Liao 2012).

Recent state-of-the-art research (Candès and Fernandez-Granda 2013; Tang et al. 2013a; Tang et al. 2013b) has addressed the problem of basis mismatch by proposing compressed sensing in continuous spectral domain. This *grid-free* approach is inspired by the problems of total variation minimization (Candès and Fernandez-Granda 2013) and atomic norm minimization (Tang et al. 2013b) to recover *super-resolution* frequencies - lying anywhere in the continuous domain [0,1] - with few random time samples of the spectrally sparse signal, provided the line spectrum maintains a nominal separation. A number of generalizations of off-the-grid compressed sensing for specific signal scenarios have also been attempted, including extension to higher dimensions (Chi and Chen 2013; Chi et al. 2011; Xu et al. 2014; Yang and Xie 2014).

However, these formulations of off-the-grid compressed sensing assume no prior knowledge of signal other than sparsity in spectrum. In fact, in many applications, where signal frequencies lie in continuous domain such as radar (Skolnik 2008a), acoustics (Trivett and Robinson 1981), communications (Beygi and Mitra 2014), and power systems (Zygarlicki and Mroczka 2012), additional prior information of signal spectrum might be available. For example, a radar engineer might know the characteristic speed with which a fighter aircraft flies. This knowledge then places the engineer in a position to point out the ballpark location of the echo from the aircraft in the Doppler frequency spectrum. Similarly, in a precipitation radar, the spectrum widths of echoes from certain

weather phenomena (tornadoes or severe storms) are known from previous observations (Doviak and Zrnić 1993). This raises the question whether we can use signal structures beyond sparsity to improve the performance of spectrum estimation.

There are extensive works in compressed sensing literature that discuss recovering sparse signals using secondary signal support structures, such as *structured sparsity* (Cevher et al. 2009) (tree-sparsity (Baraniuk et al. 2010), block sparsity (Stojnic et al. 2009), and Ising models (Cevher et al. 2008)), spike trains (Hegde et al. 2009; Azais et al. 2013), nonuniform sparsity (Khajehnejad et al. 2009; Vaswani and Lu 2010), and multiple measurement vectors (MMVs) (Duarte and Eldar 2011). However, these approaches assume discrete-valued signal parameters while, in the spectrum estimation problem, frequencies are continuous-valued. Therefore, the techniques of using prior support information in discrete compressed sensing for structured sparsity do not directly extend to spectrum estimation. Moreover, it is rather unclear as to how general signal structure constraints can be imposed for super-resolution recovery of continuous-valued frequency components.

Here, we focus on a more generalized approach to super-resolution that addresses the foregoing problems with line spectrum estimation. We propose continuous-valued line spectrum estimation of irregularly undersampled signal in the presence of structured sparsity. Prior information about the signal spectrum comes in various forms. For example, in the spectral information concerning a rotating mechanical system, the frequencies of the supply lines or interfering harmonics might be precisely known (Wirfält et al. 2011). However, in a communication problem, the engineer might only know the frequency band in which a signal frequency is expected to show up. Often the prior knowledge is not even specific to the level of knowing the frequency subbands precisely. The availability of previous measurements, such as in remote sensing or bio-medicine, can aid in knowing the likelihood of having an active signal frequency in the neighborhood of a specific spectral band. In this paper, we greatly broaden the scope of

prior information that can range from knowing only the likelihood of occurrence of frequency components in a spectral subband to exactly knowing the location of some of the frequencies.

In all these cases, we propose a precise semidefinite program to perfectly recover all the frequency components. When some frequencies are *precisely* known, we propose to use *conditional atomic norm* minimization to recover the off-the-grid frequencies. In practice, the frequencies are seldom *precisely* known. However, as long as the frequency locations are approximately known to the user, we show that the spectrally sparse signal could still be perfectly reconstructed. Here, we introduce *constrained atomic norm* minimization that accepts the *block priors* - frequency subbands in which true spectral contents of the signal are known to exist - in its semidefinite formulation. When only the probability density function of signal frequencies is known, we incorporate such a *probabilistic prior* in the spectral estimation problem by suggesting the minimization of *weighted atomic norm*. The key is to transform the dual of atomic norm minimization to a semidefinite program using linear matrix inequalities (LMI). These linear matrix inequalities are, in turn, provided by theories of positive trigonometric polynomials (Fejér 1915). Our methods boost the signal recovery by admitting lesser number of samples for spectral estimation and decreasing reliance on the minimum resolution necessary for super-resolution. If the prior information locates the frequencies within very close boundaries of their true values, then we show that it is possible to perfectly recover the signal using samples no more than thrice the number of signal frequencies.

Our work has close connections with a rich heritage of research in spectral estimation. For uniformly sampled or *regularly spaced* signals, there are a number of existing approaches for spectral estimation by including known signal characteristics in the estimation process. The classical Prony's method can be easily modified to account for known frequencies (Trivett and Robinson 1981). Variants of the subspace-based frequency estimation methods such as MUSIC (MUltiple SIgnal Classification) and

ESPRIT (Estimation of Signal Parameters via Rotation Invariance Techniques) have also been formulated (Linebarger et al. 1995; Wirfält et al. 2011), where prior knowledge can be incorporated for parameter estimation. For applications wherein only approximate knowledge of the frequencies is available, the spectral estimation described in (Zachariah et al. 2013) applies circular von Mises probability distribution on the spectrum.

For *irregularly spaced* or non-uniformly sampled signal, sparse signal recovery methods which leverage on prior information have recently gained attention (Khajehnejad et al. 2009; Vaswani and Lu 2010; Ji et al. 2008; Bourguignon et al. 2007). Compressed sensing with clustered priors was addressed in (Yu et al. 2012a) where the prior information on the number of clusters and the size of each cluster was assumed to be unknown. In (Fannjiang 2011), MUSIC was extended to undersampled, irregularly spaced sparse signals in a discrete dictionary, while (Liao and Fannjiang 2014) analyzed the performance of *snapshot*-MUSIC for uniformly sampled signals in a continuous dictionary. Our technique is more general; it applies to irregularly sampled signals in a continuous dictionary, and is, therefore, different from known works on utilizing prior information for spectral estimation of regularly sampled signals.

Problem Formulation

In general, the prior information can be available for any of the signal parameters such as amplitude, phase or frequencies. However, in this paper, we restrict the available knowledge to only the frequencies of the signal. We assume that the amplitude and phase information of any of the spectral component is not known, irrespective of the pattern of known frequency information. Our approach is to first analyze the case of a more nebulous prior information, which is the probabilistic priors, followed by an interesting special case of block priors. The case when *some* frequencies are precisely known is considered in the end where, unlike previously considered cases, we recover the signal using the semidefinite program for the primal problem.

We consider a frequency-sparse signal $x[l]$ expressed as a sum of s complex exponentials,

$$x[l] = \sum_{j=1}^{s} c_j e^{i2\pi f_j l} = \sum_{j=1}^{s} |c_j| a(f_j, \phi_j)[l], \qquad l \in \mathcal{N}, \tag{45}$$

where $c_j = |c_j| e^{i\phi_j}$ $(i = \sqrt{-1})$ represents the complex coefficient of the frequency $f_j \in [0, 1]$, with amplitude $|c_j| > 0$, phase $\phi_j \in [0, 2\pi)$, and frequency-*atom* $a(f_j, \phi_j)[l] = e^{(i2\pi f_j l + \phi_j)}$. We use the index set $\mathcal{N} = \{l \mid 0 \leq l \leq n - 1\}$, where $|\mathcal{N}| = n, n \in \mathbb{N}$, to represent the time samples of the signal. We further suppose that the signal in (45) is observed on the index set $\mathcal{M} \subseteq \mathcal{N}$, $|\mathcal{M}| = m \leq n$ where m observations are chosen uniformly at random. Our objective is to recover all the continuous-valued the frequencies with very high accuracy using this undersampled signal.

The signal in (45) can be modeled as a positive linear combination of the unit-norm frequency-*atoms* $a(f_j, \phi_j)[l] \in \mathcal{A} \subset \mathbb{C}^n$ where $\mathcal{A}$ is the set of all the frequency-atoms. These frequency atoms are basic units for synthesizing the frequency-sparse signal. This leads to the following formulation of the *atomic norm* $\|\hat{x}\|_{\mathcal{A}}$ - a sparsity-enforcing analog of ℓ_1 norm for a general atomic set $\mathcal{A}$:

$$\|\hat{x}\|_{\mathcal{A}} = \inf_{c_j, f_j} \left\{ \sum_{j=1}^{s} |c_j| : \hat{x}[l] = \sum_{j=1}^{s} c_j e^{i2\pi f_j l}, l \in \mathcal{M} \right\}. \tag{46}$$

To estimate the remaining $\mathcal{N} \backslash \mathcal{M}$ samples of the signal x, (Chandrasekaran et al. 2012) suggests minimizing the atomic norm $\|\hat{x}\|_{\mathcal{A}}$ among all vectors $\hat{x}$ leading to the same observed samples as x. Intuitively, the atomic norm minimization is similar to ℓ_1-minimization being the tightest convex relaxation of the combinatorial ℓ_0-minimization problem. The *primal* convex optimization problem for atomic norm minimization can be formulated as follows,

$$\underset{\hat{x}}{\text{minimize}} \|\hat{x}\|_{\mathcal{A}} \tag{47}$$

$$\text{subject to } \hat{x}[l] = x[l], \qquad l \in \mathcal{M}$$

Equivalently, the off-the-grid compressed sensing (Tang et al. 2013b) suggests the following semidefinite characterization for $\|\hat{x}\|_{\mathcal{A}}$:

Definition 1. *(Tang et al. 2013b) Let T_n denote the $n \times n$ positive semidefinite Toeplitz matrix, $t \in \mathbb{R}^+$, $tr(\cdot)$ denote the trace operator and $(\cdot)^*$ denote the complex conjugate. Then,*

$$\|\hat{x}\|_{\mathcal{A}} = \inf_{T_n,t} \left\{ \frac{1}{2|\mathcal{N}|} tr(T_n) + \frac{1}{2}t : \begin{bmatrix} T_n & \hat{x} \\ \hat{x}^* & t \end{bmatrix} \succcurlyeq 0 \right\}. \tag{48}$$

The positive semidefinite Toeplitz matrix T_n is related to the frequency atoms through the following Vandermonde decomposition result by Carathèodory (Carathèodory 1911):

$$T_n = URU^*, \tag{49}$$

where

$$U_{lj} = a(f_j, \phi_j)[l], \tag{50}$$

$$R = diag([b_1, \cdots, b_r]). \tag{51}$$

The diagonal elements of R are real and positive, and $r = rank(T_n)$.

Consistent with this definition, the atomic norm minimization problem for the frequency-sparse signal recovery can now be formulated as a semidefinite program (SDP) with m affine equality constraints:

$$\underset{T_n,\hat{x},t}{\text{minimize}} \frac{1}{2|\mathcal{N}|} tr(T_n) + \frac{1}{2}t$$

$$\text{subject to } \begin{bmatrix} T_n & \hat{x} \\ \hat{x}^* & t \end{bmatrix} \succcurlyeq 0 \tag{52}$$

$$\hat{x}[l] = x[l], \qquad l \in \mathcal{M}.$$

When some information about the signal frequencies is known *a priori*, then our goal is to find a signal vector $\hat{x}$ in (52) whose frequencies satisfy additional constraints imposed

by prior information. In other words, if $\mathcal{C}$ denotes the set of constraints arising due to prior knowledge of frequencies, then our goal is to find the infimum in (46) over $f_j \in \mathcal{C}$.

While framing the problem to harness the prior information, a common approach in compressed sensing algorithms is to replace the classical minimization program with its weighted counterpart (Khajehnejad et al. 2009; Vaswani and Lu 2010). However, signals with continuous-valued frequencies do not lead to a direct application of the weighted ℓ_1 approach. Rather, such an application leads to a fundamental conundrum: the Vandermonde decomposition of positive semidefinite Toeplitz matrices works for general frequencies wherein the frequency atom in (50) can freely take any frequency and phase values, and it is not clear how to further tighten the positive semidefinite Toeplitz structure to incorporate the known prior information. Thus, it is non-trivial to formulate a computable convex program that can incorporate general prior information to improve signal recovery.

<div align="center">Probabilistic Priors</div>

In the probabilistic prior model, the probability density function of the frequencies is known. Let F be the random variable that describes the signal frequencies. Let the probability density function (pdf) of F be $p_F(f)$. The problem of line spectrum estimation deals with a finite number of signal frequencies in the domain $[0,1]$. For example, we can assume $p_F(f)$ to be piecewise constant as follows. Let the domain $[0,1]$ consist of p disjoint subbands such that $[0,1] = \cup_{k=1}^{p} \mathcal{B}_k$ where $\mathcal{B}_k$ denotes a subband or a subset of $[0,1]$. Then the restriction $p_F(f)|_{\mathcal{B}_k}$ of $p_F(f)$ to $\mathcal{B}_k$ is a constant. Figure 16 illustrates a simple case for $p = 2$, where the line spectrum $X(f)$ of a signal x is non-uniformly sparse over two frequency subbands $\mathcal{B}_1$ and $\mathcal{B}_2 = [0,1]\backslash\mathcal{B}_1$, such that the frequencies $f_j, j = 1, \cdots, s$, occur in the subinterval $\mathcal{B}_2$ more likely than in $\mathcal{B}_1$.
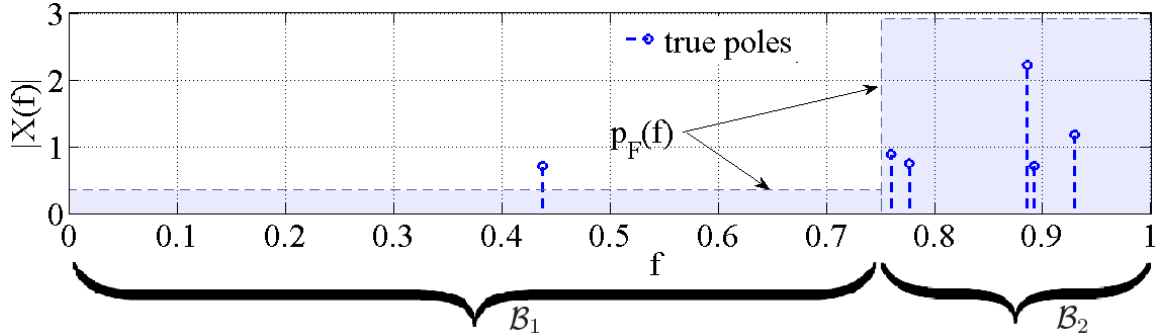
Figure 16. The probability density function $p_F(f)$ of the frequencies shown with the location of true frequencies in the spectrum $X(f)$ of the signal $x[l]$.

Intuitively, given probabilistic priors, one may think of recovering the signal x by minimizing a *weighted atomic norm* given by:

$$\|\hat{x}\|_{w\mathcal{A}} = \tag{53}$$
$$\inf_{c_j, f_j}\left\{\sum_{j=1}^{s} w_j |c_j| : \hat{x}[l] = \sum_{j=1}^{s} c_j e^{i2\pi f_j l}, l \in \mathcal{M}\right\},$$

where $\boldsymbol{w} = \{w_1, \cdots, w_s\}$ is the weight vector, each element w_j of which is associated with the probability of occurrence of the corresponding signal frequency f_j. The weight vectors are assigned using a *weight function* $w(f)$. The $w(f)$ is a piecewise constant function in the domain $[0,1]$ such that the restriction $w(f)|_{\mathcal{B}_k}$ of $w(f)$ to $\mathcal{B}_k$ is a constant. Therefore, $\forall \{f_1, \cdots, f_j\} \in \mathcal{B}_k$, we have $w_1 = \cdots = w_j = w(f)|_{f \in \mathcal{B}_k} = w(f_{\mathcal{B}_k})$ (say). The $w(f)$ is a decreasing function of the sparsity associated with the corresponding frequency subband so that the subband with higher (lower) value of pdf or lesser (more) sparsity is weighted lightly (heavily).

The problem of line spectral estimation using probabilistic prior can now be presented as the (primal) optimization problem concerning the weighted atomic norm:

$$\underset{\hat{x}}{\text{minimize}} \|\hat{x}\|_{w\mathcal{A}}$$
$$\text{subject to } \hat{x}[l] = x[l], \qquad l \in \mathcal{M} \tag{54}$$

But we now observe that, unlike weighted ℓ_1 norm (Khajehnejad et al. 2009), a semidefinite characterization of the weighted atomic norm does not evidently result from (52). Instead, we propose a new semidefinite program for the weighted atomic norm using theories of positive trigonometric polynomials, by looking at its dual problem. For the standard atomic norm minimization problem (47), the dual problem is framed in this manner:

$$\underset{q}{\text{maximize}} \ \langle q_{\mathcal{M}}, x_{\mathcal{M}} \rangle_{\mathbb{R}}$$
$$\text{subject to } \|q\|_{\mathcal{A}}^* \leq 1 \tag{55}$$
$$q_{\mathcal{N} \backslash \mathcal{M}} = 0,$$

where $\|\cdot\|^*$ represents the dual norm. This dual norm is defined as

$$\|q\|_{\mathcal{A}}^* = \sup_{\|\hat{x}\|_{\mathcal{A}} \leq 1} \langle q, \hat{x} \rangle_{\mathbb{R}} = \sup_{f \in [0,1]} |\langle q, a(f, 0) \rangle|. \tag{56}$$

For the weighted atomic norm minimization, the primal problem (54) has only equality constraints. As a result, Slater's condition is satisfied and, therefore, strong duality holds (Boyd and Vandenberghe 2004). In other words, solving the dual problem also yields an exact solution to the primal problem. The dual of weighted atomic norm is given by

$$\|q\|_{w\mathcal{A}}^* = \sup_{\|\hat{x}\|_{w\mathcal{A}} \leq 1} \langle q, \hat{x} \rangle_{\mathbb{R}} = \sup_{\phi \in [0,2\pi], f \in [0,1]} \langle q, \frac{1}{w(f)} e^{i\phi} a(f, 0) \rangle_{\mathbb{R}}$$
$$= \sup_{f \in [0,1]} \left| \langle q, \frac{1}{w(f)} a(f, 0) \rangle \right|. \tag{57}$$

The dual problem to (54) can be stated hence,

$$\underset{q}{\text{maximize}} \ \langle q_{\mathcal{M}}, x_{\mathcal{M}} \rangle_{\mathbb{R}}$$
$$\text{subject to } \|q\|_{w\mathcal{A}}^* \leq 1 \tag{58}$$
$$q_{\mathcal{N} \backslash \mathcal{M}} = 0,$$

which by substitution of (57) becomes,

$$\underset{q}{\text{maximize}} \ \langle q_{\mathcal{M}}, x_{\mathcal{M}} \rangle_{\mathbb{R}} \tag{59}$$

$$\text{subject to } \sup_{f\epsilon[0,1]} \left|\langle q, \frac{1}{w(f)} a(f,0)\rangle\right| \le 1$$

$$q_{\mathcal{N}\backslash\mathcal{M}} = 0.$$

Let the probabilistic priors consist of distinct weights for p different frequency subbands $\mathcal{B}_k \subset [0,1]$, $k = 1, \cdots, p$, such that $[0,1] = \cup_{k=1}^{p} \mathcal{B}_k = \cup_{k=1}^{p}[f_{L_k}, f_{H_k}]$, where f_{L_k} and f_{H_k} are, respectively, the lower and upper cut-off frequencies for each of the band $\mathcal{B}_k$ (
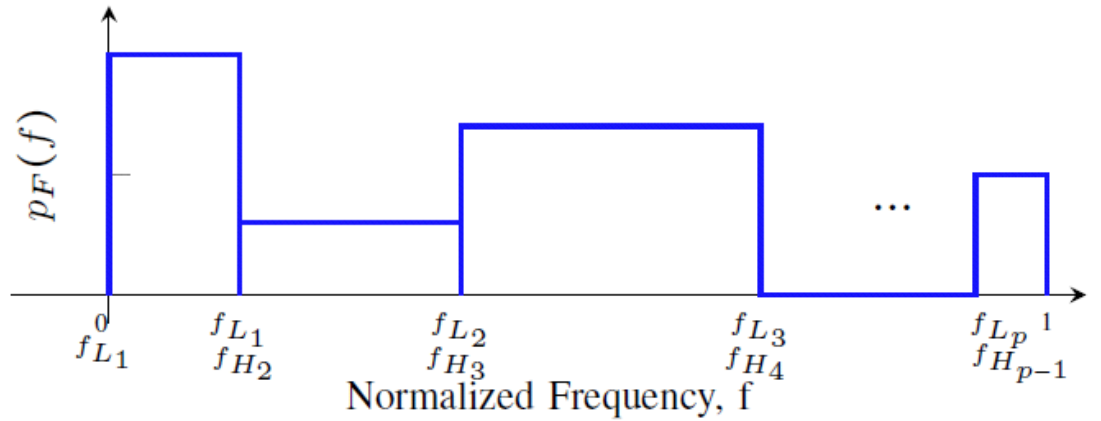
Figure 17). If the probability density function is constant within a frequency band, then the results of the supremums in (59) need not depend on the weight functions, and therefore, the inequality constraint in the dual problem in (59) can be expanded as,

$$\underset{q}{\text{maximize }} \langle q_{\mathcal{M}}, x_{\mathcal{M}}\rangle_{\mathbb{R}}$$

$$\text{subject to } \sup_{f\epsilon\mathcal{B}_1}|\langle q, a(f,0)\rangle| \le w(f_{\mathcal{B}_1})$$

$$\sup_{f\epsilon\mathcal{B}_2}|\langle q, a(f,0)\rangle| \le w(f_{\mathcal{B}_2}) \qquad\qquad (60)$$

$$\vdots$$

$$\sup_{f\epsilon\mathcal{B}_p}|\langle q, a(f,0)\rangle| \le w\left(f_{\mathcal{B}_p}\right)$$

$$q_{\mathcal{N}\setminus\mathcal{M}} = 0.$$

We now map each of the inequality constraints in the foregoing dual problem to a linear matrix inequality, leading to the semidefinite characterization of the weighted atomic norm minimization. The weights are nonnegative values. Further the expression of $Q(f)$ has sine and cosine functions. Therefore, We recognize that the constraints in (60) imply $|1 - Q(f)|^2$ is a positive trigonometric polynomial (Fejér 1915) in $f \in \mathcal{B}_k$, since
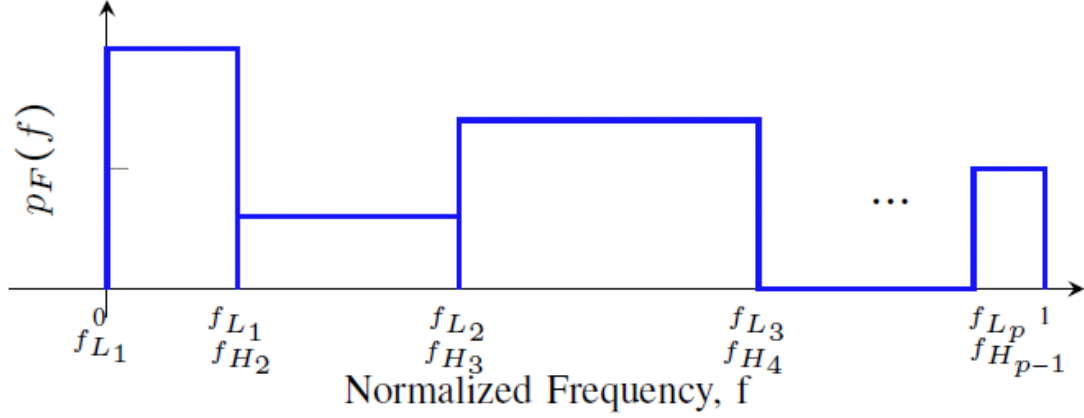
Figure 17. The individual frequencies of spectrally parsimonious signal are assumed to lie in known frequency subbands within the normalized frequency domain $[0, 1]$. We assume that all subbands are non-overlapping so that when $f_{H_{k-1}} = f_{L_k}$, then $\mathcal{B}_{k-1} = \left[f_{L_{k-1}}, f_{H_{k-1}}\right]$ and $\mathcal{B}_k = \left[f_{L_k}, f_{H_k}\right]$.

$$Q(f) = \langle q, a(f, 0) \rangle = \sum_{l=0}^{n-1} q_l e^{-i2\pi fl}. \tag{61}$$

Such a polynomial can be parameterized by a particular type of positive semidefinite matrix. Thus, we can transform the polynomial inequality, such as the ones in (60), to a linear matrix inequality.

Gram Matrix Parametrization

A trigonometric polynomial $R(z) = \sum_{k=-(n-1)}^{n-1} r_k z^{-k}$, which is also nonnegative on the entire unit circle, can be parametrized using a positive semidefinite, Hermitian matrix $\boldsymbol{G}$ (called the *Gram* matrix) that identifies the polynomial coefficients r_k as a function of its elements (Dumitrescu 2007, p. 23):

$$r_k = tr(\boldsymbol{\Theta}_k \boldsymbol{G}), \tag{62}$$

where $\boldsymbol{\Theta}_k$ is an elementary Toeplitz matrix with ones on its kth diagonal and zeros elsewhere. Here, $k = 0$ corresponds to the main diagonal, and k takes positive and negative values for upper and lower diagonals respectively.

For the trigonometric polynomial that is nonnegative only over an arc of the unit circle, we have the following theorem:

Theorem 1. *(Dumitrescu 2007, p. 12) A trigonometric polynomial*

$$R(z) = \sum_{k=-(n-1)}^{n-1} r^k z^{-k}, \ r_{-k} = r_k^*, \tag{63}$$

where $R \in \mathbb{C}_{n-1}[z]$ for which $R(\omega) \geq 0$, for any $z = e^{i\omega}$, $\omega \in [\omega_L, \omega_H] \subset [-\pi, \pi]$, can be expressed as

$$R(z) = F(z)F^*(z^{-1}) + D_{\omega_L \omega_H}(z) \cdot G(z)G^*(z^{-1}), \tag{64}$$

where $F(z)$ and $G(z)$ are causal polynomials with complex coefficients, of degree at most $n - 1$ and $n - 2$, respectively. The polynomial

$$D_{\omega_L \omega_H}(z) = d_1 z^{-1} + d_0 + d_1^* z, \tag{65}$$

where

$$d_0 = -\frac{\alpha\beta + 1}{2} \tag{66}$$

$$d_1 = \frac{1 - \alpha\beta}{4} + j\frac{\alpha + \beta}{4} \tag{67}$$

$$\alpha = tan\frac{\omega_L}{2} \tag{68}$$

$$\beta = tan\frac{\omega_H}{2} \tag{69}$$

is defined such that $D_{\omega_L\omega_H}(\omega)$ is nonnegative for $\omega \in [\omega_L, \omega_H]$ and negative on its complementary.

Since $F(z)$ and $G(z)$ are causal polynomials, the products $F(z)F^*(z^{-1})$, and $G(z)G^*(z^{-1})$ are positive trigonometric polynomials that can each be separately parameterized with Gram matrices $\boldsymbol{G}_1$ and $\boldsymbol{G}_2$ respectively.

Proposition 2. *A trigonometric polynomial R in (63) that is nonnegative on the arc $[\omega_L, \omega_H] \subset [-\pi, \pi]$ or, alternatively, the subband $[f_L, f_H] \subset [0, 1]$, can be parameterized using the Gram matrices $\boldsymbol{G}_1 \in \mathbb{C}^{n\times n}$ and $\boldsymbol{G}_2 \in \mathbb{C}^{(n-1)\times(n-1)}$ as follows:*

$$r_k = tr(\boldsymbol{\Theta}_k \boldsymbol{G_1}) + tr\big((d_1\boldsymbol{\Theta}_{k-1} + d_0\boldsymbol{\Theta}_k + d_1^*\boldsymbol{\Theta}_{k+1}) \cdot \boldsymbol{G_2}\big)$$
$$\triangleq \mathcal{L}_{k,f_L,f_H} tr(\boldsymbol{G_1}, \boldsymbol{G_2}), \tag{70}$$

where we additionally require the elementary Toeplitz matrix $\boldsymbol{\Theta}_k$ in the second argument to be a nilpotent matrix of order $n - k$ for $|k| > 0$. The translation of frequencies between the two domains is given by ($f_L < f_H$):

$$\omega_L = \begin{cases} 2\pi f_L & : 0 \le f_L \le 0.5 \\ 2\pi(f_L - 1) & : 0.5 < f_L < 1 \end{cases} \tag{71}$$

$$\omega_H = \begin{cases} 2\pi f_H & : 0 < f_L \le 0.5 \\ 2\pi(f_H - 1) & : 0.5 < f_H \le 1 \end{cases} \tag{72}$$

The dual polynomial $Q(f)$ in (61) is nonnegative on multiple non-overlapping intervals, and can therefore be parameterized by as many different pairs of Gram matrices $\{\boldsymbol{G}_1, \boldsymbol{G}_2\}$ as the number of subbands p. In the following subsection, we relate this parametrization to the corresponding probabilistic weights of the subbands.

SDP Formulation

Based on the Bounded Real Lemma (Dumitrescu 2007, p. 127) (which, in turn, is based on Theorem 1, a positive trigonometric polynomial constraint of the type $|R(\omega)| \leq 1$ can be expressed as a linear matrix inequality (Dumitrescu 2007, p.143). Stating this result for the dual polynomial constraint over a single frequency band, such as those in (60), we have

$$\lim_{f \in [f_L, f_H]} |\langle q, a(f, 0) \rangle| \leq \gamma, \tag{73}$$

if and only if there exist positive semidefinite *Gram* matrices $G_1 \in \mathbb{C}^{n \times n}$ and $G_2 \in \mathbb{C}^{(n-1) \times (n-1)}$ such that,

$$\gamma^2 \delta_k = \mathcal{L}_{k, \omega_L, \omega_H}(G_1, G_2), \ k \in \mathcal{H},$$

$$\begin{bmatrix} G_1 & q \\ q^* & 1 \end{bmatrix} \succeq 0, \tag{74}$$

where $\mathcal{H}$ is a halfspace, $\delta_0 = 1$, and $\delta_k = 1$ if $k \neq 0$. This linear matrix inequality representation using positive semidefinite matrix G_1 paves way for casting the new dual problem in (60) as a semidefinite program. This above formulation shows that we have changed the inequality form in the convex optimization problem to an equality form allowing semidefinite programming for the weighted atomic norm minimization.

If the cutoff-frequencies ω_L or ω_H (in $[-\pi, \pi]$ domain) are equal to $\pm \pi$, then we can write $[\omega_L, \omega_H] = [\omega'_L + \tau, \omega'_H + \tau]$ such that $[\omega'_L, \omega'_H] \subset [-\pi, \pi]$. For the translated subband $[\omega'_L, \omega'_H]$, let the corresponding subband in the domain $[0,1]$ be $[f'_L, f'_H]$. Then, the LMI formulation given by (70) becomes valid for this subband. However, the polynomial q is now evaluated in the domain $e^{-i\omega}e^{-i\tau}$ instead of $e^{-i\omega}$. The SDP for this frequency translation employs a scaled version of LMI in (74),

$$\delta_k = \mathcal{L}_{k, f'_L, f'_H}(G_1, G_2), \ k \in \mathcal{H}, \tag{75}$$

$$
\begin{bmatrix} G_1 & \frac{1}{\gamma}\tilde{q}_\tau \\ \frac{1}{\gamma}\tilde{q}_\tau^* & 1 \end{bmatrix} \succcurlyeq 0,
$$

where

$$
\tilde{q}_\tau[j] = q[j]e^{-i\tau j}. \tag{76}
$$

We now state the semidefinite program for weighted atomic norm minimization with the probabilistic priors. We use the LMI representation for each of the inequality constraints in (60) as follows:

$$
\begin{aligned}
&\underset{\substack{q \\ G_{11}, G_{12}, \cdots, G_{1p}, \\ G_{21}, G_{22}, \cdots, G_{2p}}}{\text{maximize}} \ \langle q_{\mathcal{M}}, x_{\mathcal{M}} \rangle_{\mathbb{R}} \\[1em]
&\text{subject to } q_{\mathcal{N}\backslash\mathcal{M}} = 0
\end{aligned}
$$

$$
\delta_{k_1} = \mathcal{L}_{k_1, f'_{L_1}, f'_{H_1}}(G_{11}, G_{21}), \qquad k_1 = 0, \cdots, n-1
$$

$$
\begin{bmatrix} G_{11} & \frac{1}{w_1}\tilde{q}_{\tau_1} \\ \frac{1}{w_1}\tilde{q}_{\tau_1}^* & 1 \end{bmatrix} \succcurlyeq 0,
$$

$$
\delta_{k_2} = \mathcal{L}_{k_2, f'_{L_2}, f'_{H_2}}(G_{12}, G_{22}), \qquad k_2 = 0, \cdots, n-1 \tag{77}
$$

$$
\begin{bmatrix} G_{12} & \frac{1}{w_2}\tilde{q}_{\tau_2} \\ \frac{1}{w_2}\tilde{q}_{\tau_2}^* & 1 \end{bmatrix} \succcurlyeq 0,
$$

$$
\vdots
$$

$$
\delta_{k_p} = \mathcal{L}_{k_p, f'_{L_p}, f'_{H_p}}(G_{1p}, G_{2p}), \qquad k_p = 0, \cdots, n-1
$$

$$
\begin{bmatrix} G_{1p} & \frac{1}{w_p}\tilde{q}_{\tau_p} \\ \frac{1}{w_p}\tilde{q}_{\tau_p}^* & 1 \end{bmatrix} \succcurlyeq 0,
$$

$$\text{where } \tilde{q}_{\tau_k}[j] = q[j]e^{-i\tau_k j}, \quad k = 1, \cdots, p$$

$$\boldsymbol{G}_{11}, \boldsymbol{G}_{12}, \cdots, \boldsymbol{G}_{1p} \in \mathbb{C}^{n \times n},$$

$$\text{and } \boldsymbol{G}_{21}, \boldsymbol{G}_{22}, \cdots, \boldsymbol{G}_{2p} \in \mathbb{C}^{(n-1) \times (n-1)}.$$

The unknown frequencies in $\hat{x}$ can be identified by the frequency localization approach (Tang et al. 2013b) based on computing the dual polynomial, that we state for the weighted atomic norm problem in Algorithm 1. We state that this characterization of the spectral estimation is a general way to integrate given knowledge about the spectrum. If the engineer is able to locate the signal frequency in a particular subband with a very high degree of certainty, better results can be obtained using the optimization (77). Also, information about signal frequency bands is frequently available through previous research and measurements, especially in problems pertaining to communication, power systems and remote sensing. We consider this more practical case in the following section.

Algorithm 1. Frequency Localization for probabilistic priors

1: Solve the dual problem (77) to obtain the optimum solution $q^{\star}$.

2: Let $\mathcal{F} = \{f_1, \cdots, f_j, \cdots, f_s\}$ be the unknown frequencies of signal x. The unknown frequencies f_j, identify as $\left| \langle q^{\star}, a(f_j, 0) \rangle \right| = w_k$, where $f_j \in \mathcal{B}_k \subset [0,1]$. For $f \in (\mathcal{B}_k \backslash \mathcal{F}) \subset [0,1]$, $|\langle q^{\star}, a(f, 0) \rangle| < w_k$.

3: The corresponding complex coefficients can be recovered by solving a system of simultaneous linear equations $\hat{x}[l] - \sum_{j=1}^{s} c_j a(f_j, 0)[l] = 0$.

Block Priors

Of particular interest to spectral estimation are spectrally block sparse signals where certain frequency bands are known to contain all the spectral contents of the signal. Let us assume that all the s frequencies f_j of the spectrally sparse signal x are

known *a priori* to lie only in a finite number of non-overlapping frequency bands or intervals within the normalized frequency domain [0,1]. Here, the known set $\mathcal{C}$ is defined as the set $\mathcal{B}$ of all frequency bands in which signal frequencies are known to reside. The prior information consists of the precise locations of all the frequency bands - the lower and upper cut-off frequencies $f_{\mathcal{L}_k}$ and f_{H_k} respectively for each of the band $\mathcal{B}_k$ - as shown in the Figure 18. We, therefore, have $f_j \in \mathcal{B}$, $\mathcal{B} = \bigcup_{k=1}^{p} \mathcal{B}_k = \bigcup_{k=1}^{p} [f_{L_k}, f_{H_k}]$, where p is the total number of disjoint bands known *a priori*.
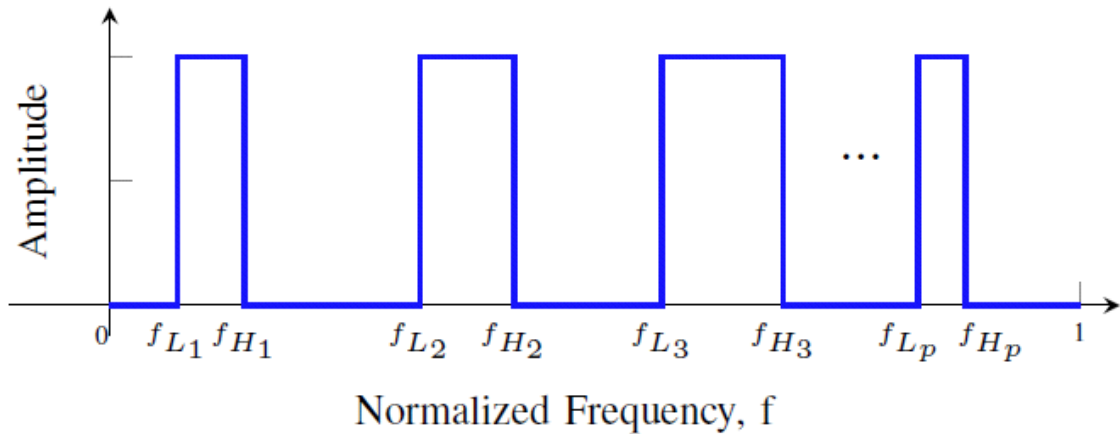
Figure 18. The individual frequencies of spectrally sparse signal are assumed to lie in known non-overlapping frequency subbands within the normalized frequency domain [0, 1].

This *block prior* problem could easily be considered as a special case of probabilistic priors where the probability of a frequency occurring in known subbands is unity while it is zero for all other subbands. When the frequencies are known to reside in the set of subbands $\mathcal{B}$ *a priori*, we propose to minimize a *constrained* atomic norm $\|\hat{x}\|_{\mathcal{A},\mathcal{B}}$ for perfect recovery of the signal:

$$\|\hat{x}\|_{\mathcal{A},\mathcal{B}} = \inf_{c_j, f_j \in \mathcal{B}} \left\{ \sum_{j=1}^{s} |c_j| : \hat{x}[l] = \sum_{j=1}^{s} c_j e^{i2\pi f_j l}, l \in \mathcal{M} \right\}, \tag{78}$$

As noted earlier, to recover all of the off-the-grid frequencies of the signal x given the block priors, the direct extension of a semidefinite program from (52) to minimize the constrained atomic norm is non-trivial. We address this problem by working with the dual problem of the constrained atomic norm minimization, and then transforming the dual problem to an equivalent semidefinite program by using theories of positive trigonometric polynomials. We note that in the case of block priors, (56) can be written as $\|q\|_{\mathcal{A},\mathcal{B}}^* = \sup_{f \in \mathcal{B}} |\langle q, a(f,0) \rangle| = \sup_{f \in \mathcal{B}} |Q(f)|$, where $Q(f)$ is the dual polynomial. The primal problem of constrained atomic norm minimization is given by

$$\underset{\hat{x}}{\text{minimize}} \|\hat{x}\|_{\mathcal{A},\mathcal{B}}$$
$$\text{subject to } \hat{x}[l] = x[l], \qquad l \in \mathcal{M} \tag{79}$$

and, similar to (55), we can formulate the corresponding dual problem as

$$\underset{q}{\text{maximize}} \langle q_{\mathcal{M}}, x_{\mathcal{M}} \rangle_{\mathbb{R}}$$
$$\text{subject to } \|q\|_{\mathcal{A},\mathcal{B}}^* \leq 1 \tag{80}$$
$$q_{\mathcal{N} \backslash \mathcal{M}} = 0,$$

where $\|q\|_{\mathcal{A},\mathcal{B}}^* = \sup_{f \in \mathcal{B}} |\langle q, a(f,0) \rangle|$. Since $\mathcal{B}$ is defined as a union of multiple frequency bands, the inequality constraint in (80) can be expanded to p separate inequality constraints. It can be easily observed that (80) is a special case of (59) with all the weights being unity and $\mathcal{B} \subseteq [0,1]$ (i. e. the set of bands $\mathcal{B}$ need not necessarily cover the entire frequency range). While framing the semidefinite program for this problem, we use a linear matrix inequality similar to that in (74) with $\gamma = 1$ for each of the inequality constraint in (80), to cast the dual problem constraint into a semidefinite program. So, when all the frequencies are known to lie in p disjoint frequency bands, then the semidefinite program for the dual problem in (80) can be constructed by using p equality-form constraints:

$$\underset{q}{\text{maximize}} \ \langle q_{\mathcal{M}}, x_{\mathcal{M}} \rangle_{\mathbb{R}}$$
$$\boldsymbol{G}_{11}, \boldsymbol{G}_{12}, \cdots, \boldsymbol{G}_{1p},$$
$$\boldsymbol{G}_{21}, \boldsymbol{G}_{22}, \cdots, \boldsymbol{G}_{2p}$$

$$\text{subject to } q_{\mathcal{N} \setminus \mathcal{M}} = 0$$

$$\delta_{k_1} = \mathcal{L}_{k_1, f_{\mathcal{L}_2}, f_{\mathcal{H}_2}}(\boldsymbol{G}_{11}, \boldsymbol{G}_{21}), \qquad k_1 = 0, \cdots, n-1$$

$$\begin{bmatrix} \boldsymbol{G}_{11} & q \\ q^* & 1 \end{bmatrix} \succcurlyeq 0,$$

$$\delta_{k_2} = \mathcal{L}_{k_2, f_{\mathcal{L}_2}, f_{\mathcal{H}_2}}(\boldsymbol{G}_{12}, \boldsymbol{G}_{22}), \qquad k_2 = 0, \cdots, n-1$$

$$\begin{bmatrix} \boldsymbol{G}_{12} & q \\ q^* & 1 \end{bmatrix} \succcurlyeq 0, \tag{81}$$

$$\vdots$$

$$\delta_{k_p} = \mathcal{L}_{k_p, f_{\mathcal{L}_p}, f_{\mathcal{H}_p}}(\boldsymbol{G}_{1p}, \boldsymbol{G}_{2p}), \qquad k_p = 0, \cdots, n-1$$

$$\begin{bmatrix} \boldsymbol{G}_{1p} & q \\ q^* & 1 \end{bmatrix} \succcurlyeq 0,$$

$$\text{where } \boldsymbol{G}_{11}, \boldsymbol{G}_{12}, \cdots, \boldsymbol{G}_{1p} \in \mathbb{C}^{n \times n},$$

$$\text{and } \boldsymbol{G}_{21}, \boldsymbol{G}_{22}, \cdots, \boldsymbol{G}_{2p} \in \mathbb{C}^{(n-1) \times (n-1)}.$$

In the extreme case when any of the known frequency bands $\mathcal{B}_k$ have $\omega_{\mathcal{L}_k}$ or $\omega_{\mathcal{H}_k}$ lying exactly on either $-\pi$ or π, then the dual-polynomial in (81) should be appropriately translated as noted in (76).

In many applications, the location of *some* of the signal frequencies might be precisely known. One could think of this *known poles* problem as a probabilistic prior problem where the cardinality of *some* sets $\mathcal{B}_k$ is exactly unity (and the associated probability be unity as well), while the remaining frequency subbands have a non-unity probability. However, there are a few differences. For probabilistic priors, the probability distribution function is known for the entire interval [0,1] while, in case of known poles, the probability distribution of the bands of unknown frequencies is unavailable. Also,

unlike block prior formulation, known poles problem does not have zero probability associated with the remaining subbands.

Known Poles

We now consider the case when some frequency components are known *a priori* but their corresponding amplitudes and phases are not. Let the index set of all the frequencies be $\mathcal{S}$, $|\mathcal{S}| = s$. Let $\mathcal{P}$ be the index set of all the known frequencies, and $|\mathcal{P}| = p$. Namely, we assume that the signal x contains some known frequencies f_j, $j \in \mathcal{P} \subseteq \mathcal{S}$, $|\mathcal{P}| = p$. For known frequencies, let us denote their *complex* coefficients as d_j and their *phaseless frequency atoms* as $a_j[l] = a(f_j, 0)[l] = e^{i2\pi f_j l}$\$. We define the *conditional atomic norm* $\|\hat{x}\|_{\mathcal{A},\mathcal{P}}$ for the *known poles* as follows:

$$\|\hat{x}\|_{\mathcal{A},\mathcal{P}} = \inf_{c_j,d_j,f_j}\{\sum_{j=1}^{s-p}|c_j|: \hat{x}[l] = \sum_{j=1}^{s-p} c_j e^{i2\pi f_j l} + \sum_{j=s-p+1}^{s} d_j e^{i2\pi f_j l}, l \in \mathcal{M}\}, \tag{82}$$

Unlike previously mentioned *a priori* counterparts of the atomic norm, the semidefinite formulation for $\|\hat{x}\|_{\mathcal{A},\mathcal{P}}$ easily follows from (48).

Proposition 1. *The conditional atomic norm for a vector $\hat{x}$ is given by*

$$\|\hat{x}\|_{\mathcal{A},\mathcal{P}} = \inf_{T_n,\tilde{x},t,d_j} \{\frac{1}{2|\mathcal{N}|}tr(T_n) + \frac{1}{2}t: \begin{bmatrix} T_n & \tilde{x} \\ \tilde{x}^* & t \end{bmatrix} \succeq 0\}. \tag{83}$$

where $\tilde{x}[l] = \hat{x}[l] - \sum_{j\in\mathcal{P}} a_j[l]d_j$ represents the positive combination of complex sinusoids with unknown poles.

The conditional atomic norm minimization problem can be posed as the following semidefinite formulation in a similar way as in (52):

$$\underset{T_n,\hat{x},\tilde{x},t,d_j}{\text{minimize}} \frac{1}{2|\mathcal{N}|}tr(T_n) + \frac{1}{2}t$$
$$\text{subject to } \begin{bmatrix} T_n & \tilde{x} \\ \tilde{x}^* & t \end{bmatrix} \succeq 0 \tag{84}$$
$$\hat{x}[l] = x[l], \quad l \in \mathcal{M}$$

$$\hat{x}[l] = \tilde{x}[l] + \sum_{j \in \mathcal{P}} a_j[l] d_j, \qquad l \in \mathcal{M}.$$

The $\tilde{x}$ can be viewed as the signal filtered of the *known poles*. The remaining unknown frequencies in $\tilde{x}$ can be identified by the frequency localization approach that we restate for $\tilde{x}$ in Algorithm 1.

Algorithm 1. *Known poles* algorithm

1: Solve the semidefinite program (84) to obtain $\tilde{x}$.

2: Solve the following dual problem to obtain the optimum solution $q^\star$

$$\underset{q}{\text{maximize}} \ \langle q, \tilde{x} \rangle_{\mathbb{R}}$$

$$\text{subject to } \|q\|_{\mathcal{A}}^* \le 1 \qquad\qquad (85)$$

$$q[l] = 0, l \in \mathcal{N} \backslash \mathcal{M}.$$

3: The unknown frequencies f_j, $j \in \mathcal{P}$, identify as $\left|\langle q^*, a_j \rangle\right| = 1$. For $j \notin \mathcal{S} \backslash \mathcal{P}$, $\left|\langle q^*, a_j \rangle\right| < 1$.

4: Solve the following system of simultaneous linear equations to recover the complex coefficients of unknown frequencies: $\tilde{x}[l] - \sum_{j \in \mathcal{S} \backslash \mathcal{P}} c_j a_j[l] = 0$.

Performance Analysis

To identify the true frequencies of the signal from the solution of the dual problem, we now establish the conditions for finding the dual-certificate of support when prior information is available. We additionally show that the dual polynomial requirements can be slackened if the prior information gives the approximate location of each of the signal frequencies. We further put our result in the context of minimum number of signal samples required for the reconstruction of the signal x.

Since the primal problem (54) has only equality constraints, Slater's condition is satisfied. As a consequence, strong duality holds (Boyd and Vandenberghe 2004). This

allows us to present the dual-certificate of support for the optimizer of (54). In the following theorems, $\text{sign}(c_j) = c_j/|c_j|$, and $\Re(\cdot)$ denotes the real part (of a complex number).

Theorem 1. *Let the set of atoms* $\{a_{\mathcal{M}}(f_1, 0), \cdots, a_{\mathcal{M}}(f_s, 0)\}$ *supported on subset* $\mathcal{M}$ *of* $\mathcal{N}$ *be linearly independent. Then,* $\hat{x} = x$ *is the unique solution to the primal problem (54), if there exists a polynomial*

$$Q(f) = \langle q, a(f, 0) \rangle = \sum_{l=0}^{n-1} q_l e^{-i2\pi f l}, \tag{86}$$

such that

$$Q(f_j) = w_k \text{sign}(c_j), \forall f_j \in \mathcal{B}_k \subseteq [0,1] \tag{87}$$

$$|Q(f)| < w_k, \ \forall f \in (\mathcal{B}_k \backslash \mathcal{F}) \subset [0,1] \tag{88}$$

$$q_{\mathcal{N} \backslash \mathcal{M}} = 0. \tag{89}$$

As a corollary to Theorem **11**, we can arrive at the dual polynomial for the block prior problem as follows.

Corollary 2. *The* $\hat{x} = x$ *is the unique solution to the primal problem (79), if there exists a polynomial* $Q(f)$ *such that*

$$Q(f_j) = \text{sign}(c_j), \forall f_j \in \mathcal{F} \subset \mathcal{B} \tag{90}$$

$$|Q(f)| < 1, \ \forall f \in (\mathcal{B} \backslash \mathcal{F}) \tag{91}$$

$$q_{\mathcal{N} \backslash \mathcal{M}} = 0. \tag{92}$$

When the prior information is available to such a generous extent that each of the individual frequencies are known within close boundaries, as we present next, an interesting consequence of this relaxation is that the number of samples required to reconstruct the signal could be bounded.

Theorem 3. *Let the signal x as in (45) be sampled on a subset $\mathcal{M}$ of $\mathcal{N}$. If there exists a polynomial $Q(f)$ such that $\forall\, f_j \in \mathcal{F} \subset \mathcal{B}$,*

$$Q(f_j) = sign(c_j) \tag{93}$$

$$Q'(f_j) = \sum_{l=0}^{n-1} l q_l e^{-i2\pi f_j l} = 0 \tag{94}$$

$$Q''(f_j) = \sum_{l=0}^{n-1} -(2\pi l)^2 q_l e^{-i2\pi f_j l} = -sign\left(\Re(c_j)\right), \tag{95}$$

and, if each of the frequencies is known within a sufficiently small frequency subband, then $\hat{x} = x$ is the unique optimizer of the primal problem (79). Further, assuming f_js are distributed uniformly at random in $[0,1]$, such a dual polynomial exists with probability 1 when $m \geq 3s$.

The formulation in (77) generalizes the prior information. As the cases of *block priors* and *known poles* indicate, the more we know about the spectral structure of the signal, precise formulations of atomic norm minimization can be evaluated to boost signal recovery. If all poles are known in the sense of *known poles* algorithm (i.e., the amplitudes and phases of all known poles are unknown), then the signal x can be uniquely reconstructed using the randomly sampled support $x_{\mathcal{M}}$ where $|\mathcal{M}| = s$. Further, it is well known that if the signal is uniformly sampled, then the Prony's method can uniquely reconstruct the signal x using no more than $2s$ samples. In comparison, our results from Theorem 3 show that if each of the poles are *approximately known*, then the unique reconstruction of the signal x requires no more than $3s$ samples.

Numerical Experiments

We evaluated our algorithms through numerical experiments using the SDPT3 (Tütüncü et al. 2003) solver for the semidefinite programs. In all experiments, for a particular realization of the signal, the phases of the signal frequencies were sampled uniformly at random in $[0, 2\pi)$. The amplitudes $|c_j|$, $j = 1, \cdots, s$ were drawn randomly

from the distribution $0.5 + \chi_1^2$ where χ_1^2 represents the chi-squared distribution with 1 degree of freedom.

Probabilistic Priors

We evaluated the semidefinite program (77) for the case when $p = 2$. Here, $\mathcal{B}_1 = [0, 0.2]$ and $\mathcal{B}_1 = (0.2, 1]$ so that $\mathcal{B}_1 \cup \mathcal{B}_2 = [0,1]$. We consider the situation when the probability of occurrence of signal frequency in $\mathcal{B}_1$ is 1000 times higher than $\mathcal{B}_2$. This results in the pdf values of $p_F(f)|_{\mathcal{B}_1} = 4.9801$ and $p_F(f)|_{\mathcal{B}_2} = 0.005$. A suitable sub-optimal choice of $w(f)$ could be simply $w(f) = 1/p_F(f)$, so that the associated weights are given by $w_1 = 0.2008$ and $w_2 = 200.8000$. For each random realization of the signal, the signal frequencies are drawn randomly based on the given probability density function.

Experiment A.1. A simple illustration of the signal recovery using (77) is shown through frequency localization in Figure 19. For a signal of dimension $n = 64$ and number of frequencies $s = 5$, Figure 19(a) shows that even when all samples are observed ($m = 64$), the standard atomic norm minimization (52) is unable to recover any of the frequencies, for the maximum modulus of the dual polynomial assumes a value of unity at many other frequencies. However, given the probabilistic priors, semidefinite program (77) is able to perfectly recover all the frequencies as shown in Figure 19(b). Here, $|Q(f_j)| = w_1 = 0.2008$ for $f_j \in \mathcal{F} \subset \mathcal{B}_1$, and $|Q(f_j)| = w_2 = 200.8$ for $f_j \in \mathcal{F} \subset \mathcal{B}_2$.

(a) Without any priors
(b) With probabilistic priors

Figure 19. Frequency localization using dual polynomial for $\{n, s, m\} = \{64, 5, 64\}$. The probabilistic priors are $p_F(f)|_{\mathcal{B}_1 = [0,0.2]} = 4.9801$ and $p_F(f)|_{\mathcal{B}_2 = (0.2,1]} = 0.005$. The insets show the same plot on a smaller scale.
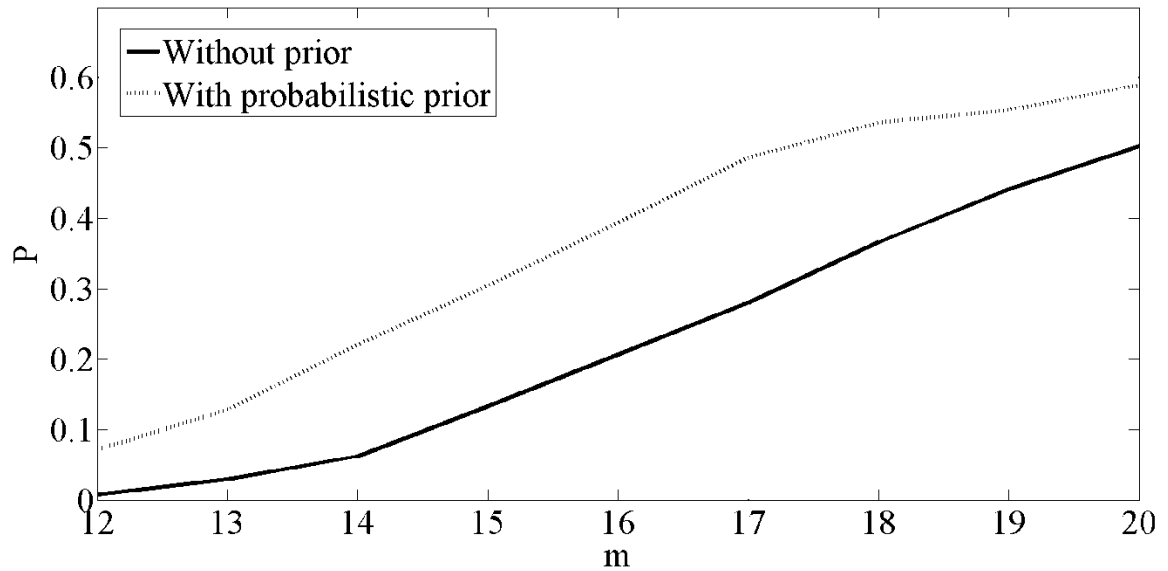
Figure 20. The probability P of perfect recovery over 1000 trials for $\{n, s\} = \{64, 5\}$. The probabilistic priors are $p_F(f)|_{\mathcal{B}_1 = \{[0,0.3] \cup (0.7,1]\}} = 0.0025$ and $p_F(f)|_{\mathcal{B}_2 = (0.3,0.7]} = 2.4963$.

Experiment A.2. A comparison of the statistical performance of (77) with the standard atomic norm for $n = 64$ is shown in Figure 20 over 1000 trials. Here, the pdf $p_F(f)$ is 1000 times higher in the subband $(0.3, 0.7]$ than the rest of the spectrum. We note that the weighted atomic norm is about twice more successful than the standard atomic norm in recovering the signal frequencies.

Block Priors

We evaluated the performance of spectrum estimation with block priors through numerical simulations for the semidefinite program in (81). Here, for every random realization of the signal, the frequencies are drawn uniformly at random in the set of subbands $\mathcal{B} = \cup_{k=1}^{s} \mathcal{B}_k \subset [0,1]$.

Experiment B.1. We first illustrate our approach through an example in Figure 21. Here for $n = 64$, we drew $s = 5$ frequencies uniformly at random within $p = 3$ subbands in the domain $[0, 1]$ without imposing any minimum separation condition. Here, $\mathcal{B} = (0.3500, 0.4800) \cup (0.6000, 0.8000) \cup (0.8500, 0.9000)$. A total of $m = 20$ observations were randomly chosen from n regular time samples to form the sample set $\mathcal{M}$. In the absence of any prior information, we solve (55) and show the result of frequency localization in Figure 21(a). Here, it is difficult to pick a unique set of $s = 5$ poles for which the maximum modulus of the dual polynomial is unity (which will actually correspond to recovered frequency poles). On the other hand, when block priors are given, Figure 21(b) shows that solving (81) provides perfect recovery of all the frequency components, where the recovered frequencies correspond to unit-modulus points of the dual polynomial.

Experiment B.2. We then give a statistical performance evaluation of our new method, compared with atomic norm minimization without any priors (55). The experimental setup and block priors are the same as in Figure 21 and no minimum separation condition was assumed while drawing frequencies uniformly at random in the

set $\mathcal{B}$. Figure 23(a) shows the probability P of perfect recovery for the two methods for fixed $n = 64$ but varying values of m and s. For every value of the pair $\{s, m\}$, we simulate 100 trials to compute P. We note that if the frequencies are approximately known, our method greatly enhances the recovery of continuous-valued frequencies.

(a) Without any priors   (b) With block priors
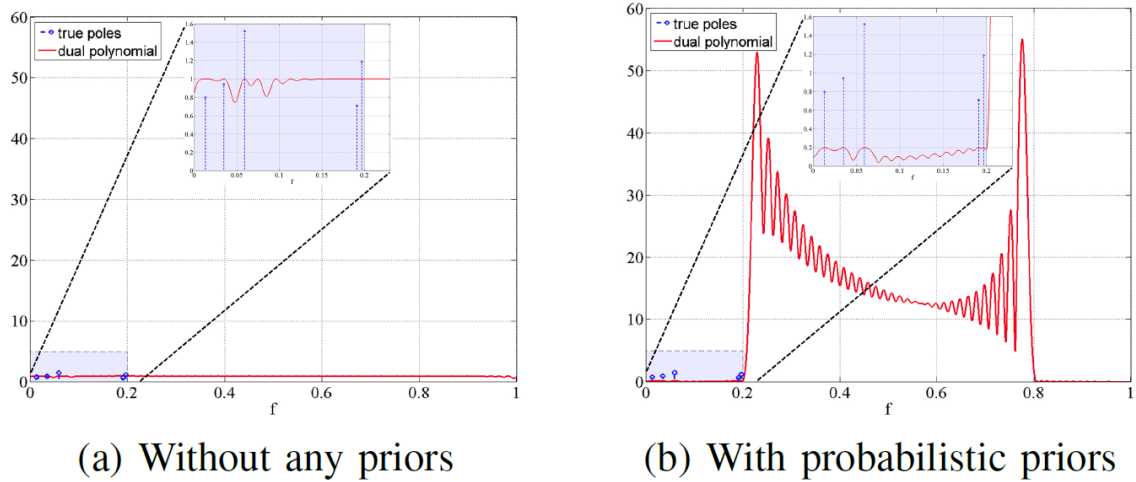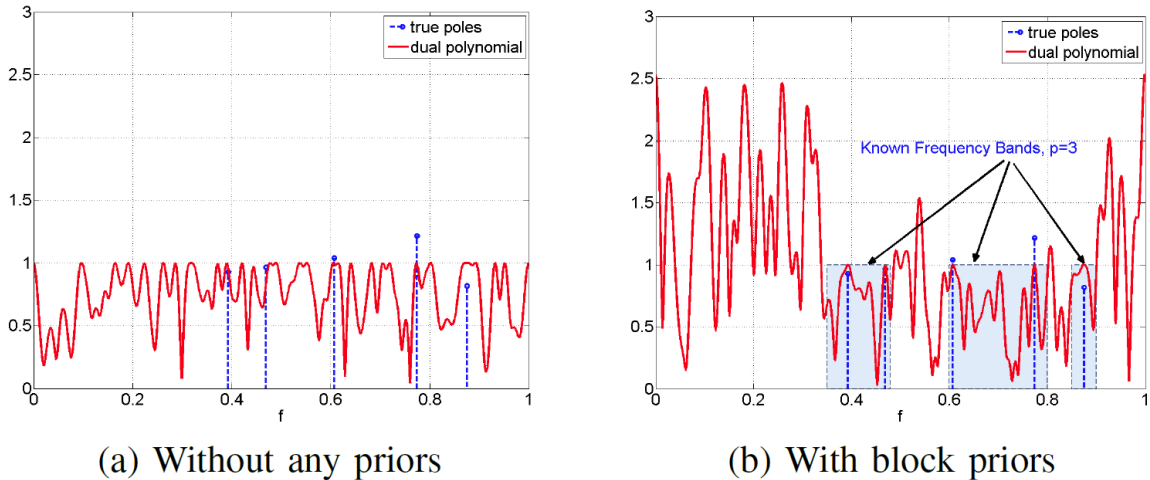
Figure 21. Frequency localization using dual polynomial for $\{n, s, m\} = \{64, 5, 20\}$. The block priors are
$$\mathcal{B} = [0.3500, 0.4800] \cup [0.6000, 0.8000] \cup [0.8500, 0.9000].$$

Experiment B.3. To illustrate the theoretical result of Theorem 3, we now consider the block prior problem when each of the frequencies are known to lie in extremely small subintervals. For the triplet $\{n, s, m\} = \{64, 7, 18\}$, Figure 22 depicts the frequency localization. In the absence of any prior knowledge, the standard atomic norm minimization of (52) fails to locate any of the signal frequencies (Figure 22(a)). However, if the frequencies are approximately known (or, in other words, the frequency subband of the block prior is very small), then the semidefinite program in (81) perfectly recovers the signal requiring not more than $3s$ number of samples ($m = 18 < 21 = $

$3s$), as shown in Figure 22(b). Here, the block priors consist of narrow frequency bands around each true pole f_j such that $\mathcal{B} = \bigcup_{k=1}^{s} \mathcal{B}_k = \bigcup_{k=1}^{s}[f_j - 0.001, f_j + 0.001]$.
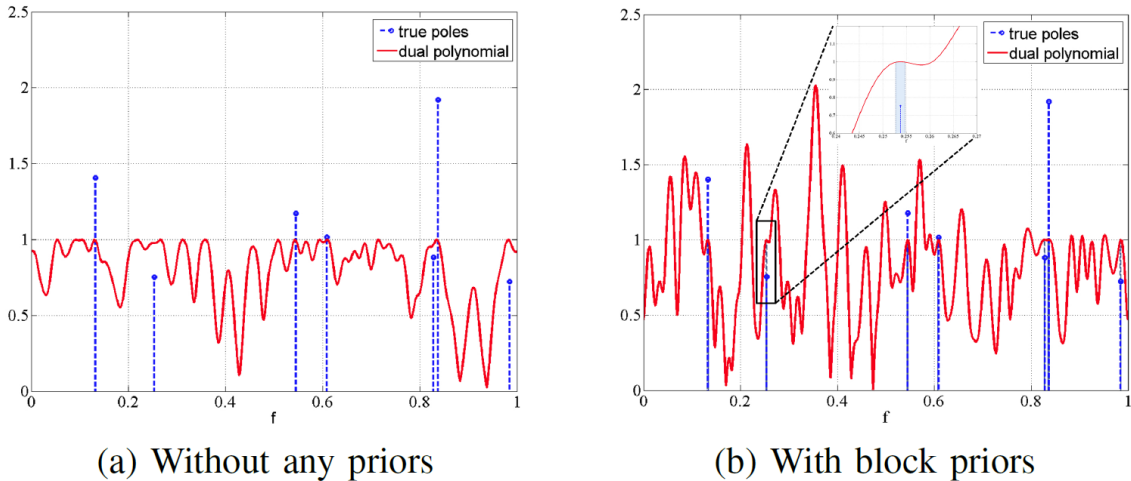
Figure 22. Frequency localization using dual polynomial for $\{n, s, m\} = \{64, 7, 18\}$. The block priors consist of small frequency bands around each true pole f_j such that $\mathcal{B} = \bigcup_{k=1}^{s} \mathcal{B}_k = \bigcup_{k=1}^{s}[f_j - 0.001, f_j + 0.001]$. The right plot has been magnified in the inset to show the size of the block prior.

Experiment B.4. For the same signal dimension, size and number of blocks as in the previous experiment, Figure 23(b) shows a comparison of statistical performance of block prior method with the standard atomic norm minimization over 100 trials. For every s, the parameter m was varied until m was at least $3s$. (Note that the perfect recovery with $3s$ samples in Theorem 3 holds only when the block prior is arbitrarily small.)
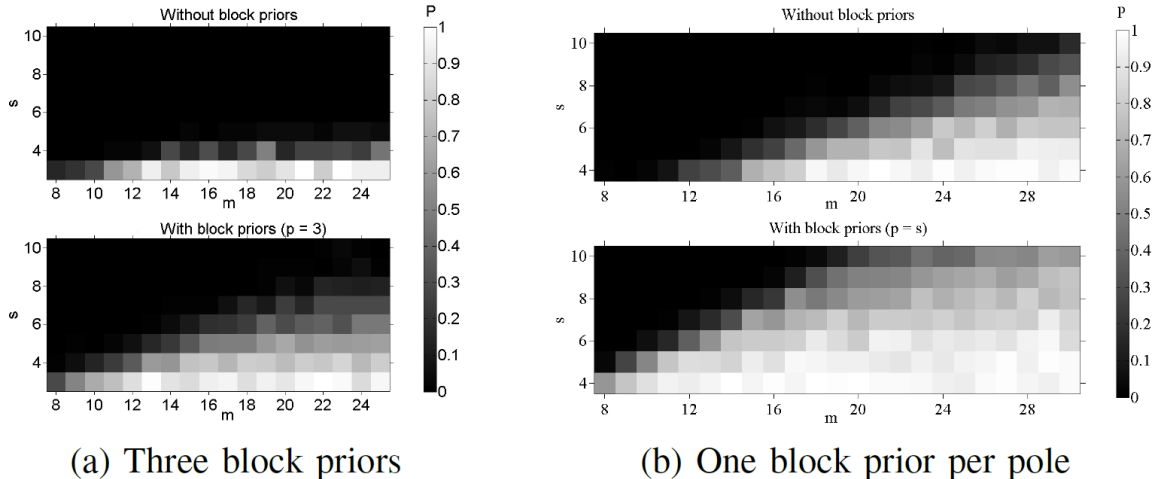
Figure 23. The probability P of perfect recovery over 100 trials for $n = 64$. The performance of standard atomic norm is compared with the block prior setups of Figure 21 (left) and Figure 22 (right).

Known Poles

We evaluated the *known poles* algorithm through a number of simulations to solve the semidefinite program (84). In all our experiments, the s frequencies of the artificially generated signal were drawn at random in the band $[0, 1]$. Except for Experiment 4, the sampled frequencies were also constrained to have the minimum modulo spacing of $\Delta_f = 1/\lfloor (n-1)/4 \rfloor$ between the adjacent frequencies. This is the theoretical resolution condition for the results in (Tang et al. 2013b), although numerical experiments suggested that frequencies could be closer, i.e., Δ_f could be $1/(n-1)$. While working with the *known poles*, we draw the first known frequency uniformly at random from the set of s frequencies. As the number p of *known poles* increases, we retain the previously drawn known frequencies and draw the next known frequency uniformly at random from the remaining set of existing signal frequencies.

Experiment C.1. We simulated a low-dimensional model with the triple $(n, m, s) = (32, 9, 4)$ and first solved the semidefinite program (52) which does not use any prior information, i.e., $p = 0$. For the same realization of the signal, we then

successively increase p up to $s - 1$, and solve the optimization (84) of the *known poles* algorithm. At every instance of solving an SDP, we record the number k of successfully recovered frequencies along with their complex coefficients. This number also includes the known frequencies if the recovery process returns exact values of their complex coefficients. $k = s$ corresponds to *complete success*, i.e., recovering all of the unknown spectral content. $k = 0$ is *complete failure*, including the case when the complex coefficients of the known frequencies could not be recovered. Figure 24(a) shows the probability P of recovering k frequencies over 1000 trials. Although the complex coefficients of the known frequencies were unknown, the *known poles* algorithm increases the probability of recovering all or some of the unknown spectral content.

Experiment C.2. We repeat the first experiment for the higher-dimensional pair $\{n, m\} = \{256, 40\}$ and vary s. The probability P over 100 random realizations of the signal is shown in Figure 25 for selected values of s. Here, the probability of successfully recovering all the frequencies using the *known poles* Algorithm 1 increases with p.

Experiment C.3. Figure 24(b) shows the probability P of *complete success* as a function of m over 100 trials for the twin $\{n, s\} = \{80, 6\}$. We note that the *known poles* algorithm achieves the same recovery probability when compared to (52) with a smaller number of random observations.

Experiment C.4. We now consider these two cases: (a) when $\Delta_f = 1/(n - 1)$, the resolution limit for the numerical experiments in (Tang et al. 2013b), and (b) when the frequencies are drawn uniformly at random and do not adhere to any minimum resolution conditions. Figure 26 shows the probability P of recovering k frequencies over 1000 trials for the triple $\{n, m, s\} = \{40, 15, 7\}$. We note that the probability of *complete success* with *known poles* suffers relatively little degradation for the random frequency resolutions. These trials include instances when the minimum resolution condition does not hold, formulation in (52) shows *complete failure* but the *known poles* algorithm recovers the unknown spectral content with *complete success*.
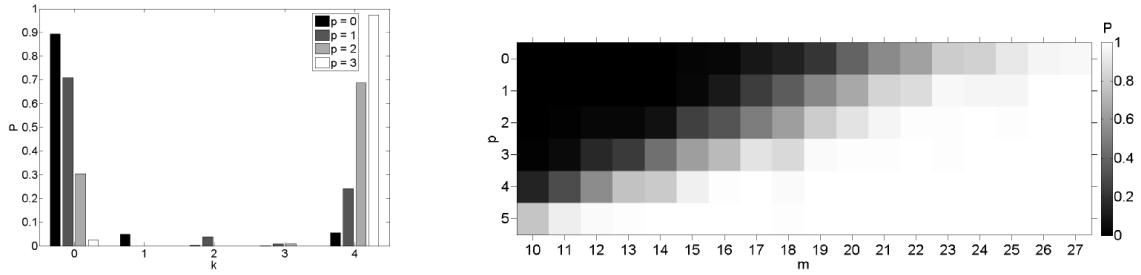
Figure 24. The probability P of recovering the unknown spectral content. The probability is computed for 1000 random realizations of the signal for the triple $\{n, m, s\} = \{32, 9, 4\}$. (For $k > 0$, $k \leq p$ being the invalid cases, the corresponding bars have been omitted.) (b) A higher probability P of recovering all the unknown frequency content can be achieved with a smaller number m of random observations using the *known poles* algorithm. The probability is computed for 100 random realizations with $\{n, s\} = \{80, 6\}$.
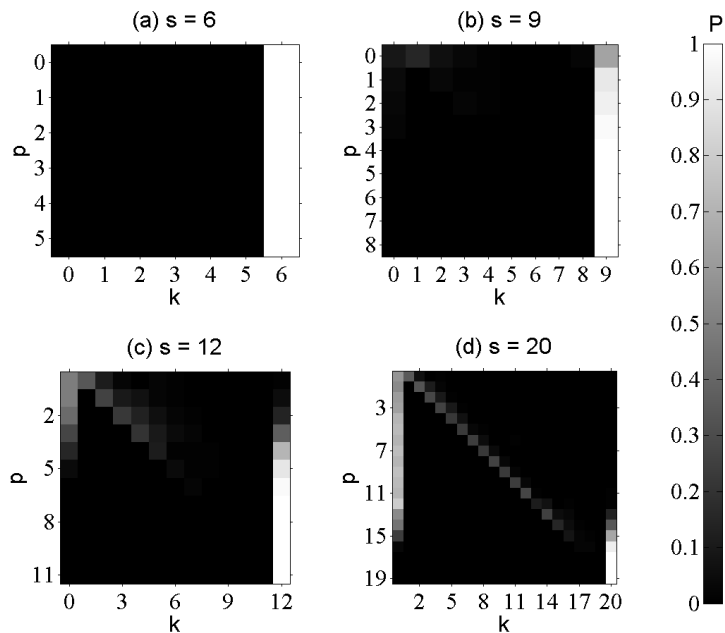
Figure 25. The probability P of recovering the unknown spectral content for selected values of s. The probability is computed for 100 random realizations of the signal with $\{n, m\} = \{256, 40\}$. (The lower diagonal cases when $k > 0$, $k \leq p$ are invalid, and do not contribute to the result.)
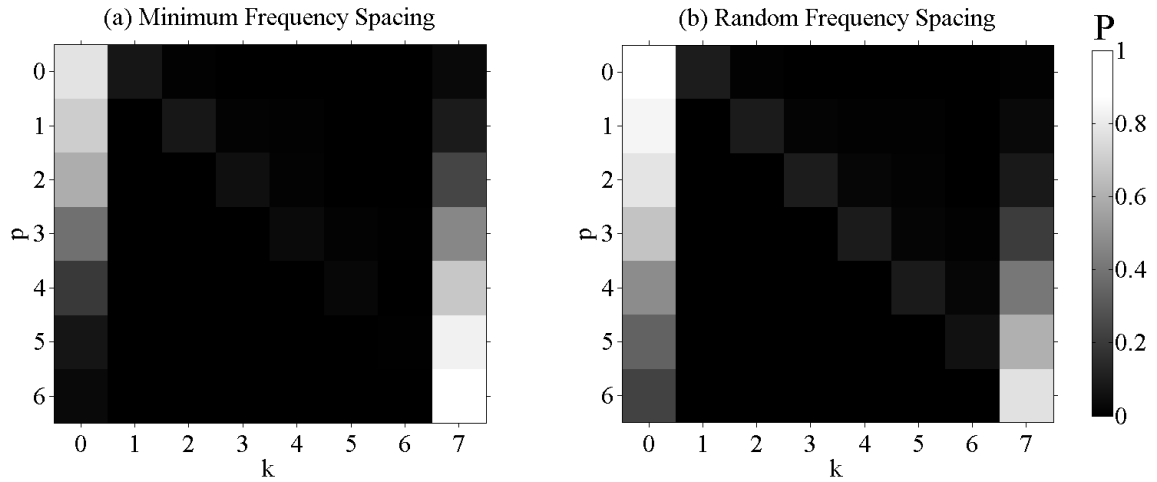
Figure 26. Performance of the *known poles* algorithm when the frequencies do not satisfy any nominal resolution conditions. The probability P of successfully recovering k frequencies is computed for 1000 realizations of the signal with dimensions $\{n, m, s\} = \{40, 15, 7\}$. (a) $\Delta_f = 1/(n-1)$ (b) Frequencies are selected uniformly at random in the band $[0, 1]$.

CHAPTER 7

SUMMARY AND FUTURE WORK

We proposed an innovative meteorological radar, which uses reduced number of spatiotemporal samples without compromising the accuracy of target information. Our approach extends recent research on compressed sensing (CS) for radar remote sensing of hard point scatterers to volumetric targets. The previously published CS-based radar techniques are not applicable for sampling weather since the precipitation echoes lack sparsity in both range-time and Doppler domains. Therefore we proposes an alternative approach by adopting the latest advances in matrix completion algorithms to demonstrate the sparse sensing of weather echoes. We used Iowa X-band Polarimetric (XPOL) radar data to test and illustrate our algorithms. This research opens a number of interesting avenues for the future work. We discuss some of these in the following sections.

Other Sparsity Models

In this research, we have made initial investigations in the sparse representation of weather radar data. One of the future research problems to consider is to extensively consider other possibilities for sparse dictionaries. This may involve dictionary learning using real weather radar data, or finding stable embeddings in high-dimensional manifolds. Even for a low-rank matrix, several other formulations are possible given prior knowledge of the signal structure. We considered some of these, for example, in Chapter 5.

Establishing other parsimonious models of weather data and accurately learning its structure is key to sparse sensing using weather radar. We may also consider the multiple-frames of radar scans for a more sophisticated signal structure. Modeling the weather data as a manifold which has a low-dimensional embedding is another promising signal model that has witnessed state-of-the-art research recently (Wakin 2010).

Attenuation Correction

As the radar signal propagates in the rain medium, it suffers differential attenuation in two polarizations. One of the matrix completion benefits could be to efficiently recover the weak signals at far range than what is possible using standard attenuation correction methods. Further, when the radar signal becomes completely extinct due to heavy precipitation, it will be interesting to recover the signal using data from other radars while also using matrix recovery algorithms.

Faster Matrix Completion Algorithms

The nuclear norm minimization, though accurate, is computationally expensive. In practice, any operational implementation of the sparse sensing using weather radar would require a real-time implementation of the matrix completion. Therefore, one of the future research areas is to explore faster algorithms for matrix recovery. As an example, we used LMaFit algorithm in Chapter 4 that yielded reasonable error with almost real-time recovery.

A possible research could be in the area of Bayesian matrix completion (Alquier et al. 2014) that uses prior statistical knowledge of the signal for matrix recovery. For precipitation, the received signal in dual-polarized weather radar is a bivariate complex Gaussian random variable. For Bayesian matrix completion, the distribution of individual I/Q samples can be used as a statistical prior.

Differential SNR-based Sampling

The results in this chapter demonstrate that low-rank nature of weather signal can be successfully harnessed for accelerating the scans of weather radars. So far, the sampling of the weather signal that we have considered is uniformly at random. However, other variations of this approach can be formulated for the sparse sensing in precipitation radars.

Since every range profile of the meteorological variable is a result of averaging of several returns from multiple pulses, a natural sparse sensing would be to randomly miss a few pulses for each ray. The result would be differential signal-to-noise ratio (SNR) for each ray. With this prior information, it is possible to pose a different matrix completion problem that has constraints of differential SNRs for each ray.

REFERENCES

Alquier, P., V. Cottet, N. Chopin, and J. Rousseau, 2014: Bayesian matrix completion: prior specification and consistency. *arXiv preprint arXiv:1406.1440*.

Azais, J.-M., Y. De Castro, and F. Gamboa, 2013: Spike detection from inaccurate samplings. *arXiv preprint arXiv:1301.5873*.

Balakrishnan, N., and D. S. Zrnić, 1990: Use of polarization to characterize precipitation and discriminate large hail. *Journal of the Atmospheric Sciences*, **47,** 1525-1540.

Baraniuk, R., and P. Steeghs, 2007: Compressive radar imaging. *IEEE Radar Conference*, 128-133.

Baraniuk, R. G., 2007: Compressive sensing [lecture notes]. *IEEE Signal Processing Magazine*, **24,** 118-121.

Baraniuk, R. G., V. Cevher, M. F. Duarte, and C. Hegde, 2010: Model-based compressive sensing. *IEEE Transactions on Information Theory*, **56,** 1982-2001.

Battan, L. J., 1973: *Radar observation of the atmosphere.* University of Chicago Press, 324 pp.

Berne, A., and R. Uijlenhoet, 2006: Quantitative analysis of X-band weather radar attenuation correction accuracy. *Natural Hazards and Earth System Science*, **6,** 419-425.

Beygi, S., and U. Mitra, 2014: Multi-scale multi-lag channel estimation using low rank structure of received signal. *IEEE International Conference on Acoustics, Speech and Signal Processing, ICASSP'14*.

Borque, P., P. Kollias, and S. Giangrande, 2014: First observations of tracking clouds using scanning ARM cloud radars. *Journal of Applied Meteorology and Climatology*, **53,** 2732-2746.

Bourguignon, S., H. Carfantan, and J. Idier, 2007: A sparsity-based method for the estimation of spectral lines from irregularly sampled data. *IEEE Journal on Selected Topics in Signal Processing*, **1,** 575-585.

Boyd, S. P., and L. Vandenberghe, 2004: *Convex optimization.* Cambridge university press, 226 pp.

Bringi, V. N., and V. Chandrasekar, 2001: *Polarimetric doppler weather radar: Principles and applications.* Cambridge University Press.

Bringi, V. N., R. Thurai, and R. Hannesen, 2007: *Dual-Polarization weather radar handbook.* Second ed. AMS-Gematronik GmbH.

Cai, J.-F., E. J. E.J. Candès, and Z. Shen, 2010: A singular value thresholding algorithm for matrix completion. *SIAM Journal on Optimization*, **20,** 1956-1982.

Candès, E. J., and B. Recht, 2009: Exact matrix completion via convex optimization. *Foundations of Computational Mathematics*, **9,** 717-772.

Candès, E. J., and Y. Plan, 2010: Matrix completion with noise. *Proceedings of the IEEE*, **98,** 925-936.

Candès, E. J., and C. Fernandez-Granda, 2013: Towards a mathematical theory of super-resolution. *Communications on Pure and Applied Mathematics*, **67,** 906-956.

Candès, E. J., J. Romberg, and T. Tao, 2006: Robust uncertainty principles: Exact signal reconstruction from highly incomplete frequency information. *IEEE Transactions on Information Theory*, **52,** 489-509.

Candès, E. J., X. Li, Y. Ma, and J. Wright, 2011: Robust Principal Component Analysis? *Journal of the ACM*, **58,** 11:11-11:37.

Carathèodory, C. C., 1911: Über ber den variabilitätsbereich der fourierschen konstanten von positiven harmonischen funktionen. *Rendiconti del Circolo Matematico di Palermo (1884-1940)*, **32,** 193-217.

Cevher, V., M. F. Duarte, C. Hegde, and R. Baraniuk, 2008: Sparse signal recovery using Markov random fields. *Advances in Neural Information Processing Systems*, 257-264.

Cevher, V., P. Indyk, C. Hegde, and R. G. Baraniuk, 2009: Recovery of clustered sparse signals from compressive measurements. *International Conference on Sampling Theory and Applications, SAMPTA'09*.

Chandrasekar, V., V. N. Bringi, and P. J. Brockwell, 1986: Statistical properties of dual polarized radar signals. *23rd AMS Conference on Radar Meteorology* Snowmass, Colorado, 154-157.

Chandrasekaran, V., B. Recht, P. A. Parrilo, and A. S. Willsky, 2012: The convex geometry of linear inverse problems. *Foundations of Computational Mathematics*, **12,** 805-849.

Chi, Y., and Y. Chen, 2013: Compressive recovery of 2-D off-grid frequencies. *Proceedings of Asilomar Conference on Signals, Systems, and Computers*.

Chi, Y., L. L. Scharf, A. Pezeshki, and A. R. Calderbank, 2011: Sensitivity to basis mismatch in compressed sensing. *IEEE Transactions on Signal Processing*, **59,** 2182-2195.

Chow, V. T., D. R. Maidment, and L. W. Mays, 1988: *Applied Hydrology.* McGraw-Hill, 570 pp.

Ciach, G. J., and W. F. Krajewski, 1999a: On the estimation of radar rainfall error variance. *Advances in Water Resources*, **22,** 585–595.

——, 1999b: Radar-rain gauge comparisons under observational uncertainties. *Journal of Applied Meteorology*, 1519–1525.

Cloude, S. R., 2010: *Polarization: Applications in remote sensing.* Oxford University Press.

Cremonini, R., L. Baldini, E. Gorgucci, V. Romaniello, R. Bechini, and V. Campana, 2010: Observations of precipitation with X-band and C-band polarimetric radars in Piedmont region (Italy). *Sixth European Conference on Radar in Meteorology and Hydrology*, Sibiu, Romania.

Delrieu, G., S. Serrar, E. Guardo, and J. D. Creutin, 1999: Rain measurement in hilly terrain with X-band weather radar systems: Accuracy of path-integrated attenuation estimates derived from mountain returns. *Journal of Atmospheric and Oceanic Technology*, **16,** 405-416.

Donoho, D. L., 2006a: Compressed sensing. *IEEE Transactions on Information Theory*, **52,** 1289-1306.

——, 2006b: Compressed sensing. *IEEE Transactions on Information Theory*, **52,** 1289-1306.

Doviak, R. J., and D. S. Zrnić, 1993: *Doppler radar and weather observations.* Dover Publications, Inc.

Duarte, M. F., and Y. C. Eldar, 2011: Structured compressed sensing: From theory to applications. *IEEE Transactions on Signal Processing*, **59,** 4053-4085.

Duarte, M. F., and R. G. Baraniuk, 2013: Spectral compressive sensing. *Applied and Computational Harmonic Analysis*, **35,** 111-129.

Dumitrescu, B., 2007: Positive trigonometric polynomials and signal processing applications. Springer.

Ebtehaj, A. M., E. Foufoula-Georgiou, and G. Lerman, 2012: Sparse regularization for precipitation downscaling. *Journal of Geophysical Research: Atmospheres (1984– 2012)*, **117**.

Ender, J. H., 2010: On compressive sensing applied to radar. *Signal Processing*, **90,** 1402-1414.

Fannjiang, A., and W. Liao, 2012: Coherence pattern-guided compressive sensing with unresolved grids. *SIAM Journal on Imaging Sciences*, **5,** 179-202.

Fannjiang, A., P. Yan, and T. Strohmer, 2010: Compressed remote sensing of sparse objects. *SIAM Journal on Imaging Sciences*, **3,** 596-618.

Fannjiang, A. C., 2011: The MUSIC algorithm for sparse objects: a compressed sensing analysis. *Inverse Problems*, **27,** 35013-35044.

Fejér, L., 1915: Über trigonometriche polynome. *Journal für die Reine und Angewandte Mathematik*, **146,** 53-82.

Fjørtoft, R., and A. Lopès, 2001: Estimation of the mean radar reflectivity from a finite number of correlated samples. *IEEE Transactions on Geoscience and Remote Sensing*, **39,** 196-199.

Galvez, M. B., J. Colom, V. Chandrasekar, F. Junyent, S. Cruz-Pol, and R. Rodriguez, 2009: Salient features of the radar nodes in the Puerto Rico tropical weather testbed. *IEEE Geoscience and Remote Sensing Symposium*, Cape Town, IEEE, 841-844.

Gebremichael, M., and W. F. Krajewski, 2004: Characterization of the temporal sampling error in space-time-averaged rainfall estimates from satellites. *Journal of Geophysical Research: Atmospheres (1984–2012)*, **109**.

Gekat, F., P. Meischner, K. Friedrich, M. Hagen, J. Koistinen, D. B. Michelson, and A. Huuskonen, 2004: The state of weather radar operations, networks and products. *Weather radar: Principles and advanced applications*, P. Meischner, Ed., Springer-Verlag, 9.

Habib, E., G. Lee, D. Kim, and G. J. Ciach, 2010: Ground-based direct measurement. *Rainfall: State of the science*, F. Y. Testik, and M. Gebremichael, Eds., American Geophysical Union, 61-77.

Harris, F. J., 1978: On the use of windows for harmonic analysis with the discrete Fourier transform. *Proceedings of the IEEE*, **66,** 51-83.

He, Y., X. Zhu, S. Zhuang, H. Li, and H. Hu, 2011: Waveform optimization for compressive sensing radar imaging. *IEEE CIE International Conference on Radar*, IEEE, 1263–1266.

Hegde, C., M. F. Duarte, and V. Cevher, 2009: Compressive sensing recovery of spike trains using a structured sparsity model. *Signal Processing with Adaptive Sparse Structured Representations, SPARS'09*.

Hendry, A., and Y. M. M. Antar, 1984: Precipitation particle identification with centimeter wavelength dual-polarization radars. *Radio Science*, **19,** 115-122.

Hendry, A., G. C. McCormick, and B. L. Barge, 1976: The degree of common orientation of hydrometeors observed by polarization diversity radars. *Journal of Applied Meteorology*, **15,** 633-640.

Herman, M. A., and T. Strohmer, 2009: High-resolution radar via compressed sensing. *IEEE Transactions on Signal Processing*, **57,** 2275-2284.

Huang, T., Y. Liu, H. Meng, and X. Wang, 2012: Adaptive matching pursuit with constrained total least squares. *EURASIP Journal on Advances in Signal Processing*, **2012,** 1-12.

Iguchi, T., H. Hanado, N. Takahashi, S. Kobayashi, and S. Satoh, 2003: The dual-frequency precipitation radar for the GPM core satellite. *IEEE Geoscience and Remote Sensing Symposium*, Toulouse, France, IEEE, 1698-1700.

Illingworth, A. J., and I. J. Caylor, 1991: Correlation measurements of precipitation. *25th International Conference on Radar Meteorology*, Paris, France, American Meteorological Society, 650-653.

Ji, S., Y. Xue, and L. Carin, 2008: Bayesian compressive sensing. *IEEE Transactions on Signal Processing*, **56,** 2346-2356.

Kabeche, F., J. F. i Ventura, B. Fradon, R. Hogan, A.-A. Boumahmoud, A. Illingworth, and P. Tabary, 2010: Towards X-band polarimetric quantitative precipitation estimation in mountainous regions: The RHYTMME project. *Sixth European Conference on Radar in Meteorology and Hydrology*, Sibiu, Romania.

Kalogerias, D., S. Sun, and A. Petropulu, 2013: Sparse sensing in colocated MIMO radar: A matrix completion approach. *IEEE International Symposium on Signal Processing and Information Technology*, Athens, Greece, IEEE, 496-502.

Keeler, R. J., and R. E. Passarelli, 1990: Signal processing for atmospheric radars. *Radar in Meteorology*, D. Atlas, Ed., American Meteorological Society, 109–121.

Khajehnejad, M. A., W. Xu, A. S. Avestimehr, and B. Hassibi, 2009: Weighted ℓ_1 minimization for sparse recovery with prior information. *IEEE International Symposium on Information Theory*, 483-487.

Klazura, G. E., and D. A. Imy, 1993: A description of the initial set of analysis products available from the NEXRAD WSR-88D system. *Bulletin of the American Meteorological Society*, **74,** 1293-1311.

Krajewski, W. F., 2007: Ground networks: Are we doing the right thing? *Measuring precipitation from space: EURAINSAT and the future*, V. Levizzani, P. Bauer, and F. J. Turk, Eds., Springer, 403-418.

Krajewski, W. F., and J. A. Smith, 2002: Radar hydrology: Rainfall estimation. *Advances in Water Resources*, **25,** 1387-1394.

Krajewski, W. F., E. N. Anagnostou, and G. J. Ciach, 1996: Effects of the radar observation process on inferred rainfall statistics. *Journal of Geophysical Research: Atmospheres (1984–2012)*, **101,** 26493-26502.

Krajewski, W. F., G. J. Ciach, and E. Habib, 2003: An analysis of small scale rainfall variability in different climatological regimes. *Hydrologic Sciences Journal*, **48,** 151-162.

Krajewski, W. F., G. Villarini, and J. A. Smith, 2010: RADAR-Rainfall uncertainties: Where are we after thirty years of effort? *Bulletin of the American Meteorological Society*, **91,** 87-94.

Kruger, A., and W. F. Krajewski, 1997: Efficient storage of weather radar data. *Software-Practice and Experience*, **27,** 623-636.

Kummerow, C., and Coauthors, 2000: The status of the Tropical Rainfall Measuring Mission (TRMM) after two years in orbit. *Journal of Applied Meteorology*, **39,** 1965-1982.

Lapczak, S., and Coauthors, 1999: The Canadian national radar project. *29th Conference on Radar Meteorology*, Montreal, American Meteorological Society, 327-330.

Lee, J.-S., and E. Pottier, 2009: *Polarimetric radar imaging: From basics to applications.* First ed. CRC Press.

Lellouch, G., R. Pribic, and P. Van Genderen, 2009: Merging frequency agile ofdm waveforms and compressive sensing into a novel radar concept. *European Radar Conference*, 137–140.

Li, L., D. Li, B. Liu, Q. Zhang, and L. Wei, 2012: Three-aperture inverse synthetic aperture radar moving targets imaging processing based on compressive sensing. *8th IEEE International Symposium on Instrumentation and Control Technology*, 210-214.

Liao, W., and A. Fannjiang, 2014: MUSIC for single-snapshot spectral estimation: Stability and super-resolution. *arXiv preprint arXiv:1404.1484*.

Lin, Y., and K. E. Mitchell, 2005: The NCEP Stage II/IV hourly precipitation analyses: development and applications. *19th Conference on Hydrology*, San Diego, USA, American Meteorological Society.

Linebarger, D. A., R. D. DeGroat, E. M. Dowling, P. Stoica, and G. L. Fudge, 1995: Incorporating a priori information into MUSIC-algorithms and analysis. *Signal Processing*, **46,** 85-104.

Ma, J., 2009: Single-pixel remote sensing. *IEEE Geoscience and Remote Sensing Letters*, **6,** 199-203.

Ma, J., and F.-X. Le Dimet, 2009: Deblurring from highly incomplete measurements for remote sensing. *IEEE Transactions on Geoscience and Remote Sensing*, **47,** 792-802.

Maki, M., and Coauthors, 2010: X-band polarimetric radar networks in urban areas. *Sixth European Conference on Radar in Meteorology and Hydrology*, Sibiu, Romania.

Marple Jr., S. L., 1987: Digital spectral analysis with applications. Englewood Cliffs, NJ, Prentice-Hall, Inc.

McCormick, G. C., and A. Hendry, 1979: Techniques for the determination of the polarization properties of precipitation. *Radio Science*, **14,** 1027-1040.

McLaughlin, D., D. Pepyne, B. Philips, J. Kurose, M. Zink, D. Westbrook, and E. Lyons, 2009: Short-wavelength technology and the potential for distributed networks of small radar systems. *Bulletin of the American Meteorological Society*, **90,** 1797-1817.

Mishali, M., and Y. C. Eldar, 2010: From theory to practice: Sub-Nyquist sampling of sparse wideband analog signals. *IEEE Journal of Selected Topics in Signal Processing*, **4,** 375-391.

Mishra, K. V., 2012: Frequency diversity wideband digital receiver and signal processor for solid-state dual-polarimetric weather radars, Electrical Engineering, Colorado State University, 158 pp.

Mishra, K. V., W. F. Krajewski, R. Goska, D. Ceynar, B.-C. Seo, A. Kruger, and W. Petersen, 2014: Filling Gaps in spatial continuity of large wavelength radar coverage of precipitation: Comparative analysis using Iowa XPOL observations during the NASA GPM IFloodS campaign. *International Weather Radar and Hydrology Symposium*, Washington DC.

Ozturk, S., T.-Y. Yu, L. Ding, N. Feng, and B. L. Cheong, 2013: Application of compressive sensing to atmospheric observations with imaging radar. *36th Conference on Radar Meteorology*, Breckenridge, Colorado, American Meteorological Society.

Papoulis, A., and S. U. Pillai, 2002: *Probability, random variables and stochastic processes.* Fourth ed. McGraw-Hill.

Pazmany, A. L., J. B. Mead, H. B. Bluestein, J. C. Snyder, and J. B. Houser, 2013: A mobile rapid-scanning X-band polarimetric (RaXPol) Doppler radar system. *Journal of Atmospheric and Oceanic Technology*, **30,** 1398-1413.

Potter, L. C., E. Ertin, J. T. Parker, and M. Cetin, 2010: Sparsity and compressed sensing in radar imaging. *Proceedings of the IEEE*, **98,** 1006-1020.

Probert-Jones, J. R., 1962: The radar equation in meteorology. *Quarterly Journal of the Royal Meteorological Society*, **88,** 485-495.

Pruente, L., 2010: Application of compressed sensing to SAR/GMTI-data. *8th European Conference on Synthetic Aperture Radar*, 1-4.

Pruppacher, H. R., and K. V. Beard, 1970: A wind tunnel investigation of the internal circulation and shape of water drops fall at terminal velocity in air. *Quarterly Journal of Royal Meteorological Society*, **96,** 247-256.

Ryzhkov, A., Zrnić D. S., J. C. Hubbert, V. N. Bringi, J. Vivekanandan, and E. A. Brandes, 2002: Polarimetric radar observations and interpretation of co-cross-polar correlation coefficients. *Journal of Atmospheric and Oceanic Technology*, **19,** 340-354.

Sachidananda, M., and D. S. Zrnić, 1985: ZDR measurement considerations for a fast scan capability radar. *Radio Science*, **20,** 907-922.

Scherier, P. J., and L. L. Scharf, 2010: *Statistical signal processing of complex-valued data: The theory of improper and noncircular signals.* Cambridge University Press.

Schneebeli, M., N. Dawes, M. Lehning, and A. Berne, 2013: High-resolution vertical profiles of X-band polarimetric radar observables during snowfall in the Swiss Alps. *Journal of Applied Meteorology and Climatology*, **52,** 378-394.

Scipión, D. E., R. Mott, M. Lehning, M. Schneebeli, and A. Berne, 2013: Seasonal small-scale spatial variability in alpine snowfall and snow accumulation. *Water Resources Research*, **49,** 1446-1457.

Seliga, T. A., and V. N. Bringi, 1976: Potential use of radar differential reflectivity measurements at orthogonal polarizations for measuring precipitation. *Journal of Applied Meteorology*, **15,** 69-76.

Seliga, T. A., and V. N. Bringi, 1978: Differential reflectivity and differential phase shift: applications in Radar Meteorology. *Radio Science*, **13,** 271-275.

Seo, D. J., and J. A. Smith, 1996: Characterization of the climatological variability of mean areal rainfall through fractional coverage. *Water Resources Research*, **32,** 2087-2095.

Shen, Y., Z. Wen, and Y. Zhang, 2014: Augmented Lagrangian alternating direction method for matrix separation based on low-rank factorization. *Optimization Methods and Software*, **29,** 239-263.

Siggia, A., and R. Passarelli Jr, 2004: Gaussian model adaptive processing (GMAP) for improved ground clutter cancellation and moment calculation. *Proceedings of ERAD*.

Skolnik, M. I., 2008a: Radar handbook. McGraw-Hill.

——, 2008b: *Radar handbook.* Third ed. McGraw-Hill.

Smith, J. A., D. J. Seo, M. L. Baeck, and M. D. Hudlow, 1996: An intercomparison study of NEXRAD precipitation estimates. *Water Resources Research*, **32,** 2035-2045.

Sonka, M., V. Hlavac, and R. Boyle, 2014: *Image processing, analysis, and machine vision.* Cengage Learning.

Stoica, P., and R. L. Moses, 2005: Spectral analysis of signals. Prentice Hall.

Stojnic, M., F. Parvaresh, and B. Hassibi, 2009: On the reconstruction of block-sparse signals with an optimal number of measurements. *IEEE Transactions on Signal Processing*, **57,** 3075-3085.

Tabary, P., 2007: The New French Operational Radar Rainfall Product. Part I: Methodology. *Weather and Forecasting*, **22,** 393-408.

Tan, Z., and A. Nehorai, 2014: Sparse direction of arrival estimation using co-prime arrays with off-grid targets. *IEEE Signal Processing Letters*, **21,** 26-29.

Tang, G., B. N. Bhaskar, and B. Recht, 2013a: Sparse recovery over continuous dictionaries: Just discretize. *Proceedings of Asilomar Conference on Signals, Systems, and Computers*.

Tang, G., B. N. Bhaskar, P. Shah, and B. Recht, 2013b: Compressed sensing off the grid. *IEEE Transactions on Information Theory*, **59,** 7465-7490.

Torres, S., and D. S. Zrnić, 2003: Whitening of signals in range to improve estimates of polarimetric variables. *Journal of Atmospheric and Oceanic Technology*, **20,** 1776-1789.

Tragl, K., 1990: Polarimetric radar backscattering from reciprocal random targets. *IEEE Transactions on Geoscience and Remote Sensing*, **28,** 856-864.

Trivett, D. H., and A. Z. Robinson, 1981: Modified Prony method approach to echo-reduction measurements. *The Journal of the Acoustical Society of America*, **70,** 1166-1175.

Tütüncü, R. H., K. C. Toh, and M. J. Todd, 2003: Solving semidefinite-quadratic-linear programs using SDPT3. *Mathematical Programming*, **95,** 189-217.

Uijlenhoet, R., and A. Berne, 2008: Stochastic simulation experiment to assess radar rainfall retrieval uncertainties associated with attenuation and its correction. *Hydrology and Earth System Sciences*, **12,** 587-601.

Van de Beek, C. Z., H. Leijnse, J. N. M. Stricker, R. Uijlenhoet, and H. W. J. Russchenberg, 2010: Performance of high-resolution X-band radar for rainfall measurement in The Netherlands. *Hydrology and Earth System Sciences*, **14,** 205-221.

Vaswani, N., and W. Lu, 2010: Modified-CS: Modifying compressive sensing for problems with partially known support. *IEEE Transactions on Signal Processing*, **58,** 4595-4607.

Venugopal, V., E. Foufoula-Georgiou, and V. Sapozhnikov, 1999: A space-time downscaling model for rainfall. *Journal of Geophysical Research: Atmospheres (1984–2012), 104(D16), 19705-19721, 1999.*, **104,** 19705-19721.

Villarini, G., and W. F. Krajewski, 2010: Review of the different sources of uncertainty in single polarization radar-based estimates of rainfall. *Surveys in Geophysics*, **31,** 107-129.

Volz, R., and S. Close, 2012: Inverse filtering of radar signals using compressed sensing with application to meteors. *Radio Science*, **47**.

Wakimoto, R. M., and V. N. V.N. Bringi, 1988: Dual-polarization observations of microbursts associated with intense convection: The 20 July storm during the MIST project. *Monthly Weather Review*, **116,** 1521-1539.

Wakin, M. B., 2010: Manifold-based signal recovery and parameter estimation from compressive measurements. *arXiv preprint arXiv:1002.1247*.

Wen, Z., W. Yin, and Y. Zhang, 2012: Solving a low-rank factorization model for matrix completion by a nonlinear successive over-relaxation algorithm. *Mathematical Programming Computation*, **4,** 333-361.

Wilson, J. W., and E. A. Brandes, 1979: Radar measurement of rainfall - A summary. *Bulletin of the American Meteorological Society*, **60,** 1048-1058.

Wirfält, P., G. Bouleux, M. Jansson, and P. Stoica, 2011: Subspace-based frequency estimation utilizing prior information. *IEEE Statistical Signal Processing Workshop*, 533-536.

Xu, W., J.-F. Cai, K. V. Mishra, M. Cho, and A. Kruger, 2014: Precise semidefinite programming formulation of atomic norm minimization for recovering d-dimensional ($d \geq 2$) off-the-grid frequencies. *IEEE Information Theory and Applications Workshop*.

Yanan, Y., L. Chunsheng, and Y. Ze, 2011: Parallel frequency radar via compressive sensing. *IEEE International Geoscience and Remote Sensing Symposium*, IEEE, 2696-2699.

Yang, Z., and L. Xie, 2014: Enhancing sparsity and resolution via reweighted atomic norm minimization. *arXiv preprint arXiv:1408.5750*.

Yoshikawa, E., and Coauthors, 2010: Development and initial observation of high-resolution volume-scanning radar for meteorological application. *IEEE Transactions on Geoscience and Remote Sensing*, **48,** 3225-3235.

Yu, L., H. Sun, J.-P. Barbot, and G. Zheng, 2012a: Bayesian compressive sensing for cluster structured sparse signals. *Signal Processing*, **92,** 259-269.

Yu, T.-Y., L. Ding, and S. Ozturk, 2011: Application of compressive sensing to refractivity retrieval with a network of radars. *IEEE Radar Conference*, Kansas City, IEEE, 757-761.

Yu, Y., A. Petropulu, and H. Poor, 2012b: CSSF MIMO radar: Compressive-sensing and step-frequency based MIMO radar. *IEEE Transactions on Aerospace and Electronic Systems*, **48,** 1490-1504.

Zachariah, D., P. Wirfält, M. Jansson, and S. Chatterjee, 2013: Line spectrum estimation with probabilistic priors. *Signal Processing*, **93,** 2969-2974.

Zawadzki, I., 1982: The quantitative interpretation of weather radar measurements. *Atmosphere-Ocean*, **20,** 158-180.

Zhu, X. X., and R. Bamler, 2012: Demonstration of super-resolution for tomographic SAR imaging in urban environment. *IEEE Transactions on Geoscience and Remote Sensing*, **50,** 3150-3157.

Zrnić, D., and P. Mahapatra, 1985: Two methods of ambiguity resolution in pulsed Doppler weather radars. *IEEE Transactions on Aerospace and Electronic Systems*, **AES-21,** 470-483.

Zygarlicki, J., and J. Mroczka, 2012: Prony\textquotesingles method used for testing harmonics and interharmonics in electrical power systems. *Metrology and Measurement Systems*, **19,** 659-672.